ASTRONOMY & ASTROPHYSICS
SUPPLEMENT SERIES

Astron. Astrophys. Suppl. Ser. **105,** 341-383 (1994)

Interstellar matter in Shapley-Ames elliptical galaxies. II. The distribution of dust and ionized gas*

P. Goudfrooij[1,**], L. Hansen[2], H.E. Jørgensen[2] and H.U. Nørgaard-Nielsen[3]

[1] Astronomical Institute "Anton Pannekoek", University of Amsterdam, Kruislaan 403, NL-1098 SJ Amsterdam, The Netherlands
[2] Copenhagen University Observatory, Øster Voldgade 3, DK-1350 København K, Denmark
[3] Danish Space Research Institute, Gl. Lundtoftevej 7, DK-2800 Lyngby, Denmark

Received November 22, accepted December 21, 1993

Abstract. — We present results of deep optical CCD imaging for a complete, optical magnitude-limited sample of 56 elliptical galaxies from the RSA catalog. For each galaxy we have obtained broad-band images (in B, V, and I) and narrow-band images using interference filters isolating the Hα+[NII] emission lines to derive the amount and morphology of dust and ionized gas. Detailed consideration of systematic errors due to effects of sky background subtraction and removal of stellar continuum light from the narrow-band images is described. The flux calibration of the narrow-band images is performed by deconvolving actually measured spectral energy distributions with the filter transmission curves. We also present optical long-slit spectroscopy to determine the [NII]/Hα intensity ratio of the ionized gas. Dust lanes and/or patches have been detected in 23 galaxies (41%) from this sample using both colour-index images and division by purely elliptical model images. We achieved a detection limit for dust absorption of $A_B \sim 0.02$. Accounting for selection effects, the true fraction of elliptical galaxies containing dust is estimated to be of order 80%. This detection rate is comparable to that of the IRAS satellite, and significantly larger than results of previous optical studies. Ionized gas has been detected in 32 galaxies (57%). The spectroscopic data confirm the presence and distribution of ionized gas as seen in the direct imaging. All elliptical galaxies in our sample in which a number of emission lines is detected show very similar emission-line intensity ratios, which are typical of LINER nuclei. The amounts of detectable dust and ionized gas are generally small—of order $10^4 - 10^5$ $M_\odot$ of dust and $10^3 - 10^4$ $M_\odot$ of ionized gas. The dust and ionized gas show a wide variety of distributions–extended along either the apparent major axis, or the minor axis, or a skewed axis, indicating that triaxiality is in general required as a galaxy figure. In some cases (NGC 1275, NGC 2325, NGC 3136, NGC 3962, NGC 4696, NGC 5018, NGC 5044, NGC 5813, IC 1459) the interstellar matter has a patchy or filamentary distribution, suggestive of a recent interaction event. The distributions of dust and ionized gas are consistent with being physically associated with each other.

Key words: galaxies: elliptical — elliptical galaxies: interstellar matter, photometry, structure

1. Overview

This is the second paper in a series presenting the results of a study of the optical and far-infrared properties of dust and ionized gas in a complete, blue magnitude-limited sample of luminous elliptical galaxies. Our main aim is to investigate the origin and fate of interstellar material and possible implications for scenarios of galaxy formation and evolution.

Recent advances in instrumental sensitivity have caused a renaissance of interest in the interstellar medium (ISM) of elliptical galaxies. Recent sensitive optical searches using CCDs have shown that even 'classical' elliptical galaxies often contain dust. The present consensus of these imaging surveys is that $\sim$ 35% of elliptical and S0 galaxies show optical evidence of dust lanes or patches (e.g., Sadler & Gerhard 1985; Sparks et al. 1985; Ebneter et al. 1988; Véron-Cetty & Véron 1988). Dust in elliptical galaxies has also been found by the Infrared Astronomical Satellite (IRAS). The detection frequency in co-added IRAS survey data has been found to be even larger than in the optical surveys (Jura et al. 1987; Knapp et al. 1989). Typical dust masses are of order $\sim 10^4 - 10^6$ $M_\odot$[1]. In

*Based on observations made at the European Southern Observatory, La Silla, Chile, and at the Royal Greenwich Observatory in the Spanish Observatorio del Roque de los Muchachos of the Instituto de Astrofisica de Canarias

**Present address*: ESO, Karl-Schwarzschild-straße 2, D-85748 Garching bei München, Germany

[1] We use $H_0 = 50$ km s^{-1} Mpc^{-1} in the course of this paper

addition to dust, spectroscopic surveys have revealed the presence of weak optical emission lines in the centres of E and S0 galaxies (Caldwell 1984; Phillips et al. 1986), typically indicating the presence of some $10^3 - 10^5$ $M_\odot$ of "warm" ionized gas within the central few hundred parsec. The quoted detection rate of optical emission-line gas was $\sim$ 55%. Moreover, observations with the EINSTEIN satellite have shown that a substantial number of luminous elliptical galaxies contains hot ($T \sim 10^7$ K), X-ray emitting gas (e.g., Forman et al. 1985; Kim et al. 1992). The presence of dust and gas in elliptical galaxies thus seems to be quite common.

Unlike the situation in spiral galaxies, physical and evolutionary relationships between the various components of the ISM are far from being understood. A number of theoretical concepts have been developed for the secular evolution of the different components of the ISM of luminous elliptical galaxies. The two currently most popular concepts are (1) the "cooling flow" picture in which stellar mass loss, heated to $10^6 - 10^7$ K by supernova explosions and collisions between expanding stellar envelopes during the violent galaxy formation stage, quiescently cools and condenses (see, e.g., the recent review of Fabian et al. 1991) and (2) the "evaporation flow" picture in which clouds of dust and gas have been accreted during post-collapse galaxy interactions. Subsequent heating (and evaporation) of the accreted gas is provided by thermal conduction in the hot, X-ray emitting plasma and/or star formation (cf. de Jong et al. 1990; Sparks et al. 1989; Bregman et al. 1990).

As to the origin of cool interstellar matter, a consensus is developing that dust in ellipticals is *always* accreted during a galaxy merger or interaction. Strong evidence for this is mainly provided in the case of early-type galaxies with large-scale dust and/or HI gas distributions: the gas (which is associated with the dust) is usually dynamically decoupled from the stellar velocity field, i.e., in disks rotating at random orientations with respect to the apparent major axis of the galaxy (e.g., Raimond et al. 1981; Möllenhoff 1982; Sharples et al. 1983; Bertola et al. 1985; Caldwell et al. 1986; Bertola & Bettoni 1988; Möllenhoff & Bender 1989; Kim 1989). The morphology of large-scale dust lanes also strongly suggests accretion events, as they often show warps or transitions from regular disks to irregular distributions in the outer regions. Another strong argument in favour of a galaxy interaction scenario is provided by the observation of substantial amounts of dust in luminous, X-ray emitting giant elliptical and cD galaxies (Jørgensen et al. 1983; Hansen et al. 1985; Sparks et al. 1989; Bregman et al. 1990; Goudfrooij 1991; Nørgaard-Nielsen et al. 1993). Since these galaxies are embedded in a hot ($T \sim 10^7$ K) gaseous halo, the presence of dust is surprising as the lifetime of a dust grain exposed to erosion by sputtering in such a hostile environment is $10^6 - 10^7$ yrs (e.g., Draine & Salpeter 1979). This dilemma can however be resolved in the "evaporation flow" scenario (cf. de Jong et al. 1990).

In spite of these arguments in favour of an external origin of the gas and dust, the majority of the ellipticals with dust exhibit *small*, arcsec scale dust lanes (cf. Ebneter et al. 1988, Véron-Cetty & Véron 1988). These lanes are often oriented parallel to the apparent major axis of the stellar body of the galaxy, in a well-defined disk-like configuration. Whether this small-scale dust also has an external origin is not clear a priori, since neither kinematical constraints nor X-ray observations are present in most cases. Furthermore, the late-type stellar population of typical giant ellipticals ($L_B = 10^{10} - 10^{11}$ $L_\odot$) has a substantial present-day mass loss rate ($\sim 0.1 - 1$ $M_\odot$ yr^{-1}; cf. Faber & Gallagher 1976). This material of internal origin could well be an important contribution to the total dust content of elliptical galaxies.

In order to systematically study the validity of the different theoretical concepts for the evolution of the ISM in elliptical galaxies, it is important to determine the morphological and physical relationships among the different components of the ISM and the structural parameters of the stellar component for a well-defined sample of elliptical galaxies. In particular, an important observational constraint for establishing the relative importance of the "cooling flow" and "evaporation flow" scenarios is whether or not dust lanes or patches are associated with warm ionized gas. Thus, imaging data of dust extinction and optical emission-lines are vital for such a study. Unfortunately, a major difficulty in studies of the ISM in ellipticals has been the lack of reliable data of a complete sample. The classification of early-type galaxies is quite difficult, and previous searches (except for the IRAS all-sky survey) have been made piecewise, with different selection criteria, levels of completeness, and sensitivity thresholds. For instance, recent imaging searches for ionized gas in elliptical and S0 galaxies have been performed only for galaxies with high IRAS flux densities (Kim 1989), or with detected X-ray emission (Trinchieri & di Serego Alighieri 1991; Shields 1991). This obviously makes it difficult to study the origin, global occurrence, and fate of the ISM in elliptical galaxies *in general*.

With this in mind, we have conducted a deep, systematic optical survey of a complete, blue magnitude-limited sample of ellipticals. Deep CCD imaging has been performed both through broad-band filters (Goudfrooij et al. 1993, hereafter referred to as Paper I) and through narrow-band filters isolating the nebular Hα+[NII] emission lines. In this paper we present the results of our CCD observations of 56 giant elliptical galaxies in the luminosity range $-19.5 > M_{B_T^0} > -23.3$. For each galaxy we have constructed colour index ($B-V$, $B-I$) images and images of the Hα+[NII] emitting gas. Medium-resolution ($\sim$ 1 Å/pixel) long-slit spectra are also presented to derive the correct [NII]/Hα emission-line ratio of the gas.

The survey also comprises long-slit spectroscopic data of lower resolution ($\sim$ 10 Å). The extensive spectroscopic data are used to study the kinematics and the excitation mechanism of the ionized gas, and the line-strength gradients of the stellar population. This will be presented in forthcoming papers.

Following a discussion of the galaxy sample (Sect. 2), we describe the observations and the reduction and analysis techniques employed in Sect. 3. In Sect. 4 we present the results of the observations in graphical and tabular form. The results are summarized in Sect. 5.

2. The galaxy sample

According to the classical definition (Hubble 1926; de Vaucouleurs 1959; Sandage 1961), elliptical (E) galaxies contain no dust, and no trace of a stellar disk. Consequently, galaxies with dusty features on photographic plates were usually given S0 or later classifications. Unfortunately, this practice is bound to blur the distinction between rotationally supported, flattened systems containing a stellar disk (i.e., S0 galaxies) and pure ellipsoidal systems (i.e., genuine ellipticals). Furthermore, the assignment of morphological types of early-type galaxies may easily be dependent on the quality and sensitivity of a given observation. To ensure consistency in the assignment of morphological types, we have chosen to draw our galaxy sample exclusively from the Revised Shapley-Ames Catalog of Bright Galaxies (Sandage & Tammann 1981), hereafter referred to as RSA.

We selected an optically complete, blue-magnitude limited sample of elliptical galaxies consisting of all galaxies with $B_T^0 < 12$ denoted E in the RSA. This magnitude limit was chosen in accordance with the sample of Jura et al. (1987) to ensure total coverage of coadded IRAS flux densities, and coincides with the completeness limit of the RSA. Table 1 lists the galaxies in our sample, along with the classification in both the RSA and the RC2 (de Vaucouleurs et al. 1976) catalogs. As Table 1 shows, the RSA and RC2 catalogs agree very well in the classification of the galaxies of our sample: 52 of the 56 galaxies (94%) in our sample are also classified as E in the RC2.

Table 1. The galaxy sample

Galaxy	Classification		v_{rad}	v_{grp}
	RSA	RC2	[km/s]	[km/s]
(1)	(2)	(3)	(4)	(5)
NGC 596	E0	E2	1902	1979
NGC 720	E5	E5	1697	1788
NGC 821	E6	E6	1727	1885
NGC 1275	Ep	p	5261	5433
NGC 1395	E2	E2	1702	1488
NGC 1399	E1	E1	1465	1319
NGC 1404	E1	E2	1994	1319
NGC 1407	E0	E0	1784	1563
NGC 1427	E3	E5	1681	1319
NGC 1537	E6	E/S0	1353	1136
NGC 1549	E2	E2	1173	979
NGC 1700	E3	E4	3953	4057
NGC 2300	E3	S0	1958	2279
NGC 2325	E4	E4	2248	2041
NGC 2974	E4	E4	1998	1727
NGC 2986	E2	E2	2397	1930
NGC 3136	E4	E4	1691	1413
NGC 3193	E2	E2	1392	1194
NGC 3250	E3	E3	2833	2692
NGC 3377	E6	E6	718	666
NGC 3379	E0	E1	885	666
NGC 3557	E3	E3	3111	2716
NGC 3608	E1	E2	1210	1022
NGC 3610	E5	E5	1765	1954
NGC 3613	E6	E6	2054	1954
NGC 3640	E2	E3	1354	1353
NGC 3706	E4	E/S0	3045	2474
NGC 3904	E2	E2	1613	1578
NGC 3962	E1	E1	1822	1390
NGC 4125	E6	E6	1375	1913
NGC 4261	E3	E2	2202	2049
NGC 4278	E1	E1	630	728
NGC 4365	E3	E3	1177	1037
NGC 4374	E1	E1	933	1037
NGC 4373	E4	E4	3417	3030
IC 3370	E2	E2	2933	3030
NGC 4473	E5	E5	2279	1037
NGC 4486	E0	E0p	1257	1037
NGC 4494	E1	E1	1310	1122
NGC 4564	E6	E6	1020	1037
NGC 4589	E2	E2	1971	1830
NGC 4621	E5	E5	414	1037
NGC 4660	E5	E5	1017	1037
NGC 4697	E6	E6	1308	1020
NGC 4696	E3	E1p	2925	2756
NGC 5018	E4	E3	2897	2517
NGC 5044	E0	E0	2704	2517
NGC 5061	E0	E0	1961	1625
IC 4296	E0	E0	3629	3459
NGC 5322	E4	E3	1804	2106
NGC 5576	E4	E3	1528	1518
NGC 5813	E1	E1	1882	1593
NGC 6482	E2	E3	3922	4090
NGC 7144	E0	E0	2113	1802
IC 1459	E4	E3	1628	1656
NGC 7507	E0	E0	1548	1603

Notes to Table 1:
Columns (2) and (3) list the galaxy classifications taken from the RSA (Sandage & Tammann 1981) and from the RC2 (de Vaucouleurs et al. 1976). Column (4) lists the radial velocities of the galaxies (cf. RSA), and Col. (5) lists the group velocity from Davies et al. 1987, corrected for the motion with respect to the centroid of the Local Group, calculated from solution No. 2 of Yahil et al. (1977)

3. Data acquisition and analysis

3.1. *Observations and data reduction*

Since the broad-band imaging observations have been described in detail in Paper I, we will only describe the optical narrow-band imaging and the spectroscopic observations in this section.

3.1.1. Narrow-band CCD imaging

The observations were done between 1984 and 1993 during several runs at the European Southern Observatory

Table 2. Narrow-band filter parameters

Name	Obs. site	Central wavelength	Width (FWHM)	Peak transm.
6569	LPO	6569 Å	60 Å	70 %
6607	LPO	6607	53	54
6652	LPO	6652	49	55
6970	LPO	6970	51	57
J66	ESO	6605	93	96
#389	ESO	6646	80	84
J69	ESO	6908	98	95

Notes to Table 2:
The first column lists the assigned names of the filters (cf. Table 5). The last column lists the peak transmissions of the filters

(ESO) and the La Palma Observatory (LPO). The southern sample objects were observed with the Danish 1.54-m telescope at ESO. The CCD images of the northern sample objects were taken with the 1.0-m Jacobus Kapteyn Telescope of LPO.

Observations of each galaxy were acquired through 2 narrow-band filters: one with a central wavelength appropriate for transmission of the Hα+[NII] emission lines at the redshift of the galaxy (hereafter called the "on-line" filter), and one at an adjacent redward band transmitting stellar continuum free of emission lines (the "off-line" filter). Care was taken not to include the [SII] (λ6716, λ6731) emission lines in the continuum passband, which was observed to provide a template for accurate subtraction of the contribution of stellar continuum to the emission-line image. Relevant parameters describing the filter passbands and peak sensitivities are listed in Table 2.

Various CCD detectors were used over the years. We list the relevant instrumental parameters of the different observing runs in Table 3. A log of the observations, including seeing measurements, is given in Table 5. Some additional (short) exposures have been made for objects that were originally observed during nonphotometric conditions.

The orientation of the CCD detector on the telescope was checked during the observing runs by making trailed exposures of bright stars. In most cases the detector was aligned correctly within 0°.5 except for the runs in January 1990 and April 1993 (both LPO) which were both misaligned by 2°.8. The images taken during these runs have been corrected for these misalignments.

The exposure times were generally chosen to equalize the signal to noise ratio achieved in the observations in the different passbands. We generally made multiple exposures to enable easy removal of cosmic ray hits. In the case of the Thomson CCD, care was taken not to saturate the CCD in view of its strong memory effect. This was done either by making a small pointing offset to move the bright stars off the field of view or by making multiple exposures with a reduced exposure time. Some of the detectors at ESO have been tested for linearity on the basis of dome flat fields under constant illumination. The nonlinearity of the CCD chips used here were found to be negligible (i.e., $< 1\%$) in the range of ADU levels used.

We have used the ESO IHAP and MIDAS image processing systems for the basic reduction of the CCD images. Several (of order 40) "bias" frames (with shutter closed and zero exposure time) were taken during each observing run to be able to eliminate possible structure in the bias level over the image. Only in the case of the ESO CCD #15 (RCA) it turned out to be necessary to construct separate bias frames, which were subtracted from the science images after having been matched in absolute level using the overscan region. In all other cases, the bias level was subtracted using the average level in the overscan region of the CCD.

Dark frames were also obtained during each run from several exposures of one hour duration with the shutter closed. The dark frames were median filtered before use in order to remove cosmic ray hits. These frames generally proved to be necessary in the reduction, especially in the case of the ESO CCD #15 (RCA) in which the central rows have a significantly higher dark current. Furthermore, this CCD has many 'hot' one-pixel size spots similar to cosmic rays but in fixed positions.

The images have been flatfielded using both dome flatfields illuminated by scattered sunlight and twilight sky exposures. The dome flatfields were used to correct for the high spatial frequency variations, e.g., bad columns of the CCDs. In this respect we note that the sensitivity of the ESO CCDs #8 and #15 (both RCA) showed column-to-column variations of a factor of ~ 2 at low count levels. Flatfielding could not completely correct this effect. We therefore constructed a "stripe frame" (with an average level equal to zero) from dome flats taken with a wide range of count levels. This stripe frame was subtracted from the flatfielded image after carefully matching the column offsets interactively across the image. The resulting image suffered cosmetically only from the most prominent defective columns of these CCDs. The other CCDs used in this study have very few blemishes. The twilight sky exposures were used to correct for the low-frequency spatial variations, since their colour temperature is better matched to that of the science images obtained at night. We emphasize that it is critical to reduce low-frequency spatial variations as much as possible in the case of surface photometry of (elliptical) galaxies (cf. Sect. 3.2). We therefore also made a few exposures of the empty sky through all narrow-band filters. The accuracy of the global flatfield correction was enhanced by fitting a two dimensional polynomial to the empty sky images and

the standard star images (avoiding objects in the field of view), usually of order 2. After this correction, the remaining low-frequency spatial variation was usually found to be less than 1%.

After the flatfielding process, the images were corrected for atmospheric extinction using the standard values for the ESO and LPO observatories (Tüg 1977, Argyle et al. 1989), and normalized to an exposure time of 60 s.

Cosmic ray hits were identified by pixel values exceeding a local 5σ threshold and replaced by a median value which was calculated over the nearest 7×7 pixels box.

The sky background level was determined by a power-law fit to the outer parts of the radial intensity profile of an elliptical fit to the galaxy isophotes. This method has been shown to be a very reliable method for sky subtraction in the case of surface photometry of large elliptical galaxies with a relatively small detector (see Paper I). We have compared the results of this power-law approach with sky values that were determined by calculating the mean pixel values of 20×20 pixels boxes in the corners of the field of view. The difference in derived sky values generally turned out to be a few percent. Although this is not much larger than that expected from errors in the flatfielding process, it proved to be significant during the final emission-line image generation (see Sect. 3.2 below).

3.1.2. Long-slit spectroscopy

The long-slit spectrograms were obtained during several observing runs at the 1.52-m and 2.2-m ESO/MPI telescopes at ESO, and the 2.5-m Isaac Newton Telescope and 4.2-m William Herschel Telescope at LPO. Table 4 lists the relevant instrumental parameters of the different observing runs. A log of the observations is given in Table 5.

At ESO, flat field images were obtained through exposures of a flat slide screen which was mounted on the inside of the telescope dome, and illuminated by a photo lamp. At the LPO telescopes, the flat field correction images were obtained using exposures of an internal lamp, supplemented by exposures of the twilight sky to check the illumination of the slit by the internal lamps.

The data reduction procedure has been carried out using the MIDAS image processing system. After the usual steps of CCD reduction (bias subtraction, division by a normalized flatfield, filtering of cosmic rays), the frames were calibrated in wavelength using Helium-Argon comparison lamp spectra which were taken before and after each scientific exposure. At LPO we used a Neon comparison lamp. The spectra were transformed to a linear wavelength scale by fitting, row by row, a third order polynomial to the positions of the emission lines in the spectra of the comparison lamps. Fine tuning of the wavelength calibration was done by measuring the centres of night sky emission lines in the calibrated science frames; the zero point shift was always (and usually much) less than 1 Å, i.e., smaller than the resolution. The final resolution of the spectra taken during the different observing runs (determined from the comparison lamp spectra) are listed in Table 4.

Sky subtraction was performed in the following way. A preliminary sky frame (of the same dimensions as the science frame) was constructed from the ends of the slit, where the residual light from the galaxy can be neglected. A larger part of the galaxy frame was used for a second sky frame in which the misalignment of the sky emission lines with the rows of the CCD detector was fitted by a third order polynomial. The second sky frame was normalized to the absolute level of the first sky frame and subsequently subtracted from the galaxy frame. After this procedure, the residuals at the sky lines were found to be fully consistent with Poisson noise.

The spectra were flux-calibrated using wide-slit observations of spectrophotometric standards from the lists of Oke (1974), Stone (1977), Oke & Gunn (1983), Stone & Baldwin (1983), and Massey et al. (1988). After correction for atmospheric extinction, the spectra were corrected for Galactic foreground extinction using A_B values from Burstein & Heiles (1984) when available, and the cosecant approximation (cf. RC2) for the remaining galaxies. Finally, we corrected the spectra for *internal* absorption in the cases of galaxies with dust lanes or patches using our E_{B-V} values as determined below in Sect. 4. The A_B and E_{B-V} values were converted to the appropriate wavelengths using the Savage & Mathis (1979) extinction law.

3.2. *Emission-line image generation*

Various sources of error hamper a proper generation of images containing pure emission-line intensity. Firstly, the different on- and off-line images have to be aligned to a common registration and position angle. This transformation procedure is very critical and has to be correct to within a few hundredths of a pixel; this accuracy was reached by measuring the centroids of stars in the common field of view by a Gaussian fit. In a few cases we derived the shift offsets from the centroids of the galaxy nuclei since suitable stars were absent. Fine tuning of the alignment was done by inspection of spurious residuals in on-line/off-line quotient images (see below). The aligned images were summed to produce final on- and off-line images which were subsequently matched to a common seeing profile by Gaussian smoothing along rows and columns. The second, and most important, source of error is the scale factor that has to be applied to the off-line image in order to serve as template for subtraction of the stellar light from the on-line images. Since emission lines in normal elliptical galaxies are generally of low equivalent width (of order 1 Å, cf. Phillips et al. 1986), this scale factor has to be determined very accurately (e.g., an error of 1% in the scale factor for images taken with 100 Å wide filters results in an error of 1 Å in equivalent width). A possible additional problem in

Table 3. Narrow-band imaging: telescopes and instrumentation

Run	Sep 84	Aug 87	Oct 87	Nov 87	Apr 88	Jan 90
Observer[1]	HEJ	HUNN	LH	LH	HEJ	PG
Observatory	ESO	ESO	ESO	ESO	ESO	LPO
Telescope[2]	1.54	1.54	1.54	1.54	1.54	JKT
CCD	RCA #1	RCA #8	RCA #8	RCA #8	RCA #8	RCA #2
Type	SID 53612	SID 006 EX	SID 006 EX	SID 006 EX	SID 006 EX	SID 501
# Pixels	320 × 512	640 × 1024	640 × 1024	640 × 1024	640 × 1024	320 × 512
Pixel size (μm)	30	15	15	15	15	30
Binning	1 × 1	2 × 2	2 × 2	2 × 2	2 × 2	1 × 1
Scale ($''$ bin^{-1})	0.471	0.475	0.475	0.475	0.475	0.41
Field of view	2.′5 × 4.′0	2.′5 × 4.′0	2.′5 × 4.′0	2.′5 × 4.′0	2.′5 × 4.′0	2.′2 × 3.′5
Readout noise	70 e$^-$	27 e$^-$	27 e$^-$	27 e$^-$	27 e$^-$	55 e$^-$

Run	Mar 90a	Mar 90b	May 90	Feb 91	Apr 92a	Apr 93
Observer[1]	HUNN	PG	PG	PG	PG	PG
Observatory	ESO	LPO	ESO	LPO	ESO	LPO
Telescope[2]	1.54	JKT	1.54	JKT	1.54	JKT
CCD	RCA #15	GEC #3	RCA #15	GEC #3	THX #17	EEV #7
Type	SID 006 EX	P8603-A	SID 006 EX	P8603-A	31156 A	P88300
# Pixels	640 × 1024	385 × 578	640 × 1024	385 × 578	1024 × 1024	1242 × 1152
Pixel size (μm)	15	22	15	22	19	22.5
Binning	2 × 2	1 × 1	2 × 2	1 × 1	1 × 1	1 × 1
Scale ($''$ bin^{-1})	0.475	0.30	0.475	0.30	0.298	0.306
Field of view	2.′5 × 4.′0	1.′9 × 2.′9	2.′5 × 4.′0	1.′9 × 2.′9	5.′1 × 5.′1	6.′3 × 5.′9
Readout noise	35 e$^-$	10 e$^-$	35 e$^-$	10 e$^-$	5 e$^-$	5 e$^-$

[1] Observers: HEJ ≙ H.E. Jørgensen, HUNN ≙ H.U. Nørgaard-Nielsen, LH ≙ L. Hansen, PG ≙ P. Goudfrooij.
[2] Telescopes: 1.54 ≙ 1.54-m Danish Telescope, JKT ≙ 1.0-m Jacobus Kapteyn Telescope

this respect is that the scale factor is in principle a function of radial distance from the galaxy centre since the stellar Hα absorption feature (which is measured through the on-line filter) represents a possible source of radial gradients. However, past spectroscopic studies have shown that the Hβ absorption line generally exhibits only very shallow radial gradients in equivalent width (cf. Gorgas et al. 1990; Davies et al. 1993; Carollo et al. 1993). We therefore assume the scale factor to be unaffected by radially variable Hα absorption. The third source of error is misestimation of sky levels in the on-line and/or off-line images. The errors in the sky determination (cf. Sect. 3.1.1) of the two images are however expected to (partially) cancel when the off-line image is subtracted from the on-line image since both sky values have been derived using the same method. Another anticipated source of error when utilising thinned (RCA) CCDs is residual high-frequency spatial variations due to improper flatfielding for objects with extended emission-line regions. In principle, these so-called "fringes" can be flatfielded out correctly when a filter is chosen with a bandwidth comparable to that of the emission line. In practice however, the emission lines cover only part of the filter bandwidth, leading to interference by the emission lines of the object in the CCD detector. Fringe patterns in narrow-band flat fields taken with RCA CCDs lead to typical high-frequency spatial variations of up to 10%. Hence, different fringe patterns in the galaxy images taken during the night can lead to an extra uncertainty in the total line flux of the order of a few percent. However, careful inspection of our final emission-line images shows that the residual effect of fringing is generally negligible, i.e., consistent with Poisson noise, over the whole field of view.

We have determined the optimum scale factor of the off-line images in the following way. In the absence of radial gradients in the spectral energy distribution of the stellar continuum, the ratio $R(r)$ of surface brightness measured for the on- and off-line images can be written as

$$R(r) = \frac{a\Sigma_{\rm cont}(r) + \Sigma_{\rm emission} + \delta_{\rm emission}}{\Sigma_{\rm cont}(r) + \delta_{\rm cont}} \qquad (1)$$

where $\Sigma_{\rm cont}(r)$ is the continuum surface brightness profile of the galaxy, a is a scale factor (assumed to be constant), $\Sigma_{\rm emission}$ is the emission-line surface brightness profile,

Table 4. Long-slit spectroscopy: telescopes and instrumentation

Run	Oct 90	Apr 91	Dec 91	Apr 92a	Apr 92b	May 92
Observing dates	Oct 5–9	Apr 23–30	Dec 26–30	Apr 1–5	Apr 7–10	May 23–26
Observer(s) [1]	PG	PG	PG/DC	PG	DC	PG/DC/LBH
Telescope [2]	2.2	INT	WHT	1.52	WHT	WHT
Spectrograph [3]	B&C	IDS	ISIS	B&C	ISIS	ISIS
Grating	#26	R632V	R600R	#26	R600R	R600R
CCD	RCA #8	GEC #6	EEV #3	FA #27	EEV #3	EEV #3
Type	SID 006 EX	P8603-A	P88300	2048 L	P88300	P88300
# Pixels	640 × 1024	385 × 578	1242 × 1152	2048 × 2048	1242 × 1152	1242 × 1152
Readout noise	27 e^-	10 e^-	5 e^-	7 e^-	5 e^-	5 e^-
Slit length	4′.9	4′.0	4′.0	2′.9	4′.0	4′.0
Slit width	2″.0	1″.6	1″.2	2″.0	1″.2	1″.2
Spatial scale (pixel^{-1})	0″.89	0″.65	0″.34	0″.68	0″.34	0″.34
Resolution (FWHM)	1.8 Å	2.8 Å	1.9 Å	2.7 Å	1.9 Å	1.9 Å

[1] Observers: DC ≙ D. Carter, LBH ≙ L.B. van den Hoek, PG ≙ P. Goudfrooij.
[2] Telescopes: 1.52 ≙ 1.52-m ESO telescope, 2.2 ≙ 2.2-m ESO/MPI telescope, INT ≙ 2.5-m Isaac Newton Telescope at LPO, WHT ≙ 4.2-m William Herschel Telescope at LPO.
[3] Spectrographs: B&C ≙ Boller & Chivens, IDS ≙ Intermediate Dispersion Spectrograph, ISIS: Double spectrograph of intermediate dispersion

and $\delta_{\rm emission}$ and $\delta_{\rm cont}$ are residuals of the sky background in the emission-line and continuum bandpasses, respectively. Since surface brightness scales monotonically with radius in elliptical galaxies, errors in sky subtraction will lead to gradients in $R(r)$ that are monotonic with radius in regions of the galaxy which are *devoid of any line emission*. In case of erroneous sky subtraction, one can thus still reach the ideal case of a ratio $R(r)$ that is constant as a function of radius using an iterative method wherein the sky levels are adjusted (i.e., to reach $\delta_{\rm emission} = a \times \delta_{\rm cont}$, see also Shields 1991). It is however of crucial importance to select the regions devoid of line emission from the images. To this end we first constructed a "ratio image" which is the quotient of the on-line and off-line images. In case the on- and off-line images have been aligned correctly, these images evidently show a very smooth behaviour with radius except in regions where line emission is detected. The ratio images were therefore studied visually using a colour display to check the alignment of the images, and to determine the (preliminary) distribution of line emission in the galaxies. The radius outside which no emission was evident was registered and checked against our long-slit spectra; the latter indeed confirmed the absence of emission (to within the noise) outside the registered radius.

Elliptical isophotes were subsequently fitted to the on- and off-line surface brightness distributions using the program package *GALPHOT* created by M. Franx (cf. Jørgensen et al. 1992; Paper I). After removal of the stars and bad regions in the images, the data were fitted from the radius outside which no line emission was evident out to the radius where the uncertainties in the ellipse parameters exceeded 3%. After a succesful fitting procedure, purely elliptical model images were created from the fits and radial surface brightness profiles were derived for both the on- and off-line images by averaging over the elliptical isophotes. A least-squares fit was made to the radial on-line/off-line profile; if the slope was non-zero, the off-line profile was iteratively modified by an additive constant value until the ratio profile was consistent with zero. This method thus provides the "optimal" scale factor of the off-line image along with a quantified uncertainty of this value. Usually the initial sky values as determined by the power-law fits (Sect. 3.1.1) proved to be very accurate: they only needed modifications of $\leq$1%, which is smaller than, e.g., the dispersion of sky values in the corner boxes. In a few instances the ratio images revealed prominent, extended line-emitting regions (e.g., NGC 5044, IC 1459); in these cases the scale factor could not be accurately determined by the method described above since the interval in radius to be fitted by the ellipse fitting routine was too small to yield unambiguous results. In these cases the scaling factor was determined by calculating the mean pixel values of regions which appeared devoid of line emission in the on-line/off-line ratio image. The final scale factor was then assigned to be the overall mean value (with its associated dispersion). Errors in the sky values were checked by visually examining a series of ratio images, with a sequence of sky values of the off-line image centred on the initial value. The "best" ratio image was then selected.

Table 5. Observing log

	Narrow-band imaging						*Long-slit spectroscopy*			
Galaxy	Run	Line filter	t_{exp} [sec]	Cont. filter	t_{exp} [sec]	Seeing FWHM	Run	Slit PA	t_{exp} [sec]	Seeing FWHM
(1)	(2)	(3)	(4)	(5)	(6)	(7)	(8)	(9)	(10)	(11)
NGC 596	Oct 87	J66	3600	J69	3600	1.1	Dec 91	00	2700	1.0
NGC 720	Oct 87	J66	1320	J69	1320	1.5	Dec 91	142	3600	1.7
NGC 821	Oct 87	J66	1500	J69	1500	1.7	Dec 91	220	3600	1.7
NGC 1395	Sep 84	J66	3000	J69	3000	1.8	Oct 90	05	3600	
								95	7200	2.2
NGC 1399	Sep 84	J66	3000	J69	3000	1.8				
NGC 1404	Oct 87	J66	1200	J69	1200	1.9	Oct 90	163	7200	2.5
NGC 1407	Oct 87	J66	3600	J69	3600	1.7	Oct 90	54	6000	2.5
NGC 1427	Oct 87	J66	1380	J69	1380	1.4				
NGC 1537	Oct 87	J66	900	J69	900	1.7				
NGC 1549	Oct 87	J66	1260	J69	1260	1.7				
NGC 1700	Oct 87	J66	2400	J69	1800	1.6				
NGC 2300	Jan 90	6607	6000	6970	6000	1.8	Dec 91	235	3600	0.8
NGC 2325	Nov 87	J66	3600	J69	3600	1.9	Dec 91	04	1800	0.8
								13	1800	0.8
								36	4500	1.7
								348	3600	0.8
NGC 2974	Mar 90a	J66	3600	J69	3600	1.9	Dec 91	312	3600	0.8
NGC 2986	Mar 90a	J66	3600	J69	3600	1.4				
NGC 3136	Mar 90a	J66	3600	J69	3600	1.7	Apr 92a	35	8100	2.3
								125	7200	2.0
NGC 3193	Mar 90b	6607	6000	6970	6000	3.5				
NGC 3250	Mar 90a	J66	3600	J69	3600	1.6				
NGC 3377	Apr 92	J66	2700	J69	2700	1.3	Apr 92b	40	3600	1.2
NGC 3379	Mar 90b	6607	3600	6970	3600	1.6				
NGC 3557	Mar 90a	J66	3600	J69	3600	1.4	Apr 92a	80	7200	2.3
								170	3600	2.0
NGC 3608	Mar 90b	6607	7200	6970	7200	1.6	Apr 92b	29	3000	1.2
							May 92	79	3600	1.0
NGC 3610	Apr 93	6607	3600	6970	3600	1.2	May 92	133	3600	0.9
NGC 3613	Apr 93	6607	5400	6970	5400	1.7				
NGC 3640	May 90	J66	2400	J69	2400	1.3				

Table 5. continued

	Narrow-band imaging						*Long-slit spectroscopy*			
Galaxy	Run	Line filter	t_{exp} [sec]	Cont. filter	t_{exp} [sec]	Seeing FWHM	Run	Slit PA	t_{exp} [sec]	Seeing FWHM
(1)	(2)	(3)	(4)	(5)	(6)	(7)	(8)	(9)	(10)	(11)
NGC 3706	Mar 90a	J66	3600	J69	3600	1.4				
NGC 3904	Mar 90	J66	3600	J69	3600	1.4	Apr 92a	17	3600	2.1
NGC 3962	Mar 90a	J66	5400	J69	3600	1.3	Apr 92a	48	7200	2.1
NGC 4125	Apr 93	6607	5400	6970	5400	1.1	Apr 91	88	3900	1.5
							Dec 91	268	3600	1.7
							May 92	45	1800	
NGC 4261	Apr 88	J66	3600	J69	3000	1.4	Dec 91	00	3600	1.0
NGC 4278	Mar 90b	6569	5400	6970	5400	1.6	Apr 91	62	4500	1.5
							May 92	200	3600	1.0
NGC 4365	May 90	J66	2160	J69	2160	1.5				
NGC 4374	Feb 83	J66	3600	J69	3600	1.4	Apr 92a	85	6300	2.3
								175	6000	2.0
NGC 4373	Mar 90a	J66	3600	J69	3600	1.3				
IC 3370	Mar 90a	J66	3600	J69	3600	1.7	Apr 92a	43	7200	2.1
								133	7200	2.3
NGC 4473	Feb 91	6607	6000	6970	5400	1.2				
NGC 4486	Not observed									
NGC 4494	Not observed									
NGC 4564	Apr 92	J66	3600	J69	2700	1.1				
NGC 4589	Feb 91	6607	3600	6970	3600	2.3	Apr 91	175	6300	1.5
							Apr 92b	95	3600	1.2
NGC 4621	Mar 90b	6569	3600	6970	3600	1.5				
NGC 4660	May 90	J66	1260	J69	1260	1.4	May 92	95	3600	0.9
NGC 4697	Mar 90a	J66	3600	J69	3600	1.2	May 92	62	3600	0.9
NGC 4696	May 82	J66	3600	J69	3600	1.1	Apr 92a	96	7200	2.0
NGC 5018	Mar 90a	J66	3600	J69	3600	1.7	Apr 92a	95	7200	2.1
							May 92	39	3600	1.1
NGC 5044	May 90	J66	5400	J69	5400	1.7	May 91*	23	7200	1.5
								96	7200	1.5
							Apr 92a	151	9000	2.1
							May 92	59	3600	0.9
NGC 5061	Mar 90a	J66	3600	J69	3600	1.4				
IC 4296	Apr 92	#389	3600	J69	3600	1.8	Apr 92a	59	5400	2.0

Table 5. continued

	Narrow-band imaging						*Long-slit spectroscopy*			
Galaxy	Run	Line filter	t_{exp} [sec]	Cont. filter	t_{exp} [sec]	Seeing FWHM	Run	Slit PA	t_{exp} [sec]	Seeing FWHM
(1)	(2)	(3)	(4)	(5)	(6)	(7)	(8)	(9)	(10)	(11)
NGC 5322	Feb 91	6607	3600	6970	3600	2.0	Apr 91	93	4500	1.5
							Dec 91	48	3600	1.7
							Apr 92b	03	8100	0.8
NGC 5576	May 90	J66	1800	J69	1200	1.5				
NGC 5813	Mar 90a	J66	2700	J69	2700	1.8	Apr 92a	47	7200	2.1
								137	5400	2.1
							May 92	27	3600	1.0
								182	3600	0.7
NGC 6482	Feb 91	6652	7200	6970	4500	1.6	May 92	08	3600	1.0
								250	3600	0.9
NGC 7144	Sep 87	J66	3600	J69	3600	1.8	Oct 90	20	7200	2.2
IC 1459	Sep 87	J66	3600	J69	3600	1.5	Oct 90	38	10800	2.2
								83	7200	2.5
								128	7200	2.5
NGC 7507	Sep 87	J66	3600	J69	3600	1.7				

Notes to Table 5:
In Col. (1): Galaxy name. Column (2): Run name (cf. Table 3). The narrow-band images of NGC 4374 (run "Feb 83") and NGC 4696 (run "May 82") have already been described in Hansen et al. (1985) and Nørgaard-Nielsen & Jørgensen (1984), respectively. Columns (3) and (4): Filter used for the on-line image and the total exposure time in seconds, respectively. Columns (5) and (6): Filter used for the off-line image and the total exposure time in seconds, respectively. Column (7): Seeing values (FWHM in arcsec) of the narrow-band imaging. Column (8): Run name (cf. Table 4). Column (9): Position angle of slit. Column (10): Total exposure time in seconds. Column (11): Approximate seeing (FWHM in arcsec) during observation
* The run May 91 was performed by P. Goudfrooij and T. Oosterloo on the ESO/MPI 2.2-m telescope equipped with the ESO Faint Object Spectrograph & Camera #2 and grism #9 (wavelength range 5875 – 7820 Å, resolution $\sim$ 3.3 Å, spatial scale = $0''.332$ pixel^{-1})

After the optimal continuum scale factor was derived, the off-line image was scaled and subtracted from the on-line image, yielding the final emission-line image. The uncertainty in the measured emission-line intensity includes photon noise in both the on- and off-line images as well as systematic errors related to the continuum scale factor, sky subtraction, and the residual low- and high-frequency spatial variations after flatfielding. Estimating the latter at 1%, the (2σ) detection limit for Hα+[NII] emission is estimated at

$$\delta(\mathrm{EW\ [\AA]}) = 0.015\ \mathrm{FWHM_{filter}[\AA]}$$

where EW stands for equivalent width.

Note that the approach described above produces results which are not sensitive to the presence of line-emitting material distributed like the continuum starlight. However, comparison of our final emission-line images with our long-slit spectra shows that such emission is rarely, if ever, present. In other words, the spectra show the emission-line images to be faithful to within the noise along the sampled position angles.

3.3. *Colour-index images*

To find dust lanes and/or patches, the broad-band images presented in Paper I have been used to construct colour index ($B-V$ and $B-I$) images. The alignment and the sky subtraction of the images in the different passbands was performed similar to the narrow-band images as described in the previous section. We also created "residual" images, defined as the difference between the original and a (purely elliptical) model image; the model image was created by the *GALPHOT* ellipse fitting package (see Pa-

per I). Image pixels occupied by foreground stars, cosmic rays, and neighbouring galaxies were flagged before the model fit was executed. Dust lanes or patches were also excluded from the fit if present, as well as the prominent optical jet in the case of NGC 4486. The model images were also used to create "extinction" images, e.g., $A_V = -2.5 \log(V_{\rm obs}/V_{\rm model})$.

3.4. *Emission-line spectrum generation*

As a first step in the generation of nuclear pure emission-line spectra, we extracted the central $\sim 3''$ from all galaxy spectra (corresponding on average to 0.5 Kpc). This was done to enable a comparison of our results with previous investigations using similar apertures (e.g., Véron-Cetty & Véron 1986; Phillips et al. 1986).

As mentioned before, emission lines in normal elliptical galaxies are generally very weak and therefore severely entangled with the underlying stellar absorption-line spectrum. It is thus crucial to have a suitable stellar population template in order to isolate the pure emission-line component from the spectra. The nuclear absorption-line spectra of luminous elliptical galaxies are very similar (see, e.g., Bica 1988). With this in mind, we have built an absorption-line template by averaging nuclear spectra of the observed galaxies in our sample which did not show any evidence for emission lines (neither in their emission-line images nor in their spectra), after having converted the nuclear spectra of all observed galaxies to zero redshift. The galaxies used for the template were NGC 596, 720, 821, 1404, 1427, 1549, 2300, 3904, and 7144. A number of these galaxies were observed during other observing runs which will be described elsewhere (Goudfrooij 1993, in preparation), and included in the template in order to provide a better signal-to-noise ratio of the template spectrum.

The importance of the template subtraction is demonstrated in Appendix B where original spectra of line-emitting galaxies, their scaled template, and the pure emission-line spectra. The emission lines Hα, [NII] $\lambda\lambda$6548, 6583, and [SII] $\lambda\lambda$6716, 6731 are shown. Notice that especially in galaxies with weak emission (e.g., NGC 4697; NGC 5322), the effect of template subtraction on the Hα line is fundamental, and has to be taken into account in the flux calibration of the emission-line images (cf. below). The residual emission-line spectra also serve as a check to the applied extinction corrections by means of the slope of the continuum baseline; in virtually all cases no further reddening correction was needed.

3.5. *Flux calibration of emission-line images*

The measured Hα+[NII] fluxes have been converted to an absolute flux scale using out-of-focus exposures of spectrophotometric standards from the lists of Oke (1974), Stone (1977), Oke & Gunn (1983), Stone & Baldwin (1983), and Massey et al. (1988). The images of NGC 3608, NGC 4589 and NGC 5322 which were taken during non-photometric weather have been flux calibrated by measuring the intensity of a subimage at the same position on the sky as the extracted region of the galaxy that was covered by the spectrograph slit during a spectroscopic observation. Comparison with the measured Hα+[NII] emission-line flux in the spectrum thus yielded the total flux.

In principle, the spectra of standard stars can be approximated as a constant function of wavelength for narrow-band filters. However, the Hα absorption line generally is a strong feature in standard star spectra, thereby imposing potential problems for the flux calibration of some frequently used filters (i.e., the 6569, 6607 and J66 filters, cf. Table 2). To overcome this problem, we used standard star spectra which were taken during our spectroscopic observing runs (cf. Table 4) to calculate the average flux-density-weighted transmission for these filters. The average differences of these transmission values with mean transmission values calculated with flat weighting were found to be 6.2%, 2.5%, and 1.5% for the 6569, 6607 and J66 filters, respectively.

Another problem which is often discarded in the calibration of narrow-band imaging studies is that (instrumental-to-absolute) flux conversion factors which are derived using standard star continua are in principle *not* appropriate for calibrating emission-line fluxes in view of their different spectral energy distribution within the filter passband (see also Shields 1991). In the present case of combined Hα (λ6563) and [NII] (λ6548, λ6583) emission, the flux conversion factor for the (gaseous) emission can be written as

$$F_{\rm flux,emission} = \frac{F_{\rm flux,star}}{W_{6548}\,T_{6548} + W_{6563}\,T_{6563} + W_{6583}\,T_{6583}} \quad (2)$$

where $F_{\rm flux,star}$ is the flux conversion factor derived from the standard star observation, W_λ is a weight factor corresponding to the fractional contribution of the emission line at wavelength λ to the total emission, and T_λ is the filter transmission at wavelength λ. Hence, a proper emission-line flux calibration can *only* be achieved when the W_λ values (i.e., the [NII]/Hα ratios) are known. Since [NII]/Hα ratios in normal elliptical galaxies span a quite large range (cf. Table 6; Phillips et al. 1986), the usually made assumption of an average [NII]/Hα ratio can impose significant errors in the calibration, especially for objects of which strong emission lines are present near the wavelength boundaries of the filter used. The weight factors W_λ were derived by fitting Gaussians to the emission lines in our *pure* emission-line spectra (i.e., after template subtraction, cf. Sect. 3.4). In case no Hα+[NII] emission was detected, we assumed [NII]λ6583/Hα = 1.38, which is the average intensity ratio found by Phillips et al. (1986) using their spectroscopic dataset of 203 southern E and S0 galaxies. The emission-line fluxes were additionally cor-

rected for Galactic foreground extinction and intrinsic extinction by dust as mentioned in Sect. 3.1.2.

4. Results

The final colour-index ($B-I$ if available, otherwise $B-V$) and Hα+[NII] images of galaxies which show evidence of dust and/or ionized gas are shown in Figs. 1–34, along with a isophotal contour map of the broad-band B image to enable a morphological comparison. North is up and East is to the left for all images shown. The colour-index and Hα+[NII] images have been slightly smoothed by a circular Gaussian to reduce the noise at faint levels. The morphologies of individual objects are discussed below in Sect. 4.3.

The final Hα+[NII] fluxes were measured by integrating over an aperture large enough to contain all the line emission, and therefore different for each galaxy. Results are listed in Table 6. In view of possible residual effects of incorrect PSF matching of the on– and off-line images, fluxes are only listed for apertures larger than twice the seeing FWHM, unless the presence of emission lines is confirmed by the long-slit spectra. The tabulated uncertainties represent 1σ errors determined as described in Sect. 3.2. The upper limits are listed as 2σ thresholds integrated over a metric aperture of radius 1 Kpc. The line fluxes were converted to luminosities using the group velocities taken from Davies et al. (1987) and reproduced in Table 6.

4.1. *Comparison with previous flux measurements*

Flux measurements from imaging studies are available in the literature for several galaxies in the present sample, and a comparison of the results is listed in Table 7.

In general, our Hα+[NII] fluxes are found to be consistent with the results from previous imaging studies. However, for a number of objects notable disagreement is present. Our flux for NGC 1395 is found to be one order of magnitude lower than that measured by Trinchieri & di Serego Alighieri (1991). Part of this discrepancy may be due to systematic errors as discussed in Sect. 3.5. However, a measurement of the flux covered by the slit region of our spectroscopic observation from our emission-line image is found to be consistent with the flux measured from the spectrum, so we find it hard to believe that our calibration is in error. Also our result for NGC 4697 is not consistent with that of Trinchieri & di Serego Alighieri, but in this case our flux is *higher* by a factor of about 5. A significant fraction of the emission-line flux from NGC 4697 is due to faint extended emission (cf. Fig. 24), which they did not detect, so this discrepancy may be due to a higher sensitivity of our observation of NGC 4697. Our fluxes are reasonably consistent with those given by Kim (1989), although in some cases they are different by a factor of about 2. However, a proper comparison is hampered by the fact that Kim did not specify his aperture sizes. The measurements of Shields (1991) are mostly consistent with ours except for the case of IC 4296 for which his flux is higher by a factor of about 5. Neither the extent of emission nor the flux from the central 2″ region reported by Shields' image is confirmed by our spectrum, so we are led to believe our own flux measurement.

4.2. *Derived masses of dust and ionized gas*

Dust. The dust mass can be estimated by integrating the reddening over the areas of the colour index images which are depleted in blue light. We only considered reddened areas with a morphology bearing no similarity to the elliptical galaxy isophotes, i.e., dust lanes or patches. Assuming the dust in the elliptical galaxies to be similar to that in our own galaxy (i.e., a gas-to-dust ratio of 100 by mass), the corresponding E_{B-V} values are converted to an equivalent mass of neutral hydrogen using the Galactic ratio of neutral hydrogen column density to colour excess $N_H/E_{B-V} = 5.8\ 10^{21}$ cm^{-2} mag^{-1} (Bohlin et al. 1978). E_{B-I}-values have been converted to E_{B-V} using the Savage & Mathis (1979) reddening law. It should be pointed out that this method presupposes that the dust and gas constitute a homogeneous layer in front of the stars in the galaxy. In reality the dust may be highly clumpy and deeply embedded in the central areas of the galaxy. Furthermore, orientation effects can be significant since we measure E_{B-V} relative to a mean colour which is assumed to be free of dust. Thus we are not sensitive to e.g., absorption by a face-on dust lane. In any case we underestimate the amount of dust, and the resulting dust mass is consequently a lower limit. We have achieved a mean detection limit of $E_{B-I} \sim 0.01$, corresponding to $A_B = 0.018$; assuming a minimum size for a dust patch of 10 $(″)^2$, the lower limit to the mass of detectable dust is $2.2\ 10^4\ (D/25$ Mpc$)^2\ M_\odot$, where D is the distance of the galaxy.

Ionized gas. The mass of ionized gas can be estimated by assuming homogeneous physical conditions in the clouds. A glance at the spectra in Appendix B reveals that the [SII] λ6716 and λ6731 lines are always nearly equal in intensity when detected. For an assumed electron temperature of 10^4 K, this implies an electron density of $\sim 10^3$ cm^{-3} (e.g., Osterbrock 1974). Using standard case B recombination theory (Osterbrock 1974), the mass of ionized gas can be written as

$$M(\mathrm{HII}) = 2.33\ 10^3 \left(\frac{L(\mathrm{H}\alpha)}{10^{39}\ \mathrm{erg\ s^{-1}}}\right) \left(\frac{10^3\ \mathrm{cm^{-3}}}{n_e}\right) M_\odot \quad (3)$$

where n_e is the electron density.

The estimated masses of dust and ionized gas are listed in Table 8. Dust masses are given only for galaxies in which we have found evidence for dust absorption.

Table 6. Hα+[NII] fluxes and luminosities

Galaxy	Dist.	A_R	$E_{B-V,\,int}$	Aper.	[NII]/Hα	[NII]/Hα	10^{14} $F_{H\alpha+[NII]}$	$L_{H\alpha}$
	[Mpc]	[mag]	[mag]	["]		(corr.)	[erg s^{-1} cm^{-2}]	[10^{39} erg s^{-1}]
(1)	(2)	(3)	(4)	(5)	(6)	(7)	(8)	(9)
NGC 596	39.58	0.075	—	—	—	—	< 0.28	< 0.19
NGC 720	35.76	0	—	—	—	—	< 1.56	< 0.84
NGC 821	37.70	0.100	—	—	—	—	< 0.68	< 0.40
NGC 1275	108.66	0.438	—	30	1.01	1.01	266.9 ± 36.	1608. ± 217
NGC 1395	29.76	0.006	—	23	...**	0.55	2.2 ± 0.3	1.4 ± 0.3
NGC 1399	26.38	0	—	23	—	—	4.2 ± 0.2	1.2 ± 0.1
NGC 1404	26.38	0	—	—	—	—	< 1.20	< 0.36
NGC 1407	31.36	0.100	—	10	—	—	0.9 ± 0.2	0.4 ± 0.2
NGC 1427	26.38	0	—	—	—	—	< 0.86	< 0.26
NGC 1537	22.72	0	—	—	—	—	< 1.92	< 0.42
NGC 1549	19.58	0	—	—	—	—	< 2.02	< 0.34
NGC 1700	81.14	0.075	—	—	—	—	< 0.28	< 0.74
NGC 2300	45.58	0.138	—	—	—	—	< 2.22	< 1.94
NGC 2325	40.82	0.600*	—	30	1.61	1.29	18.6 ± 2.4	13.7 ± 2.5
NGC 2974	34.54	0.069	0.05	32	4.57	2.17	16.3 ± 4.2	6.0 ± 2.2
NGC 2986	38.60	0.056	—	—	—	—	< 1.40	< 0.85
NGC 3136	28.26	0.419*	0.05	55	11.62	1.28	32.1 ± 7.9	11.4 ± 3.9
NGC 3193	23.88	0.050	—	—	—	—	< 12.2	< 2.92
NGC 3250	53.84	0.331	—	—	—	—	< 1.00	< 1.20
NGC 3377	13.32	0.038	0.03	13	—	—	11.9 ± 0.2	0.9 ± 0.1
NGC 3379	13.32	0.031	—	—	—	—	< 6.51	< 0.49
NGC 3557	54.32	0.344	—	18	2.82	1.37	18.4 ± 3.3	23.0 ± 6.0
NGC 3608	20.44	0	—	16	...**	0.91	26.0 ± 4.0	5.9 ± 0.9
NGC 3610	39.08	0	—	10	...**	...**	0.9 ± 0.1	0.6 ± 0.1
NGC 3613	39.08	0	—	—	—	—	< 1.96	< 1.26
NGC 3640	27.06	0.063	0.03	—	—	—	3.1 ± 0.5	1.0 ± 0.2
NGC 3706	49.48	0.225	—	—	—	—	< 0.41	< 0.47
NGC 3904	31.56	0.113	—	—	—	—	< 0.60	< 0.28
NGC 3962	27.80	0.025	0.06	28	3.31	1.82	40.6 ± 8.0	11.0 ± 3.1
NGC 4125	38.26	0.019	0.06	14	6.64	1.84	39.5 ± 6.0	20.1 ± 4.5
NGC 4261	40.98	0	0.03	4	4.19	3.49	6.6 ± 0.1	2.4 ± 0.1
NGC 4278	14.56	0.063	0.04	23	1.41	1.21	199.5 ± 24.	19.4 ± 3.3
NGC 4365	20.74	0	—	—	—	—	< 1.24	< 0.23
NGC 4374	20.74	0.081	0.08	25	4.12	1.54	21.6 ± 6.5	3.6 ± 1.5
NGC 4373	60.60	0.231	—	—	—	—	< 0.40	< 0.63
IC 3370	60.60	0.201	0.10	19	1.90	1.24	18.8 ± 1.5	31.2 ± 3.5
NGC 4473	20.74	0.025	—	—	—	—	< 8.24	< 1.66
NGC 4486	20.74	0.056	—	Not observed				
NGC 4494	22.44	0.038	0.03	Not observed				
NGC 4564	20.74	0.025	—	—	—	—	3.1 ± 0.3	0.6 ± 0.1
NGC 4589	36.60	0.025	0.06	19	2.80	1.23	14.4 ± 3.1	8.5 ± 2.6
NGC 4621	20.74	0.044	—	—	—	—	< 16.9	< 3.08
NGC 4660	20.74	0	—	6	—	—	4.0 ± 1.6	0.7 ± 0.4
NGC 4697	20.40	0.025	0.03	23	...**	1.79	29.5 ± 6.8	4.3 ± 1.4
NGC 4696	55.12	0.288	0.05	32	4.29	1.94	41.2 ± 5.8	41.9 ± 5.9
NGC 5018	50.34	0.138	0.06	32	...**	3.27	18.4 ± 7.0	10.4 ± 5.5
NGC 5044	50.34	0.069	0.05	50	2.48	1.89	55.4 ± 6.5	47.8 ± 8.0
NGC 5061	32.50	0.156	—	—	—	—	< 0.80	< 0.35
IC 4296	69.18	0.075	—	—	6.50	2.27	5.4 ± 0.4	10.9 ± 1.2
NGC 5322	42.12	0	—	18	...**	1.48	7.7 ± 1.9	5.5 ± 1.9
NGC 5576	30.36	0.025	0.03	7	—	—	3.3 ± 0.7	1.3 ± 0.3
NGC 5813	31.36	0.094	0.04	40	...**	1.32	22.6 ± 3.7	10.0 ± 2.3
NGC 6482	81.80	0.269	0.03	4	4.48	1.75	10.8 ± 1.8	26.0 ± 0.4
NGC 7144	36.04	0	—	—	—	—	< 0.82	< 0.46
IC 1459	33.12	0	0.05	55	3.24	2.24	147.0 ± 13.	48.5 ± 6.4
NGC 7507	32.06	0.125	0.03	—	—	—	< 1.42	< 0.62

Notes to Table 6:

The assumed distances as listed in Col. (2) are derived from the group velocities taken from Davies et al. (1987) and $H_0 = 50$ km s^{-1}Mpc^{-1}. The galactic foreground extinction values (taken from Burstein & Heiles 1984) are listed in Col. (3); values with an asterisk superscript are calculated using the cosecant approximation (cf. RSA). The average internal extinction values as derived from our colour index images are listed in Col. (4). The apertures (radii) over which the emission-line fluxes have been measured are given in Col. (5); upper limits have been measured using a *metric* aperture of radius 1 Kpc. The [NII]/Hα ratios (measured from our spectra) are given in Cols. (6) and (7); values in the latter column have been measured after subtraction of a template stellar absorption-line spectrum. Entries with a superscript (**) indicate that Hα is in absorption. The total Hα+[NII] fluxes are listed in Col. (8). The pure Hα luminosity is listed in Col. (9)

Table 7. Comparison with previous Hα+[NII] flux measurements

Galaxy	This paper		PJDSB	Kim		TdSA		Shields	
	Flux	r(″)	Flux	Flux	r(″)	Flux	r(″)	Flux	r(″)
(1)	(2)	(3)	(4)	(5)	(6)	(7)	(8)	(9)	(10)
NGC 720	<1.49	6	—	—	—	—	—	<3.53	6
NGC 1275	400. ± 39.	30	—	320. ± 32.	—	—	—	—	—
NGC 1395	2.1 ± 0.3	23	—	—	—	22.7 ± 0.5	35	< 17.	14
NGC 1407	0.8 ± 0.2	10	—	—	—	—	—	< 5.11	10
NGC 1549	<1.9	11	<1.56	—	—	—	—	—	—
NGC 2974	15.3 ± 3.9	32	—	31. ± 9.3	—	—	—	18.9 ± 5.0	14
NGC 3136	21.8 ± 5.4	55	19.5	—	—	—	—	—	—
NGC 3250	<0.70	4	<3.49	—	—	—	—	—	—
NGC 4125	33.2 ± 5.0	14	—	16. ± 1.6	—	—	—	—	—
NGC 4261	6.6 ± 0.1	4	—	9.6 ± 1.0	—	—	—	—	—
NGC 4365	<1.2	10	—	—	—	<0.8	15	<11.	8
NGC 4374	18.2 ± 5.5	25	—	21.0 ± 6.3	—	37.8 ± 7.5	50	25.3 ± 12.	12
NGC 4473	<8.05	10	—	—	—	—	—	<14.	8
NGC 4589	9.95 ± 2.2	19	—	4.7 ± 0.5	—	—	—	—	—
NGC 4621	<16.2	10	—	—	—	—	—	<13.4	8
NGC 4697	24.2 ± 5.6	23	—	—	—	4.7 ± 0.9	20.3	—	—
NGC 4696	28.2 ± 4.0	32	1.50	—	—	—	—	—	—
IC 4296	5.0 ± 0.4	6	—	—	—	—	—	23. ± 3.7	6
NGC 7144	<0.82	6	<0.92	—	—	—	—	—	—
IC 1459	131. ± 12.	55	25.9	—	—	—	—	82. ± 13.	15

Notes to Table 7:
PJDSB ≙ Phillips et al. (1986); Kim ≙ Kim (1989); TdSA ≙ Trinchieri & di Serego Alighieri (1991); Shields ≙ Shields (1991). The mentioned Hα+[NII] fluxes are in units of 10^{-14} erg s^{-1} cm^{-2}; no corrections for either Galactic foreground extinction or internal extinction by dust have been employed for this comparison. For this paper and for Shields, upper limits are 2σ, and uncertainties are 1σ. TdSA state uncertainties of $\leq 20\%$, and Kim states uncertainties of 10% except for NGC 2974 and NGC 4374 which are subject to errors of 30%. PJDSB fluxes are based on spectroscopic apertures of variable size, and Kim does not specify the apertures which he used for flux measurements.

4.3. *Descriptions for individual galaxies*

NGC 1275 = Perseus A. Central galaxy of the Perseus cluster, featuring two distinct, filamentary nebulosity systems which are ~ 3000 km s^{-1} apart in radial velocity (discovered by Minkowski 1957). NGC 1275 itself is associated with the "low-velocity system" of ionized gas. NGC 1275 was included in the original list of Seyfert galaxies (Seyfert 1943). The distribution of the ionized gas in NGC 1275 consists of a very luminous nucleus and various filament-like features (see, e.g., the famous picture of Lynds 1970). The B image of NGC 1275 exhibits many regions of absorption (see also the photographic plate of Adams 1977). These features do not obviously show up in colour index images due to the presence of strong emission lines in the broad-band bandpasses and various regions with evidence of recent star formation (e.g., Kent & Sargent 1979). The distribution of dust patches is much better revealed by an A_V image, which has been produced by division of the V image by a purely elliptical model fit (cf. Nørgaard-Nielsen et al. 1993). Comparing the A_V image with the Hα+[NII] image of the *low-velocity system* (both are shown in Fig. 1, reproduced from Nørgaard-Nielsen et al. 1993), it can be seen that the absorption features in NGC 1275 generally do *not* show up in the distribution of ionized gas, implying that at least some of the dust patches are situated behind the filamentary system of ionized gas. Conversely, the dust patches are distributed similar to the *high-velocity system* of ionized gas. We argue in a companion paper (Nørgaard-Nielsen et al. 1993) that most dust patches are associated with the high-velocity system which is moving through NGC 1275. NGC 1275 exhibits strong far-infrared emission in all IRAS passbands (Jura et al. 1987), and is a strong

source of extended radio and X-ray emission. Molecular gas has also been detected (Lazareff et al. 1989).

NGC 1395. The Hα+[NII] image reveals slightly extended line emission peaked on the nucleus. Neither our image nor our spectrum confirms the large extent of the emission-line region reported by Trinchieri & di Serego Alighieri (1991). The $B-I$ image does not reveal obvious dust absorption. Since this galaxy has been detected by IRAS at 60 and 100 μm, we expect the dust to be in a face-on distribution (cf. also the symmetrical distribution of the ionized gas, Trinchieri & di Serego Alighieri 1991). Shells revealed in residual image (see also Malin & Carter 1983). Radio and X-ray source.

NGC 1399 = Fornax I. Our Hα+[NII] image reveals emission from the nuclear region. IRAS 100 μm detection, but no obvious dust associated with the emission-line gas. This may be due to orientation effects. Extended radio source. X-ray emission.

NGC 1407. Marginal detection of line emission centered on the nucleus. The $B-V$ image reveals a circumnuclear 'ring' which is slightly redder ($\Delta(B-V) \sim 0.01$) than the nucleus. This feature is probably real since the point spread function of the B and V images are well matched as can be judged from stars in the field of view. Detected at 60 and 100 μm by IRAS. Radio source. X-ray emission.

NGC 2325. Hα+[NII] line emission strongly peaked on the nucleus, and extended along PA 36°, which differs significantly from the apparent principal axes of the stellar body of the galaxy. There is some evidence for a spiral-like distribution in the outer parts of the emission region. The nuclear spectrum reveals a hitherto unknown broad component of the Hα line (FWHM $\sim$ 3800 km s^{-1}), reminiscent of a Seyfert I nucleus. The $B-V$ image does not reveal obvious dust absorption.

NGC 2974. The HI 21 cm line has been detected in this galaxy with a rather regular distribution which is consistent with a rotating disk or ring along the (apparent) major axis of the galaxy (Kim et al. 1988). Previous imaging studies have shown the existence of a dust lane and ionized gas along the major axis (e.g., Kim 1989). The present $B-I$ image reveals a similar distribution of the dust absorption, with some additional amorphous substructure at $\sim 10''$ NE of the nucleus. The Hα+[NII] image shows a rather regular gas disk associated with the dust lane, with additional evidence for warped outer structure. The emission-line spectrum exhibits very broad wings to the Hα line. X-ray source with extended halo (Forman et al. 1985). Nuclear radio source. Detected by IRAS at 60 and 100 μm. Our broad-band images confirm the presence of weak spiral arm structure as was previously reported in this galaxy (see Roberts et al. 1993).

NGC 3136. The Hα+[NII] image reveals extended emission peaking on the nucleus and extending slightly to the SW. In addition, a peculiar arm-like feature is extending out to $\sim 55''$ from the centre. The $B-I$ image reveals dust absorption associated with the ionized gas. The [NII]λ6583 to Hα ratio is 1.28. Detected by IRAS at 60 μm.

NGC 3377. Our images reveal a slightly warped dust lane. The presence of dust in this galaxy was already implied by the detection of 60 and 100 μm emission by IRAS (Jura et al. 1987). The dust lane is probably associated with a gaseous disk. We must however add a note of caution in this respect. Our emission-line image shows an extended, regular distribution to the SE, but is strangely abridged to the NW. This effect is usually the result of incorrect alignment or PSF matching of the on– and off-line images; however, all stellar objects in the images of NGC 3377 have been aligned perfectly within only 0.001 pixel with no obvious PSF matching problems. In any case, the presence of ionized gas in NGC 3377 requires confirmation.

NGC 3557. The Hα+[NII] image reveals line emission extended in the North-South direction. The outer isophotes of the line emission twist gradually towards the apparent major axis of the galaxy. The $B-V$ image only shows a symmetric colour gradient with no evidence for obvious dust absorption associated with the ionized gas. The [NII]λ6583 to Hα ratio at the centre is 1.37. Detected by IRAS at 60 and 100 μm. Bright radio elliptical.

NGC 3608. Hα+[NII] line emission centered on the nucleus, and extended symmetrically along the continuum isophotes. The emission extends out to $r \sim 15''$, corresponding to $\sim$ 1.5 Kpc. The $B-I$ image shows a symmetric colour gradient with no evidence for obvious dust absorption associated with the ionized gas; this may not be surprising since the ionized gas distribution seems to be nearly face-on. The [NII]λ6583 to Hα ratio at the nuclear position is 0.91, which is significantly lower than average for this sample; it suggests photoionization by stellar radiation as in HII regions. Radio source.

NGC 3610. This galaxy exhibits a prominent, edge-on stellar disk along the major axis in the inner regions (see, e.g., Scorza & Bender 1990). Our Hα+[NII] image reveals weak line emission associated with the central regions of the disk. The $B-I$ image shows that the stellar disk has a slightly *bluer* colour than the surrounding regions ($\Delta(B-I) = 0.12$). This may be due to a younger stellar population; the fact that the Hα line remains in absorption after subtraction of the absorption-line template from the nuclear spectrum is consistent with this view. No obvious dust absorption. Detected by IRAS at 100 μm. Radio source.

NGC 3640. Small dust lane along the minor axis, previously reported by Prugniel et al. (1988). The Hα+[NII] image shows a marginal detection of line emission from the central region.

NGC 3962. The Hα+[NII] image reveals prominent line emission with a disky inner structure which is clearly misaligned with the apparent principal axes of the stellar body. In addition, a peculiar outer arm-like feature is present which departs from the major axis of the disky structure and crosses the stellar body; it extends to $\sim 50''$ from the centre, corresponding to ~ 7 Kpc. The $B-I$ image reveals dust absorption associated with the inner regions of the gas distribution. Conversely, the outer arm-like feature seems to be associated with a *bluer* colour compared to the surrounding regions. However, this result needs confirmation using broad-band images with a very high signal-to-noise ratio. Detected by IRAS at 60 and 100 μm. Nuclear radio source.

NGC 4125. The B isophotes are significantly distorted in the inner $\sim 30''$ due to a prominent dust lane (see also Kim 1989) which shows signs of warps in its outer parts. The dust lane is inclined by $\sim 10°$ with respect to the apparent major axis of the galaxy, and more extended to the E side of the centre. The Hα+[NII] image shows line emission associated with the dust lane. Detected by IRAS at 60 and 100 μm. Nuclear radio source.

NGC 4261. Möllenhoff & Bender (1987) and Kim (1989) reported the presence of a dust lane elongated along the major axis. However, our $B-V$ image does not confirm this; we *do* find a colour gradient in the sense that the central regions are redder than the surroundings (as is the case in virtually all sample ellipticals, cf. Paper I), and a red nucleus. We note that we obtained this final colour index image after careful alignment (accuracy: 0.002 pixel) and PSF matching. The red nucleus may be associated with the nuclear dusty disk reported by Jaffe et al. (1993) using HST Planetary Camera observations. The Hα+[NII] image shows strong line emission in the centre only. The optical spectrum shows a typical LINER spectrum with [NII]/H$\alpha = 3.5$ and unusually broad wings to the emission lines. Marginal detections by IRAS at 60 and 100 μm. Powerful two-lobed radio galaxy with two jets emanating from the centre along PA 88°, which is essentially perpendicular to the nuclear dusty disk (Birkinshaw & Davies 1985; Jaffe et al. 1993).

NGC 4278. Elliptical galaxy with large HI ring, inclined by $\sim 45°$ to the line of sight (Raimond et al. 1981). The outer contours of the ionized gas distribution in our Hα+[NII] image have an axis ratio of ~ 0.74 which indicates an inclination of $\sim 48°$ to the line of sight if the contours are intrinsically circular in space. The ionized gas may thus be physically associated with the neutral gas which is located further out. The $B-I$ image reveals prominent patchy dust out to $\sim 25''$ (see also Ebneter et al. 1988), most prominently on the northern side of the nucleus. Although the extinction in the dust patches N of the nucleus amounts to $E_{B-I} \sim 0.12$ mag, no sign of obscuration is seen in the Hα+[NII] image. This suggests that the dust patches are located (at least partially) *behind* the ionized gas.

NGC 4374. Prominent skewed dust lane in central region (see also Hansen et al. 1985; Kim 1989), associated with ionized gas. Detected by IRAS at 60 and 100 μm. X-ray emission. Classical double lobed radio galaxy. The orientation of the dust lane is perpendicular to that of the radio continuum emission (Kotanyi & Ekers 1979).

IC 3370. Prominent dustlane in central region (see also Sadler & Gerhard 1985), associated with Hα+[NII] emission. Nearly square isophotes at larger radii (cf. Jarvis 1987). Molecular gas has been detected in this galaxy (Lees et al. 1991). Detected by IRAS at 60 and 100 μm. Nuclear radio source.

NGC 4473. The stellar disk as revealed by CCD surface photometry (Paper I; Bender et al. 1988) is found to be significantly *bluer* ($\Delta(V-I) \sim 0.12$) than the surrounding regions of the galaxy. No trace of Hα+[NII] emission.

NGC 4486 = Virgo A. Powerful radio emitter with prominent radio and optical jet associated with low surface-brightness radio lobes (Birkinshaw & Davies 1985). Dust was not detected in a previous search using a colour index image (Véron-Cetty & Véron 1988). Also the present $B-I$ image provides no obvious evidence for dust. However, the A_B image reveals some low-level dust absorption which seems to be associated with the Hα+[NII] jet found by Jarvis (1990) (see also Sparks et al. 1993). Powerful radio and X-ray emitter.

NGC 4494. Small dustlane along minor axis. We do not have narrow-band images of this galaxy. Residual image reveals low surface brightness galaxy at 1.'4 NE of the nucleus. Detected by IRAS at 60 μm and at radio wavelengths.

NGC 4564. This galaxy has a fairly prominent stellar disk along its apparent major axis (cf. Paper I). Our Hα+[NII] image shows emission in its nucleus, but we do not have spectra to confirm this.

NGC 4589. The $B-I$ and Hα+[NII] images reveal a prominent dust lane with associated ionized gas extending $\sim 20''$ along PA 173° which is close to that of the minor axis (see also Möllenhoff & Bender 1989). The ionized gas shows a LINER type spectrum. Detected by IRAS at 60 and 100 μm. This galaxy has been detected in the ^{12}CO($J = 1-0$) line (Sofue & Wakamatsu 1993). X-ray source with compact radio source.

NGC 4660. Galaxy with a prominent stellar disk along its apparent major axis. The Hα+[NII] image reveals the presence of ionized gas in the central region of the disk structure. The presence of associated dust is not obvious from the $B-I$ image, and this galaxy has not been detected in the far-infrared. However, the third and fourth order Fourier terms behave differently in B, V, and I in the inner 6″, which has been shown to be a sensitive indicator for the presence of dust.

NGC 4697. E6 galaxy with stellar disk along the apparent major axis (cf. also Carter 1987). Neither Véron-Cetty & Véron (1988) nor Kim (1989) found evidence for the presence of dust, and our $B-I$ image only reveals a very red nucleus. However, the presence of cool gas in this galaxy is strongly suggested by its significant IRAS flux densities (e.g., S_{100} = 1.10 Jy), and the detection of molecular gas (Sofue & Wakamatsu 1993). This suggests that the dust is primarily distributed like the stars; this may partially be the cause of the radial colour gradient of NGC 4697, which is quite large compared with its radial metallicity gradient as measured by the Mg_2 index (see Peletier 1989). A marginal detection of ionized gas was reported by Trinchieri & di Serego Alighieri (1991); Kim (1989) reported a nondetection. However, we find quite significant detections in both our Hα+[NII] image and our emission-line spectrum. The ionized gas is extended over a radius of $\sim$ 35″. Marginal detection of X-ray emission, with a possibly large contribution from discrete stellar sources (Canizares et al. 1987).

NGC 4696. Brightest galaxy of the Centaurus cluster. The $B-I$ image clearly reveals the previously reported, prominent dust lane shaped like a horseshoe (e.g., Jørgensen et al. 1983, Sparks et al. 1989), associated with Hα+[NII] emission. Evidence for a dynamically decoupled stellar substructure has been reported by Danziger & Focardi (1988). Detected by IRAS at 60 and 100 μm. Extended radio emission. Powerful X-ray emission.

NGC 5018. The isophotes of this galaxy are quite irregular, especially in the B passband; it has been considered to be a strong candidate for a galaxy merger remnant in view of the presence of prominent ripples and shells (e.g., Schweitzer 1987). Although previous studies reported only marginal detections of emission lines (Caldwell 1984; Kim 1989), our Hα+[NII] image reveals the presence of extended emission-line gas distributed like a (strongly) warped disk. The very centre does *not* show emission, due to a strong Hα absorption line as revealed by the nuclear spectrum (cf. Appendix B) . The emission-line gas is accompanied by a complex system of prominent dust lanes and patches as revealed by the colour index images; the dust patches are most prominent on the NW side of the galaxy nucleus, which may be the cause of the lack of Hα+[NII] emission from those regions. However, close inspection of the colour index images reveals that the distribution of ionized gas is associated with a region (of the same morphology) with a clearly *bluer* colour (e.g., $\Delta\, B-V \simeq 0.12$) than its surroundings. This suggests that the ionized gas is associated with star forming regions. In this respect it is interesting to note that NGC 5018 has one of the lowest nuclear magnesium absorption-line strengths relative to its absolute magnitude among known giant elliptical galaxies (Schweitzer et al. 1990), and Bertola et al. (1993) conclude that NGC 5018 is a giant, metal-poor elliptical by comparing its IUE spectrum—which covers the central $\sim$ 7″—with that of M 32 (which is metal-poor with respect to giant ellipticals). However, these conclusions are based upon the nuclear region only. As mentioned above, this region has a significantly bluer colour than the outer regions of the galaxy. Furthermore, the recent study of Carollo & Danziger (1993) shows a strong decrease of the Mg_2 index inside $\sim$ 7″ from the centre; if their radial Mg_2 profile were extrapolated from outer radii to the centre, the Mg_2 index would be normal for its luminosity. This evidence suggests the presence of a relatively young stellar population in the central region of NGC 5018. This may have been driven by a past merger event, causing the dilution of the Mg_2 index in the central region (see also Schweitzer 1987). Detected by IRAS at 60 and 100 μm. Radio source.

NGC 5044. Very extensive emission-line filament system, with a rather irregular distribution bearing very little if any relationship with the B isophotes. The $B-I$ image reveals dust absorption in the inner 10″, reminiscent of a ring structure (see Goudfrooij 1991). Marginally detected by IRAS at 60 and 100 μm. Nuclear radio source. Powerful, extended X-ray emission (Fabbiano et al. 1992).

IC 4296. Hα+[NII] emission detected in the inner 5″. No obvious dust absorption. Detected by IRAS at 60 and 100 μm. Bright, extended radio source. X-ray emission.

NGC 5322. This boxy galaxy contains a stellar disk along its major axis in the inner $\sim$ 9″ (cf. Paper I). Kim (1989) did already search for dust and ionized gas in this galaxy, but reported no detection. However, our Hα+[NII] image reveals extended emission which is elongated along the major axis and may thus be physically associated with this disk. Our $B-I$ image does not reveal obvious associated dust absorption. Detected by IRAS at 60 and 100 μm. Radio source. X-ray emission.

NGC 5576. The $B-I$ and Hα+[NII] images show marginal traces of dust and ionized gas in the central regions of the galaxy. However, these features require confirmation since our data are relatively noisy, and Kim (1989) reported nondetections. Marginal IRAS detections at 60 & 100 μm.

NGC 5813. The Hα+[NII] image shows extended emission-line gas with a rather peculiar distribution bearing no similarity to that of the stellar body of the galaxy. The emission-line gas is associated with patchy dust as revealed by the $V-I$ image (cf. also Peletier 1989). Radio source.

NGC 6482. The Hα+[NII] image reveals the presence of emission-line gas in the nucleus, supported by the spectral data. The $V-I$ image shows a red nucleus. Radio source.

IC 1459. This galaxy is an archetypical merger candidate in view of the presence of a fast, counter-rotating stellar core (Franx & Illingworth 1988). Furthermore, spiral-like structure has been found in both the outer regions using a deep photograph (Malin 1985) and the distribution of extended ionized gas (Goudfrooij et al. 1990). The $B-V$ image (cf. also Sparks et al. 1985; Goudfrooij et al. 1990) shows an asymmetric distribution in the inner $\sim 15''$ which is most probably due to dust absorption, and a general similarity to the Hα+[NII] image. A small, low surface-brightness galaxy is found at $35''$ NW of the galaxy nucleus. Strongest IRAS source at 60 and 100 μm of the sample. Compact, powerful nuclear radio source. X-ray emission.

NGC 7507. This very round galaxy exhibits an extended region of dust absorption on the SW side of the nucleus, thereby confirming the findings of Sparks et al. (1985). We do not find significant evidence for the presence of ionized gas.

5. Summary and discussion

We have found that 23 ellipticals (i.e., 41%) out of the total of 56 luminous elliptical galaxies in our complete, optical magnitude-limited sample either definitely or very probably contain dust, either in patches or in well-defined lanes or rings. This detection rate is higher than results of previous optical searches (Sadler & Gerhard 1985; Ebneter et al. 1988; Véron-Cetty & Véron 1988), and similar to that reported by Knapp et al. (1989) using co-added IRAS flux densities. The optical detection rates represent lower limits, since the detection of dust features from optical imaging data is dependent on the signal-to-noise of the data and the precise intrinsic three-dimensional distribution of the absorbing regions with respect to that of the stars. For instance, absorbing regions which are present in the outer regions of the galaxies are undetectable for reasons of local signal-to-noise. Furthermore, a significant number of galaxies classified as elliptical is found to contain small stellar disks (e.g., Paper I); differences in the stellar populations of the disk- and spherical components further hamper the detection of dust in these galaxies. Finally, orientation effects on the dust optical depth are expected to be important. A rough estimate of the effect of

Table 8. Estimated masses of dust and ionized gas

Galaxy (1)	$\log \frac{M(dust)}{M_\odot}$ (2)	$\log \frac{M(HII)}{M_\odot}$ (3)	IRAS detection (4)
NGC 596	—	< 2.65	—
NGC 720	—	< 3.29	—
NGC 821	—	< 2.97	—
NGC 1275	6.26	6.40 ± 0.06	*
NGC 1395	—	3.51 ± 0.09	*
NGC 1399	—	3.45 ± 0.04	*
NGC 1404	—	< 2.92	*
NGC 1407	3.47	2.97 ± 0.22	*
NGC 1427	—	< 2.78	—
NGC 1537	—	< 2.99	*
NGC 1549	—	< 2.90	*
NGC 1700	—	< 3.24	—
NGC 2300	—	< 3.66	—
NGC 2325	—	4.50 ± 0.08	—
NGC 2974	4.94	4.15 ± 0.16	*
NGC 2986	—	< 3.27	*
NGC 3136	4.77	4.42 ± 0.15	*
NGC 3193	—	< 3.83	—
NGC 3250	—	< 3.45	—
NGC 3377	3.98	3.32 ± 0.05	*
NGC 3379	—	< 3.62	—
NGC 3557	—	4.73 ± 0.11	*
NGC 3608	—	4.14 ± 0.07	—*
NGC 3610	—	3.15 ± 0.07	*
NGC 3613	—	< 3.47	—
NGC 3640	4.29	3.37 ± 0.09	—
NGC 3706	—	< 3.07	*
NGC 3904	—	< 2.67	*
NGC 3962	4.65	4.41 ± 0.12	*
NGC 4125	5.52	4.67 ± 0.10	*
NGC 4261	4.28:	3.75 ± 0.02	*
NGC 4278	4.35	4.66 ± 0.07	*
NGC 4365	—	< 2.73	*
NGC 4374	4.49	3.92 ± 0.18	*
NGC 4373	—	< 3.15	—
IC 3370	5.53	4.86 ± 0.05	*
NGC 4473	—	< 3.59	—
NGC 4486	3.16	—	*
NGC 4494	3.91	—	*
NGC 4564	—	3.15 ± 0.07	—
NGC 4589	4.90	4.30 ± 0.13	*
NGC 4621	—	< 3.86	—
NGC 4660	—	3.21 ± 0.25	—
NGC 4697	4.40	4.00 ± 0.14	*
NGC 4696	5.69	4.99 ± 0.06	*
NGC 5018	5.72	4.38 ± 0.22	*
NGC 5044	4.36	5.05 ± 0.07	*
NGC 5061	—	< 1.97	—
IC 4296	—	4.40 ± 0.05	*
NGC 5322	—	4.11 ± 0.15	*
NGC 5576	3.51	3.48 ± 0.10	*
NGC 5813	3.97	4.37 ± 0.10	—
NGC 6482	4.02	4.78 ± 0.01	—
NGC 7144	—	< 3.03	*
IC 1459	5.26	5.05 ± 0.06	*
NGC 7507	5.00	< 3.16	—

Notes to Table 8:
Column (2) lists the dust masses as estimated from the colour index images. Entries with a colon indicate uncertain values which are calculated assuming that the red nucleus is entirely due to dust absorption. Masses of ionized gas as estimated from the emission-line images are listed in Col. (3). Column (4) states whether or not the galaxy has been detected by IRAS in the 60 and/or 100 μm bands. NGC 3608 has not been observed by IRAS

Table 9. Summary of optical imaging results

Galaxy	Remarks
NGC 1275	Dust patches in northern part of galaxy; filamentary structure of ionized gas
NGC 1395	Ionized gas in central region
NGC 1399	Ionized gas in central region
NGC 1407	Marginal evidence for ionized gas in central region; red ring-like structure surrounding centre
NGC 2325	Ionized gas along skewed axis, with outer spiral-like structure
NGC 2974	Dust and ionized gas along major axis, with evidence for outer warps
NGC 3136	Dust and ionized gas centered on nucleus, with filament to the NE
NGC 3377	Dust and ionized gas along major axis
NGC 3557	Ionized gas along skewed axis in inner $\sim 5''$, and twisting towards major axis in outer regions
NGC 3608	Ionized gas roughly along continuum isophotes
NGC 3610	Weak central line emission along major axis
NGC 3640	Dust lane along minor axis; marginal line emission
NGC 3962	Dust and ionized gas along skewed axis, with spiral-like filamentary outer structure
NGC 4125	Warped dust lane and ionized gas along major axis
NGC 4261	Possible dust along major axis; ionized gas in centre
NGC 4278	Patchy dust; ionized gas along skewed axis
NGC 4374	Dust lane and ionized gas along skewed axis
IC 3370	Dust lane and ionized gas centered on nucleus and extending to SW
NGC 4486	Patchy dust, possibly associated with jet-like feature of ionized gas*
NGC 4494	Small dust lane along minor axis
NGC 4564	Ionized gas in the centre
NGC 4589	Dust lane and ionized gas along minor axis
NGC 4660	Red nucleus and ionized gas along major axis in central $5''$
NGC 4697	Red nucleus and low-level Hα+[NII] emission, roughly along continuum isophotes
NGC 4696	Dust and ionized gas in dust lane with "horse shoe" shape
NGC 5018	Patchy dust on northern side of galaxy and ionized gas along major axis, warped in outer parts
NGC 5044	Extensive spiral-like filaments of ionized gas; central dusty ring-like structure
IC 4296	Ionized gas in centre
NGC 5322	Ionized gas along major axis
NGC 5576	Marginal evidence for dust and ionized gas along minor axis
NGC 5813	Irregularly distributed dust and ionized gas
NGC 6482	Red nucleus and ionized gas in centre
IC 1459	Ionized gas along major axis, with spiral-like distribution in outer regions; dust patches in centre
NGC 7507	Irregular dusty region on SW side of nucleus

* cf. Jarvis (1990)

orientation on the observed fraction of ellipticals containing dust can be made as follows. Combining the galaxies in the samples of this paper and those of Véron-Cetty & Véron (1988) and Kim (1989), we find a total of 19 elliptical (and S0) galaxies exhibiting dust lanes or rings that are sufficiently regular to allow an estimate of the inclination. The inclinations are found to range between 0° and 35°, i.e., dust lanes or rings are detected from about half the total solid angle on the sky. This is similar to the result of Sadler & Gerhardt (1985) who used ESO/SRC photographic plates of 10 'discless' galaxies. Assuming that this result is entirely due to the selection effect that dust lanes are detected only if inclined by less than a certain critical angle, one would expect that the true fraction of ellipticals containing dust is about twice as high as the observed one, i.e., of order 80%. This percentage may need some further adjustment since dust in elliptical galaxies is also often distributed in patches which are less subject to this selection effect. 34 elliptical galaxies in our sample (i.e., 61%) have been detected by the IRAS satellite at 60 and/or 100 μm (cf. Table 8). This detection rate is not inconsistent with our estimate of 80%; more sensitive future ISO data will shed more light on this matter.

Ionized gas has been detected in 32 ellipticals in our sample (57%). This detection rate is significantly higher than that of the imaging study of Shields (1991; 39%) who used an X-ray selected sample of 46 E and S0 galaxies. Moreover, our detection rate is similar to that of Kim

(1989; 58%) who used a sample of 26 E and S0 galaxies that are detected in at least two IRAS bands, whereas our sample selection is not biased towards the presence of any kind of interstellar matter. This illustrates that the presence of dust and ionized gas in elliptical galaxies is indeed the rule rather than the exception. Our detection rate is also similar to that of the most recent spectroscopic survey of E and S0 galaxies by Phillips et al. (1986; 55–60%), who claimed a limiting equivalent width of 0.5 Å.

Table 9 summarizes the morphological characteristics of the detected dust and ionized gas. The dust and ionized gas show a wide variety of distributions—extended along either the apparent major axis, or the minor axis, or a skewed axis, indicating that triaxiality is in general required as a galaxy figure (see, e.g., van Albada et al. 1982; Merritt & de Zeeuw 1983). For a total of 11 galaxies, no previous optical detection of dust or ionized gas has been reported according to the NED database[2]. In a substantial number of the galaxies in our sample (i.e., NGC 1275, NGC 2325, NGC 3136, NGC 3962, NGC 4696, NGC 5018, NGC 5044, NGC 5813, IC 1459, NGC 7507), the interstellar matter has a irregular or filamentary distribution, suggestive of a recent interaction event.

In our sample galaxies, ionized gas is detected in virtually all galaxies with dust (a notable exception is NGC 7507), and dust is detected in 23 of the galaxies with ionized gas (i.e., 68%, or 41% of the total sample). The latter discrepancy is consistent with orientation effects as mentioned above, since the ionized gas in the galaxies in which we have found no evidence for associated dust absorption is generally found to be either concentrated to the central few seconds of arc in the galaxy, or to have roundish isophotes, consistent with e.g., a face-on disk. Furthermore, a glance at Figs. 1–34 show that the dust and ionized gas in the detected galaxies are usually distributed similarly, irrespective of the particular distribution of dust (along the major axis, minor axis, or skewed axis). This indicates that the cold and warm (ionized) gas seem to be (physically) associated, which may provide important clues to the origin and subsequent evolution of the interstellar medium in elliptical galaxies (cf. Sect. 1).

The dataset presented in this paper will be used as a tool for investigating the relationship of the dust and ionized gas with other galaxy properties. This will be dealt with in forthcoming papers.

Acknowledgements. We are grateful to the European Southern Observatory, the Panel for Allocation of Telescope Time, and the Danish Board for Astronomical Research for allocating observing time to this project. The members of the scientific and technical support staff of the European Southern Observatory and the La Palma Observatory are gratefully acknowledged for their help during the observations. We thank Dave Carter and Bobby van den Hoek for performing observations for this project. PG acknowledges travel support by the Netherlands Organization for Scientific Research (NWO), the Leids Kerkhoven-Bosscha Fonds (LKBF), and the European Southern Observatory. The Jacobus Kapteyn Telescope, the Isaac Newton Telescope, and the William Herschel Telescope are operated on the island of La Palma by the Royal Greenwich Observatory in the Spanish Observatorio del Roque de los Muchachos of the Instituto de Astrofisica de Canarias. We have made use of the NASA/IPAC Extragalactic Database (NED) which is operated by the Jet Propulsion Laboratory, Caltech, under contract with the National Aeronautics and Space Administration. This paper is part of the Ph. D. thesis of P. Goudfrooij who joined this research project in October 1988.

[2]The NASA/IPAC Extragalactic Database (NED) is operated by the Jet Propulsion Laboratory, California Institute of Technology, under contract with the National Aeronautics and Space Administration

References

Adams T.F. 1977, PASP 89, 488
Argyle R.W., Mayer C.J., Pike C.D., Jorden P.R. 1989, La Palma User Manual No. 18: A user guide to the JKT CCD camera
Bender R., Döbereiner S., Möllenhoff C. 1988, A&AS 74, 385 (BDM)
Bender R., Surma P., Döbereiner S., Möllenhoff C., Madejsky R. 1989, A&A 217, 35
Bertola F., Galletta G., Zeilinger W.W. 1985, ApJL 292, L51
Bertola F., Bettoni D. 1988, ApJ 329, 102
Bertola F., Burstein D., Buson L.M. 1993, ApJ 403, 573
Bica E. 1988, A&A 195, 76
Birkinshaw M., Davies R.L. 1985, ApJ 291, 31
Bohlin R.C., Savage B.D., Drake J.F. 1978, ApJ 224, 132
Bregman J.E., O'Connell R.W., McNamara B.R. 1990, ApJ 351, 406
Burstein D., Heiles C. 1984, ApJS 54, 33
Burstein D., Davies R.L., Dressler A., Faber S.M., Stone R.P.S., Lynden-Bell D., Terlevich R., Wegner G. 1987, ApJS 64, 601
Caldwell N. 1984, PASP 96, 287
Caldwell N., Krishner R.P., Richstone D.O. 1986, ApJ 305, 136
Canizares C.R., Fabbiano G., Trinchieri G. 1987, ApJ 312, 503
Carollo C.M., Danziger I.J. 1993, in: Structure, Dynamics and Chemical Evolution of Elliptical Galaxies, ESO Conference & Workshop proceedings No. 45, eds. I.J. Danziger, W.W. Zeilinger & K. Kjär, p. 431
Carollo C.M., Danziger I.J., Buson L.M. 1993, MNRAS 265, 553
Carter D. 1987, ApJ 312, 514

Danziger I.J., Focardi P. 1988, in: Cooling Flows in Clusters and Galaxies, ed. A.C. Fabian (Dordrecht: Kluwer) p. 133
Davies R.L., Burstein D., Dressler A., Faber S.M., Lynden-Bell D., Terlevich R.J., Wegner G. 1987, ApJS 64, 581
Davies R.L., Sadler E.M., Peletier R.F. 1993, MNRAS 262, 650
de Jong T., Nørgaard-Nielsen H.U., Hansen L., Jørgensen H.E. 1990, A&A 232, 317
de Vaucouleurs G. 1959, Handb. Phys. 53, 275
de Vaucouleurs G., de Vaucouleurs A., Corwin H.G. 1976, Second Reference Catalog of Bright Galaxies (Univ. of Texas press, Austin) (RC2)
Draine B.T., Salpeter E. 1979, ApJ 231, 77
Ebneter K., Djorgovski S., Davis M. 1988, AJ 90, 183
Fabbiano G., Kim D.-W., Trinchieri G. 1992, ApJS 80, 531
Faber S.M., Gallagher J.S. 1976, ApJ 204,365
Fabian A.C., Nulsen P.E.J., Canizares C.R. 1991, A&AR 2, 191
Forbes D.A., Thomson R.C. 1992, MNRAS 254, 723
Forman W., Jones C., Tucker W. 1985, ApJ 293, 102
Franx M., Illingworth G.D. 1988, ApJL 327, L55
Franx M., Illingworth G.D., Heckman T.M. 1989, AJ 98, 538 (FIH)
Gorgas J, Efstathiou G., Aragón Salamanca A. 1990, MNRAS 245, 217
Goudfrooij P. 1991, The ESO Messenger, 63, 42
Goudfrooij P., Nørgaard-Nielsen H.U., Hansen L., Jørgensen H.E., de Jong T. 1990, A&A 228, L9
Goudfrooij P., Hansen L., Nørgaard-Nielsen H.U., Jørgensen H.E., de Jong T., van den Hoek L.B. 1993, A&AS, in press (Paper I)
Hansen L., Nørgaard-Nielsen H.U., Jørgensen H.E. 1985, A&A 149, 442
Hogg D.E., Roberts M.S., Sandage A. 1993, AJ , in press (NRAO preprint)
Hubble E. 1926, ApJ 64, 321
Jaffe W., Ford H.C., Ferrarese L., van den Bosch F., O'Connell R.W. 1993, Nature 364, 213
Jarvis B.J. 1987, AJ 94, 30
Jarvis B.J. 1990, A&A 240, L8
Jørgensen H.E., Nørgaard-Nielsen H.U., Pedersen H., Rasmussen I.L., Schnopper H. 1983, A&A 122, 301
Jørgensen I., Franx M., Kjærgaard P. 1992, A&AS 95, 489
Jura M., Kim D.-W., Knapp G.R., Guthathakurta P. 1987, ApJL 312, L11
Kent S.M. 1984, ApJS 56, 105
Kent S.M., Sargent W.L.W. 1979, ApJ 230, 667
Kim D.-W. 1989, ApJ 346, 653
Kim D.-W., Guharthakurta P., van Gorkom J.H., Jura M., Knapp G.R. 1988, ApJ 330, 684
Kim D.-W., Fabbiano G., Trinchieri G. 1992, ApJS 80, 645
Knapp G.R., Guharthakurta P., Kim D.-W., Jura M. 1989, ApJS 70, 329
Kotanyi C.G., Ekers R.D. 1979, A&A 73, L1
Lazareff B., Castets A., Kim D.-W., Jura M. 1989, ApJL 336, L13
Lees J.F., Knapp G.R., Rupen M.P., Phillips T.G. 1991, ApJ 379, 177
Lynds R. 1970, ApJL 159, L151
Malin D.F. 1985, in: New Aspects of Galaxy Photometry, ed. J.-L. Nieto (Berlin:Springer-Verlag) p. 27
Massey P., Strobel K., Barnes J.V., Anderson E. 1988, ApJ 328, 315
Merritt D., de Zeeuw P.T. 1983, ApJL 267, L19
Minkowski R. 1957, in: Radio Astronomy, IAU Symposium No. 4, ed. H.C. van der Hulst, p. 107
Möllenhoff C. 1982, A&A 108, 130
Möllenhoff C., Bender R. 1987, A&A 174, 63
Möllenhoff C., Bender R. 1989, A&A 214, 61
Nørgaard-Nielsen H.U., Jørgensen H.E. 1984, Phys. Scr. T7, 174
Nørgaard-Nielsen H.U., Goudfrooij P., Hansen L., Jørgensen H.E. 1993, A&A 279, 61
Oke J.B. 1974, ApJS 27, 21
Oke J.B., Gunn J.E. 1983, ApJ 266, 713
Osterbrock D.E.: 1974, Astrophysics of Gaseous Nebulae (W.H. Freeman & Co., San Francisco)
Peletier R.F. 1989, Ph. D. Thesis, University of Groningen
Peletier R.F., Davies R.L., Illingworth G.D., Davis L.E., Cawson M. 1990, AJ 100, 1043
Phillips M.M., Jenkins C.R., Dopita M.A., Sadler E.M., Binette L. 1986, AJ 91, 1062
Prugniel P., Nieto J.-L., Bender R., Davoust E. 1988, A&A 204, 61
Raimond E., Faber S.M., Gallagher J.S. III, Knapp G.R. 1981, ApJ 246, 708
Roberts M.S., Hogg D.E., Bregman J.N. 1993, in: Structure, Dynamics and Chemical Evolution of Elliptical Galaxies, ESO workshop proceedings No. 45, p. 563
Sadler E.M., Gerhardt O.E. 1985, MNRAS 214, 177
Sandage A. 1961, The Hubble Atlas of Galaxies, Carnegie Institution of Washington
Sandage A., Tammann G.A. 1981, A Revised Shapley-Ames Catalog of Bright Galaxies, Carnegie Institution of Washington (RSA)
Savage B.D., Mathis J.S. 1979, ARA&A 17, 84
Schweizer F. 1987, in Structure and Dynamics of Elliptical Galaxies, IAU Symposium No. 127, ed. P.T. de Zeeuw (Dordrecht: Reidel) p. 109
Schweitzer F., Seitzer P., Faber S.M., Burstein D., Dalle Ore C., Gonzalez J.J. 1990, ApJL 364, L33
Scorza C., Bender R. 1990, A&A 235, 49
Seyfert C.K. 1943, ApJ 97, 28
Sharples R.M., Carter D., Hawarden T.G., Longmore A.J. 1983, MNRAS 202, 37
Shields J.C. 1991, AJ 102, 1314

Sofue Y., Wakamatsu K. 1993, PASJ 45, 529
Sparks W.B., Wall J.V., Thorne D.J., Jorden P.R., van Breda I.G., Rudd P.J., Jørgensen H.E. 1985, MNRAS 217, 87
Sparks W.B., Macchetto F., Golombek D. 1989, ApJ 345, 153
Sparks W.B., Ford H.C., Kinney A.L. 1993, ApJ 413, 531
Stone R.P.S. 1977, ApJ 218, 767
Stone R.P.S., Baldwin J.A. 1983, MNRAS 204, 347
Trinchieri G., di Serego Alighieri S. 1991, AJ 101, 1647
Tüg H. 1977, The ESO Messenger 11, 7
van Albada T.S., Kotanyi C.G., Schwarzschild M. 1982, MNRAS 198, 303
Véron-Cetty M.P., Véron P. 1986, A&AS 66, 335
Véron-Cetty M.P., Véron P. 1988, A&A 204, 28
Yahil A., Tammann G.A., Sandage A. 1977, ApJ 217, 903

A. Morphologies of dust and ionized gas for individual galaxies

In Figs. 1–34 we present CCD images of sample galaxies showing, unless stated otherwise, for each galaxy isophotal contours of the B-band image (top), a $B-I$ colour index image (middle), and an Hα+[NII] emission-line image with the continuum subtracted. For each galaxy the images are aligned and on the same scale. North is up and east is to the left. The grey scale goes from blue (white) to red (black) in the colour index images, and from low to high intensity in the emission-line images. The contour levels are indicated in the captions for each image as: lowest level (step) highest level, or by mentioning all contour levels separated by a comma. The levels are expressed in mag arcsec^{-2}, except for the emission-line images which are expressed in units of 10^{-16} erg s^{-1} cm^{-2} arcsec^{-2}.

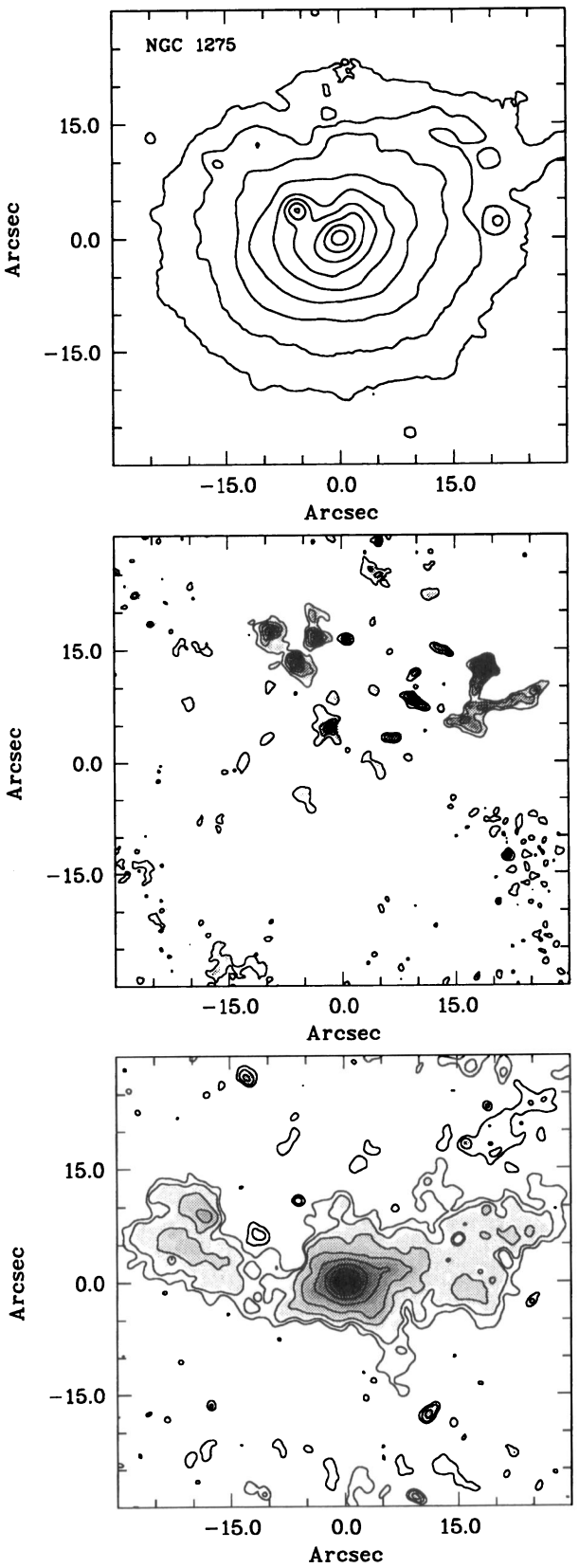

Fig. 1. NGC 1275. B (top): 23.0 (0.5) 19.0; Av (middle): 0.08 (0.10) 0.48; Hα+[NII] (bottom): 3., 6., 12., 24., 48., 96., 192., 384

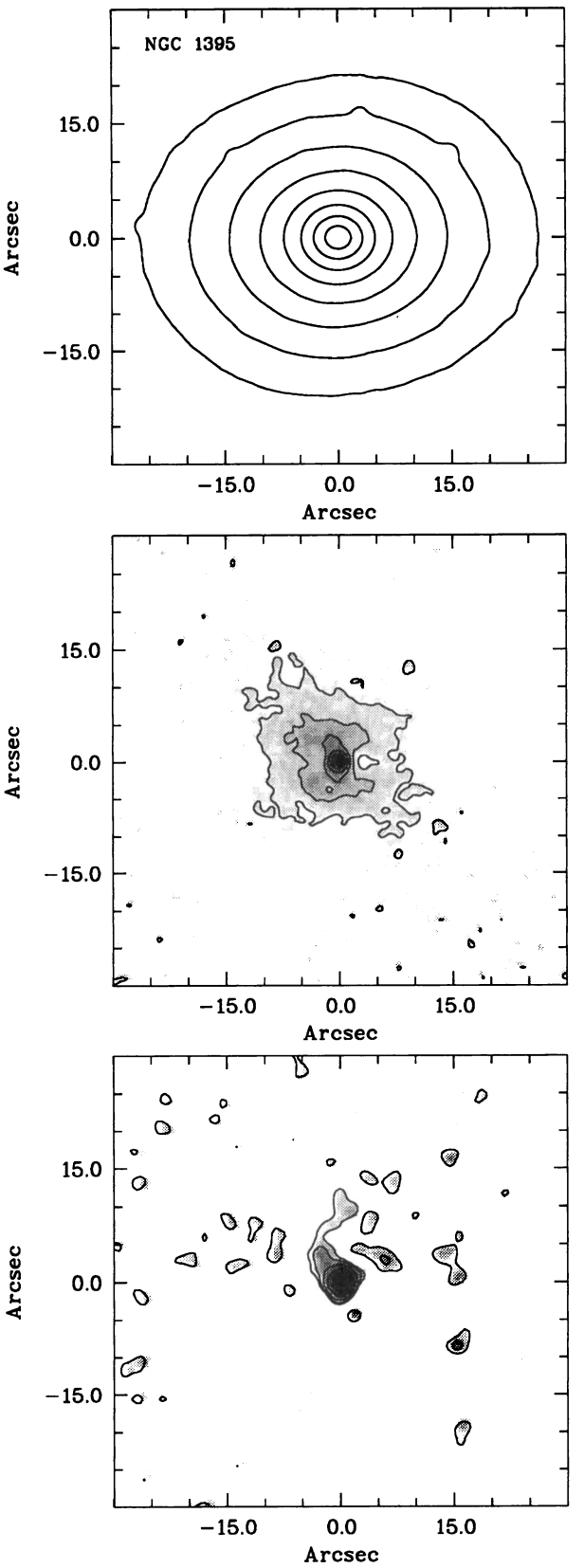

Fig. 2. NGC 1395. B (top): 21.5 (0.5) 18.0; $B-V$ (middle): 1.06 (0.01) 1.12; Hα+[NII] (bottom): 0.7, 1.4, 2.8, 5.6, 11.2

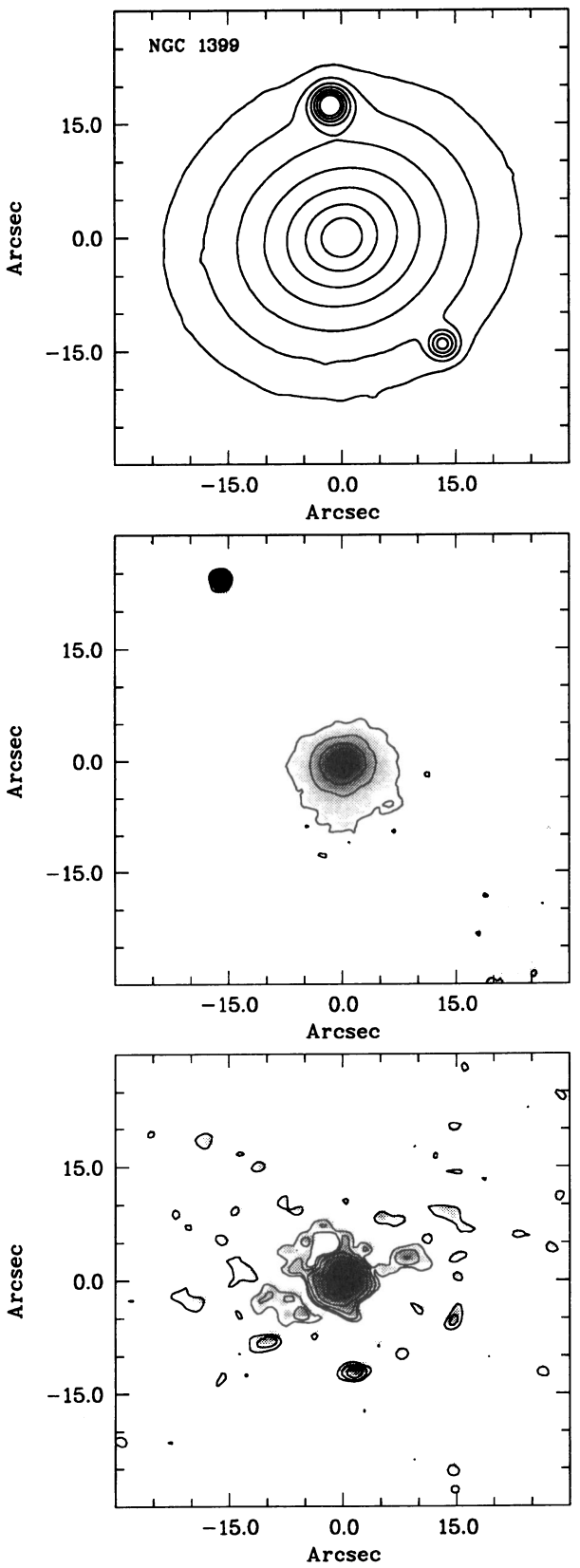

Fig. 3. NGC 1399. B (top): 21.0 (0.5) 18.0; $B-I$ (middle): 2.42 (0.04) 2.58; Hα+[NII] (bottom): 0.4, 0.8, 1.6, 3.2, 6.4, 12.8

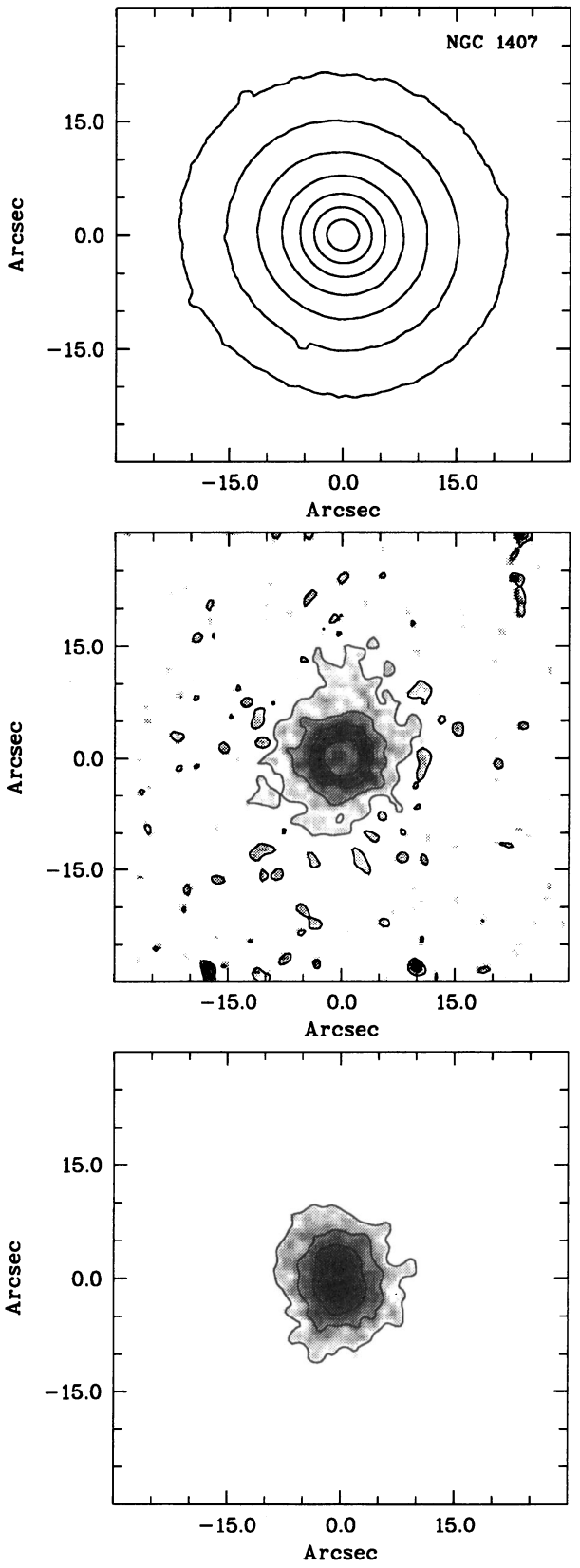

Fig. 4. NGC 1407. B (top): 18.0 (0.5) 21.5; $B-V$ (middle): 1.13 (0.01) 1.16; Hα+[NII] (bottom): 0.5, 1.0, 2.0, 4.0

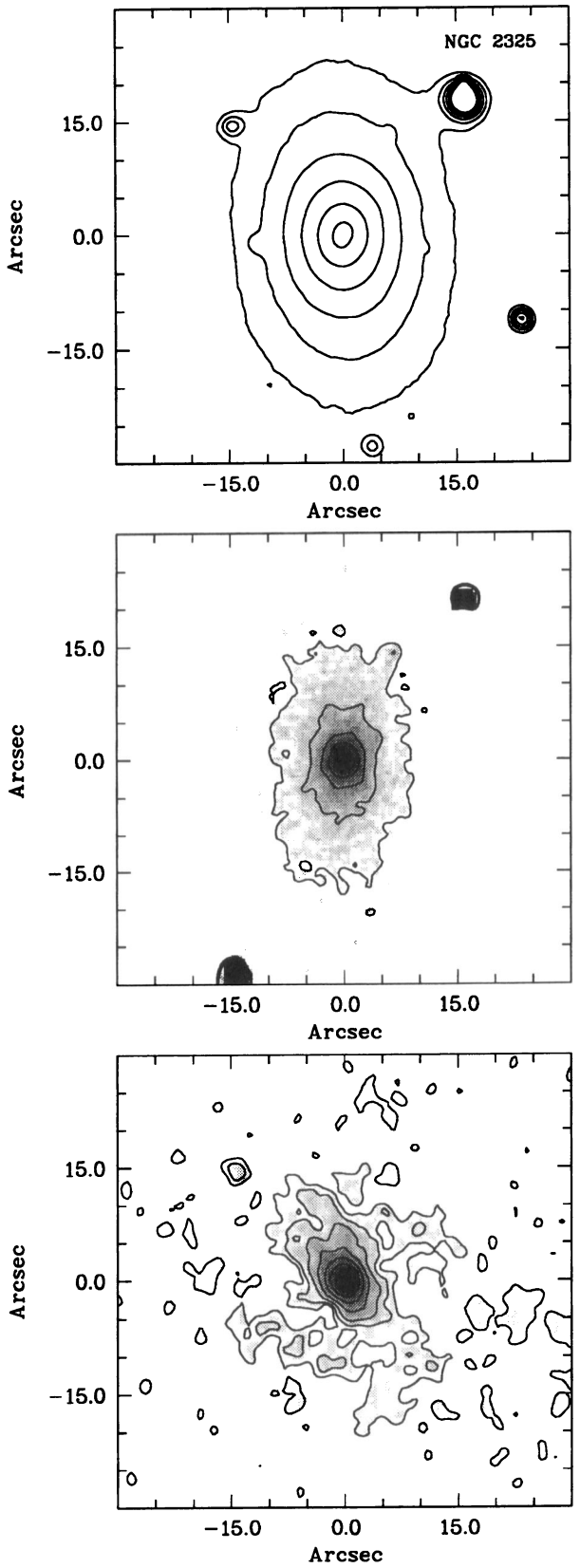

Fig. 5. NGC 2325. B (top): 22.5 (0.5) 20.0; $B-V$ (middle): 1.14 (0.04) 1.34; Hα+[NII] (bottom): 0.7, 1.4, 2.8, 5.6, 11.2, 22.4, 44.8

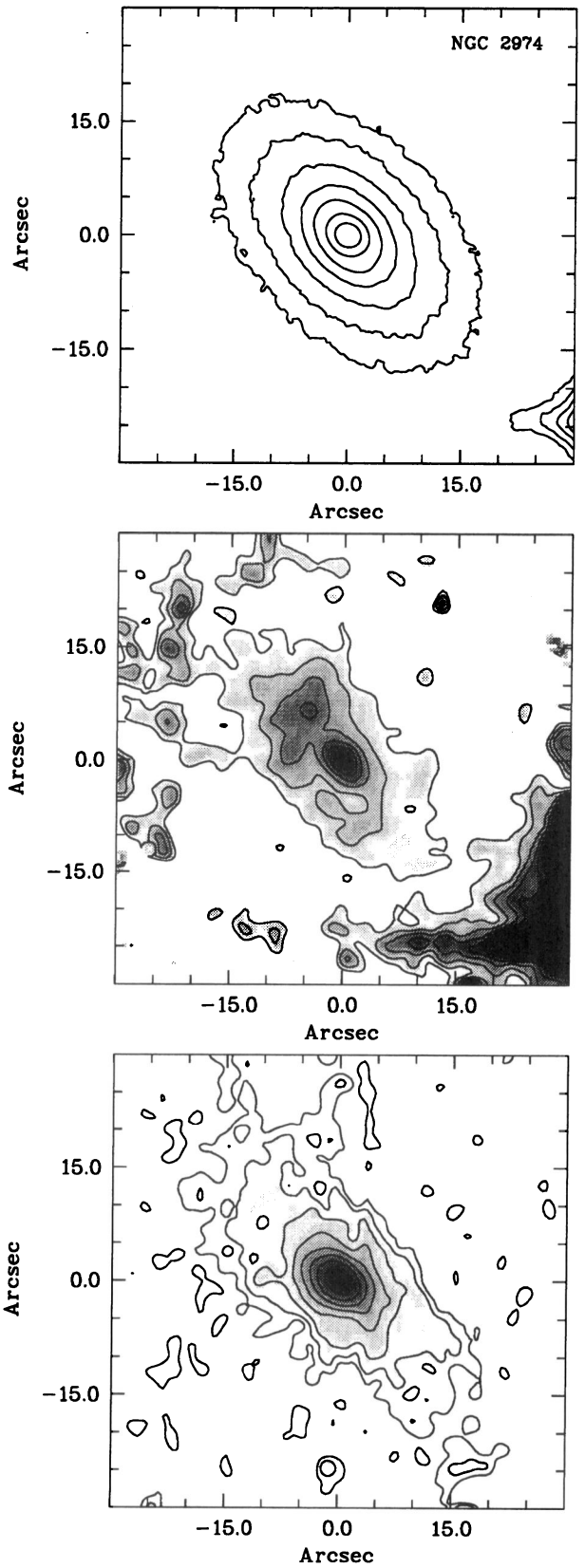

Fig. 6. NGC 2974. B (top): 21.5 (0.5) 18.5; $B-I$ (middle): 2.28 (0.04) 2.52; Hα+[NII] (bottom): 0.7, 1.4, 2.8, 5.6, 11.2, 22.4, 44.8, 89.6, 150

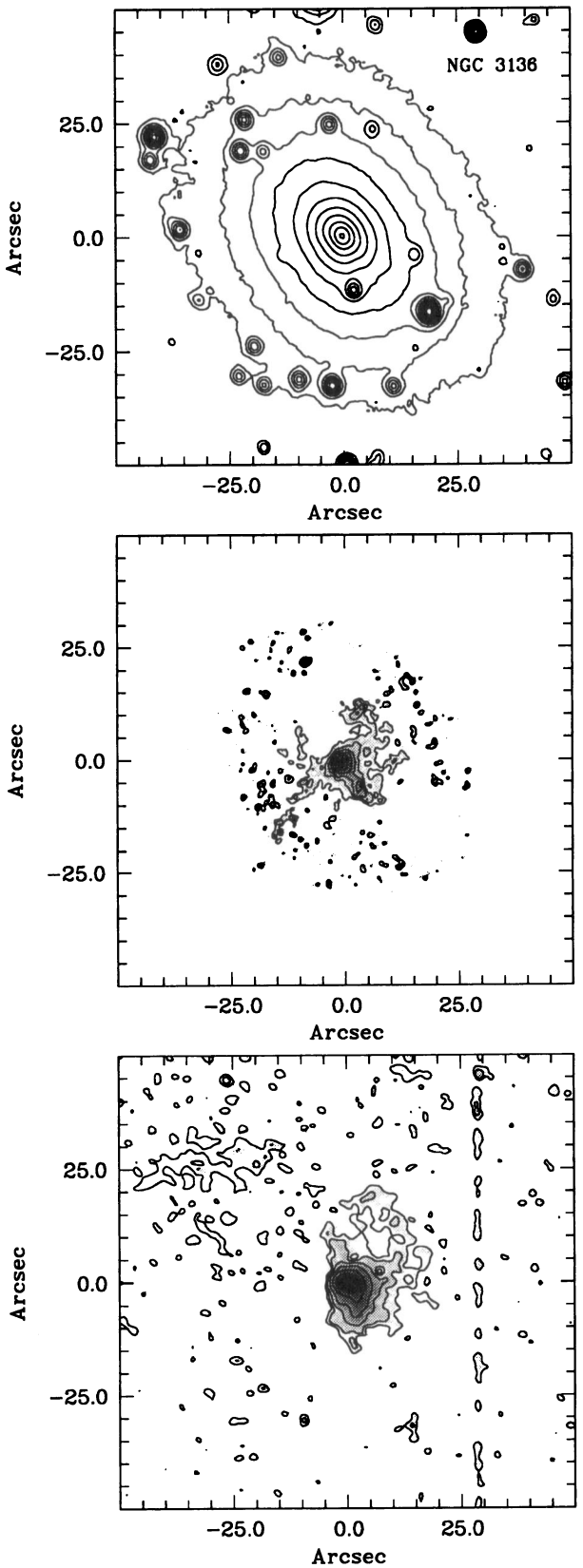

Fig. 7. NGC 3136. B (top): 23.5 (0.5) 18.5; $B-I$ (middle): 2.32 (0.03) 2.50; Hα+[NII] (bottom): 0.9, 1.8, 3.6, 7.2, 14.4, 28.8, 57.6

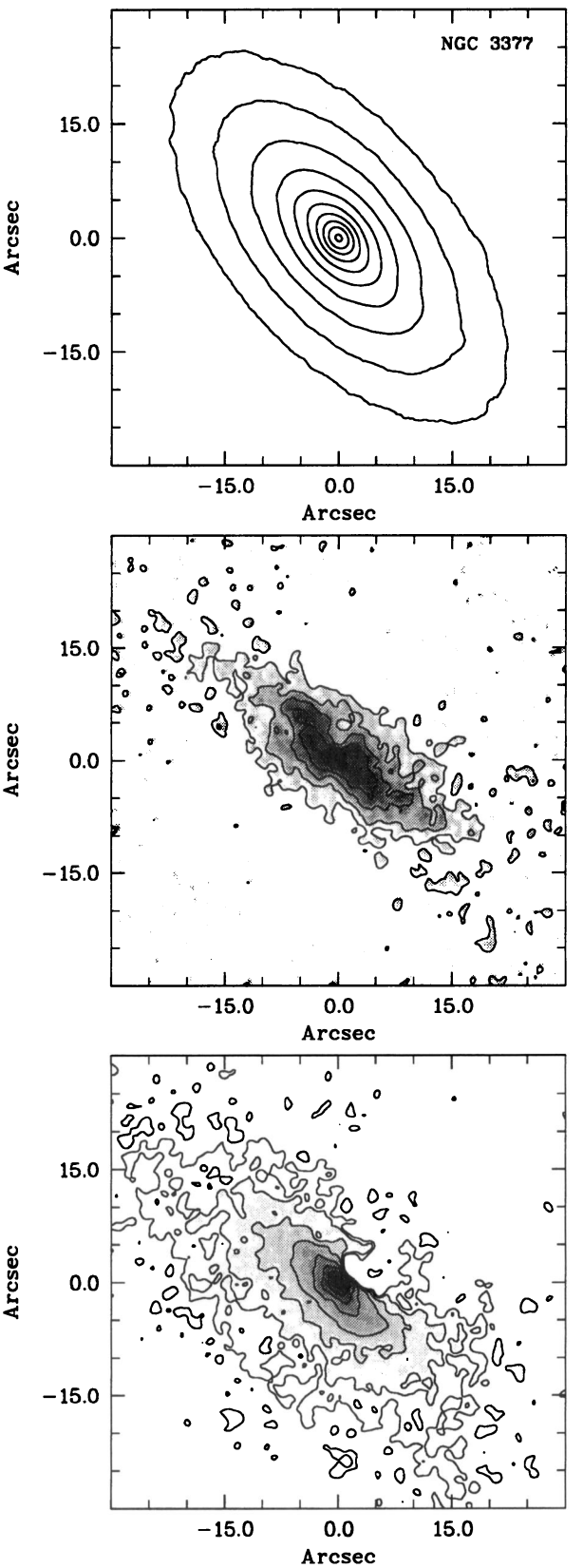

Fig. 8. NGC 3377. B (top): 21.5 (0.5) 17.0; $B-I$ (middle): 1.67 (0.03) 1.82; Hα+[NII] (bottom): 0.9, 1.8, 3.6, 7.2, 14.4, 28.8, 57.6, 115.2; see Sect. 4.3 for comments on Hα+[NII] image

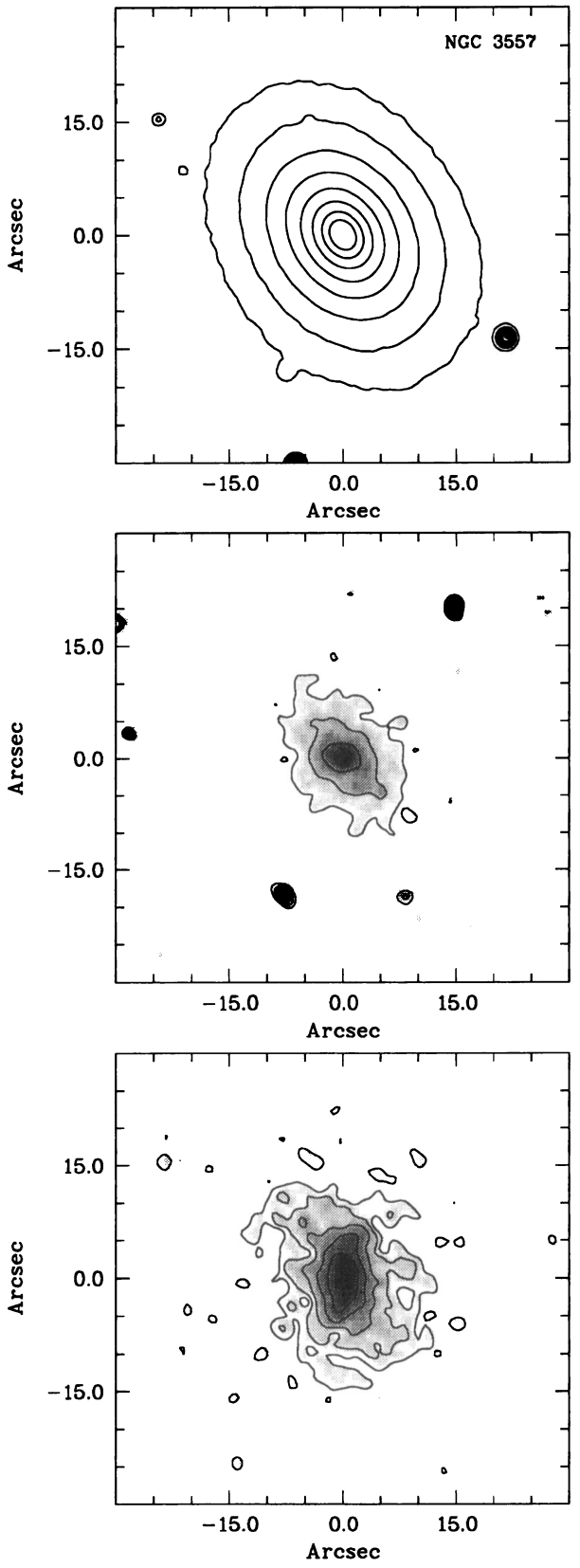

Fig. 9. NGC 3557. B (top): 22.5 (0.5) 19.0; $B-V$ (middle): 0.91 (0.02) 0.99; Hα+[NII] (bottom): 0.8, 1.6, 3.2, 6.4, 12.8, 25.6

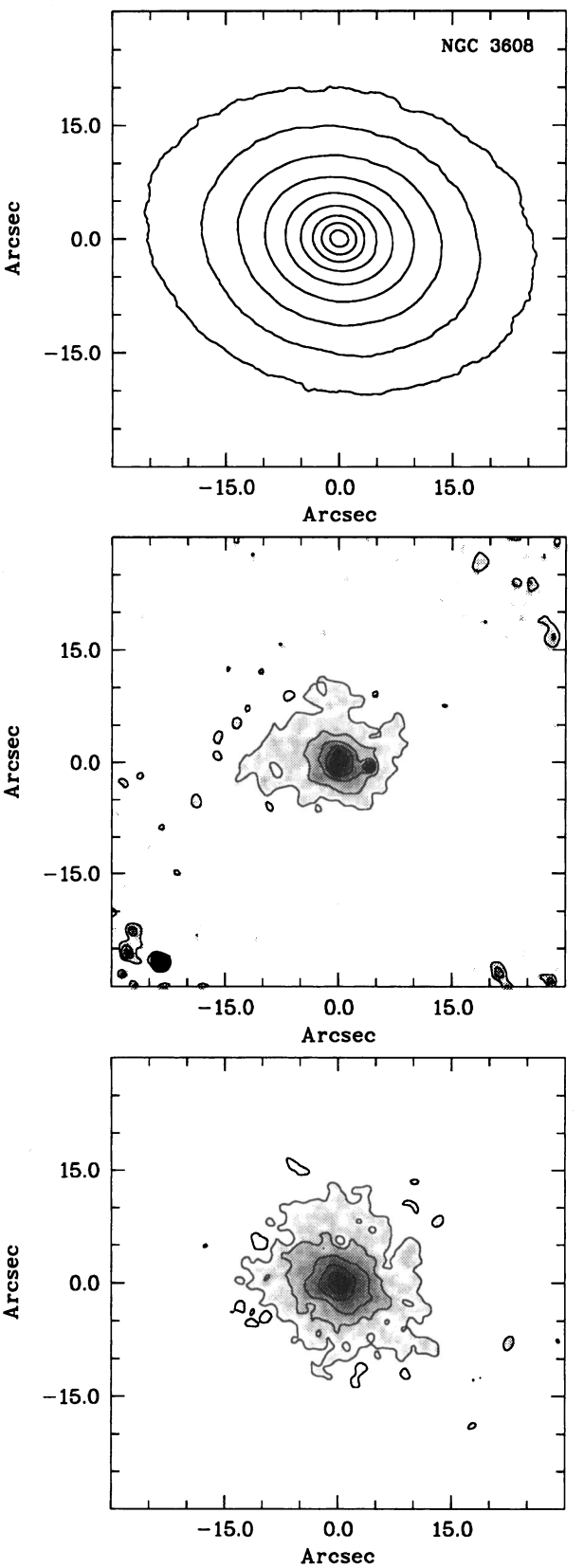

Fig. 10. NGC 3608. B (top): 22.5 (0.5) 18.5; $B-I$ (middle): 2.27 (0.03) 2.42; Hα+[NII] (bottom): 1.5, 3.0, 6.0, 12., 24., 36

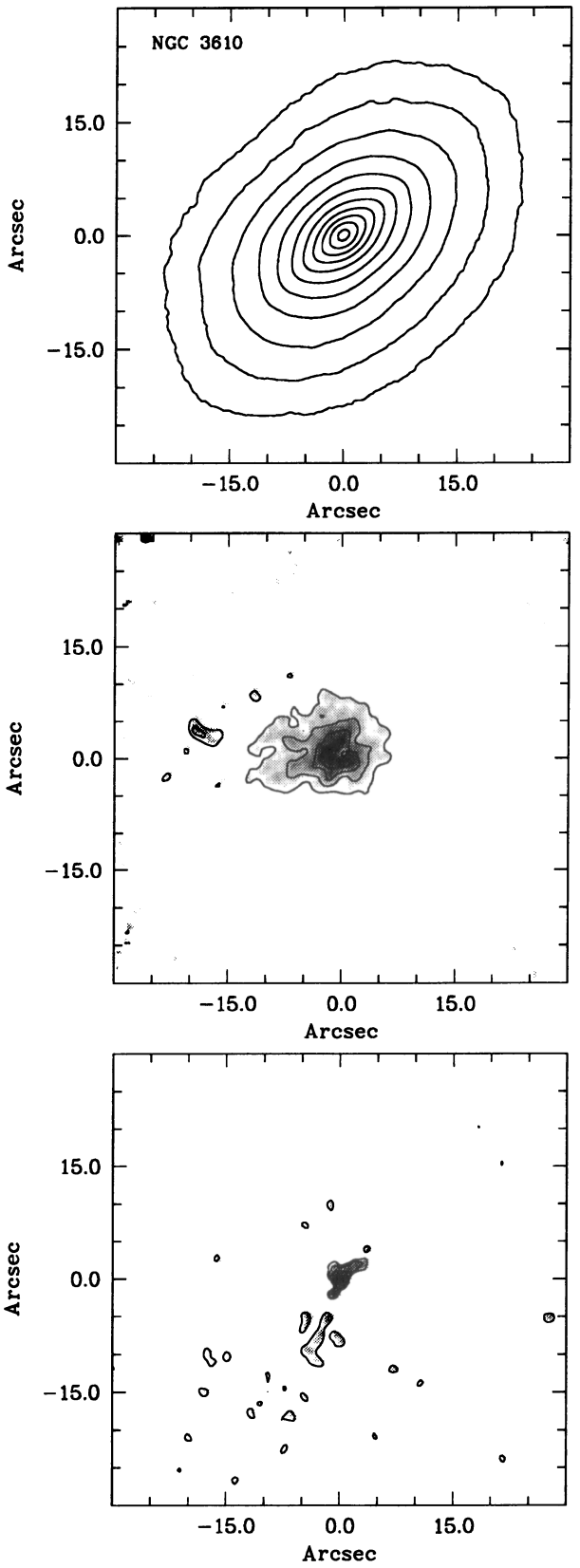

Fig. 11. NGC 3610. B (top): 22.0 (0.5) 17.0; $B-I$ (middle): 1.98 (0.03) 2.10; Hα+[NII] (bottom): 0.9, 1.8, 3.6, 7.2

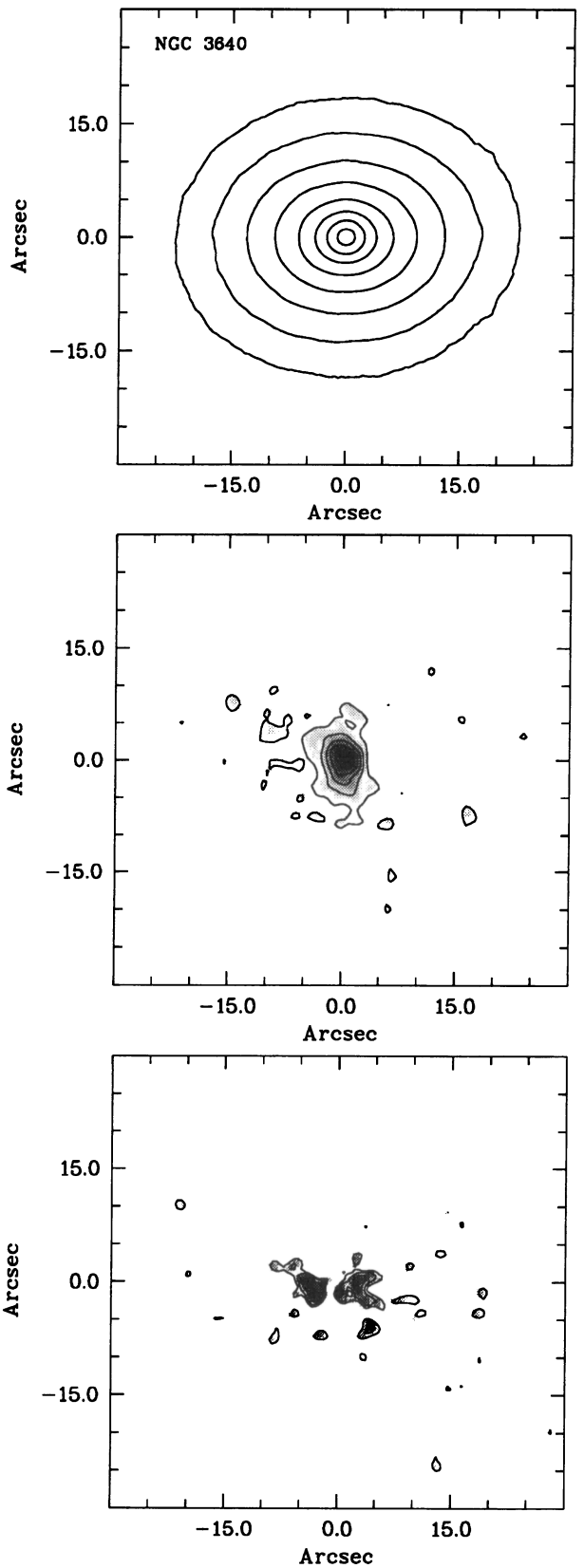

Fig. 12. NGC 3640. B (top): 22.0 (0.5) 18.0; $B-V$ (middle): 0.92 (0.03) 1.07; Hα+[NII] (bottom): 1.5, 3.0, 6.0, 12.0

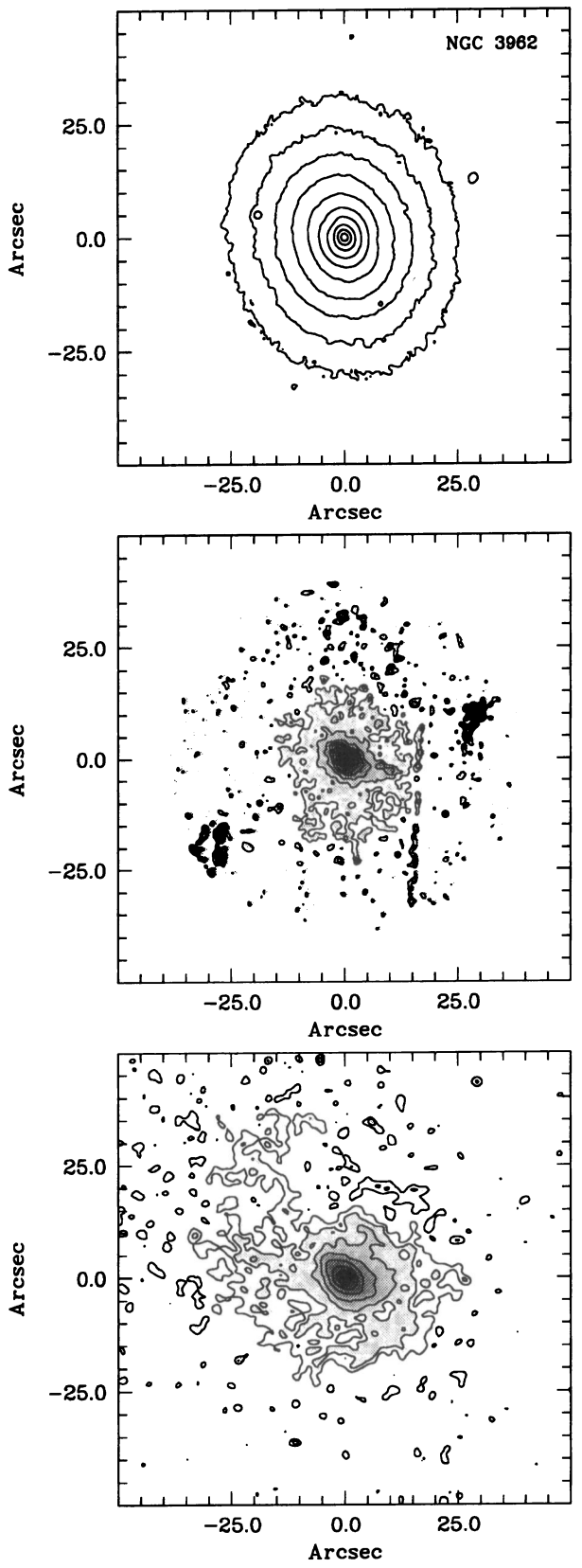

Fig. 13. NGC 3962. B (top): 22.5 (0.5) 18.0; $B-I$ (middle): 2.17 (0.04) 2.41; Hα+[NII] (bottom): .65, 1.3, 2.6, 5.2, 10.4, 20.8, 41.6, 83.2

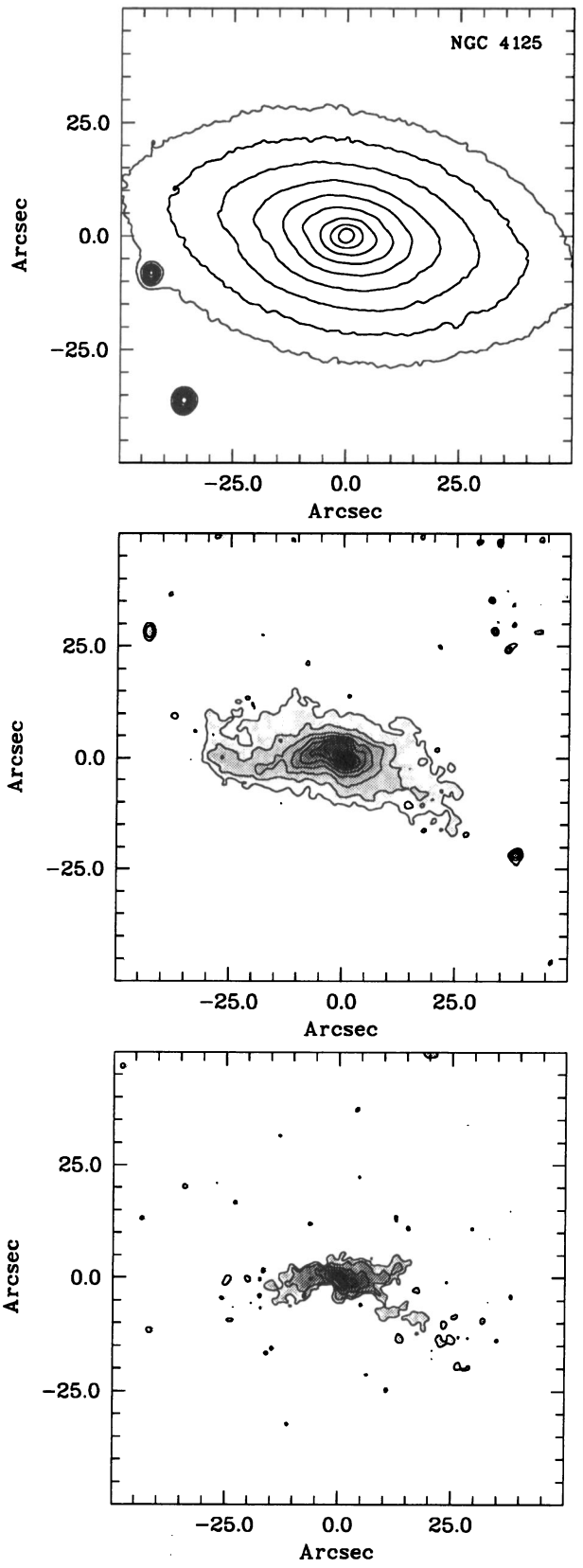

Fig. 14. NGC 4125. B (top): 22.0 (0.5) 18.0; $B-I$ (middle): 2.02 (0.04) 2.38; Hα+[NII] (bottom): 5., 10., 20., 40., 80

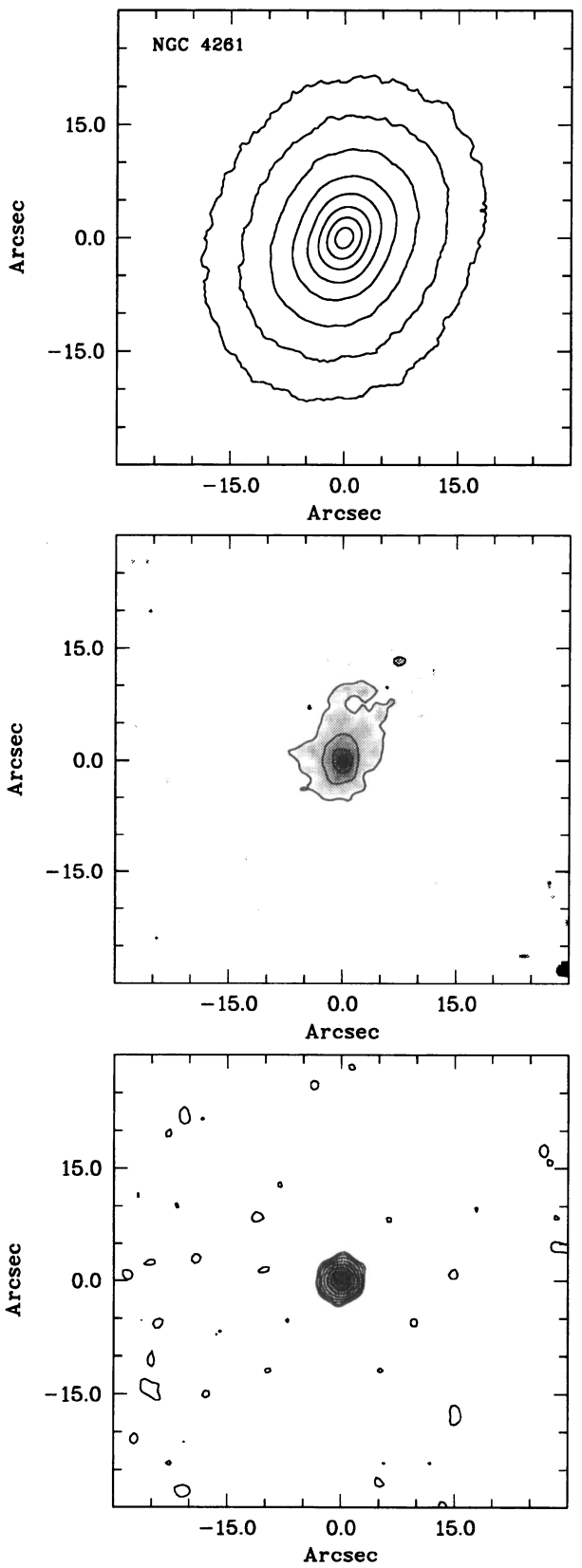

Fig. 15. NGC 4261. B (top): 23.0 (0.5) 19.0; $B-V$ (middle): 0.95 (0.02) 1.01; Hα+[NII] (bottom): 0.9, 1.8, 3.6, 7.2, 14.4, 28.8, 57.6, 115.2

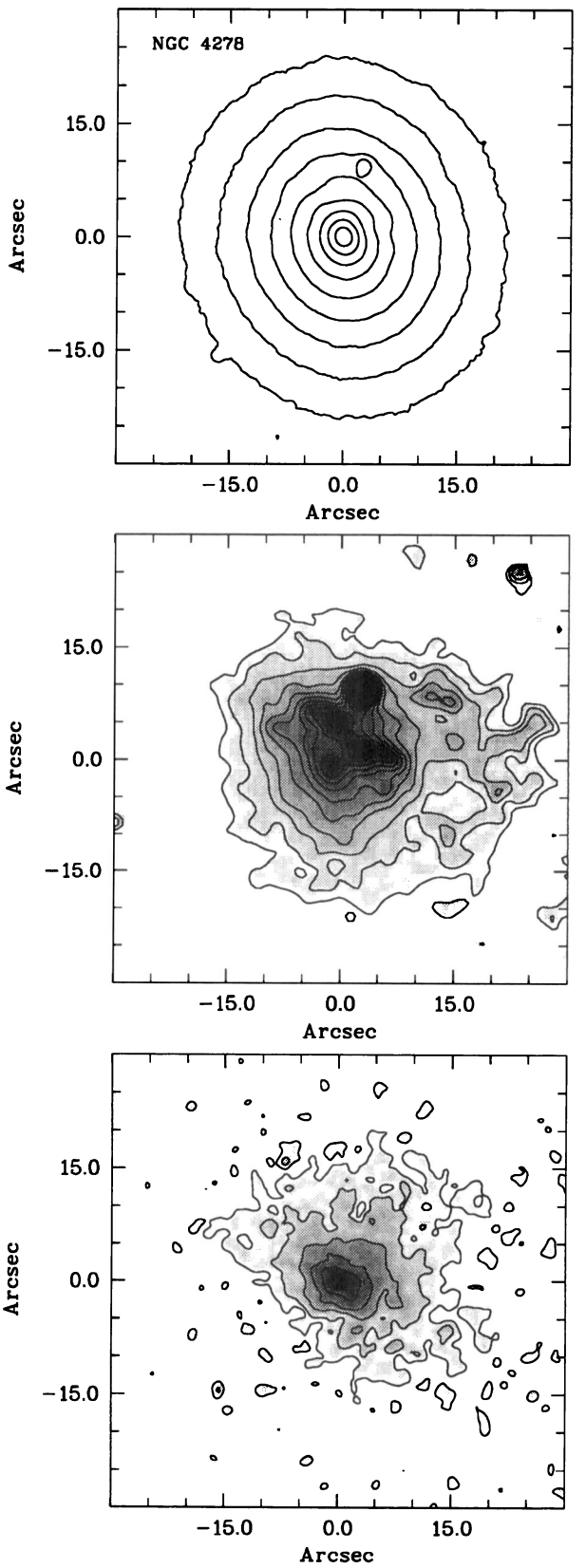

Fig. 16. NGC 4278. B (top): 21.5 (0.5) 17.5; $B-I$ (middle): 2.17 (0.02) 2.39; Hα+[NII] (bottom): 9., 18., 36., 72., 144., 288., 400

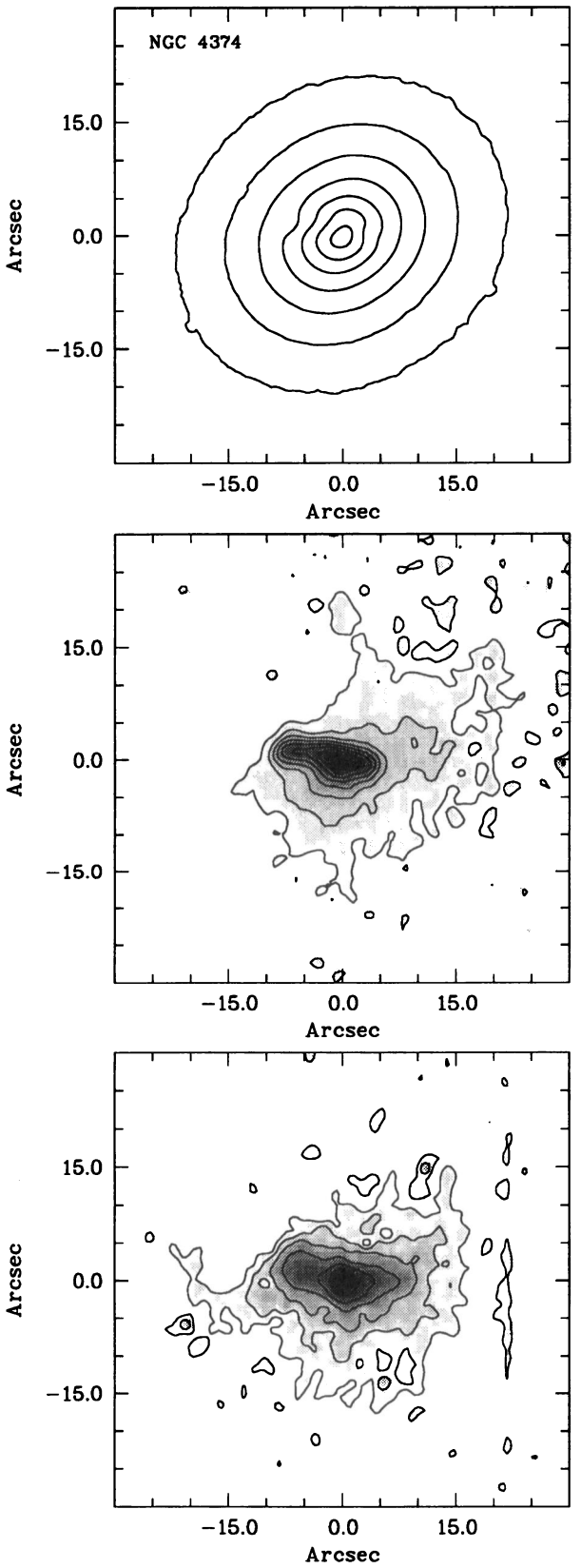

Fig. 17. NGC 4374. B (top): 20.5 (0.5) 17.5; $B-I$ (middle): 2.15 (0.03) 2.40; Hα+[NII] (bottom): .75, 1.5, 3.0, 6.0, 12.0, 24.0, 48.0

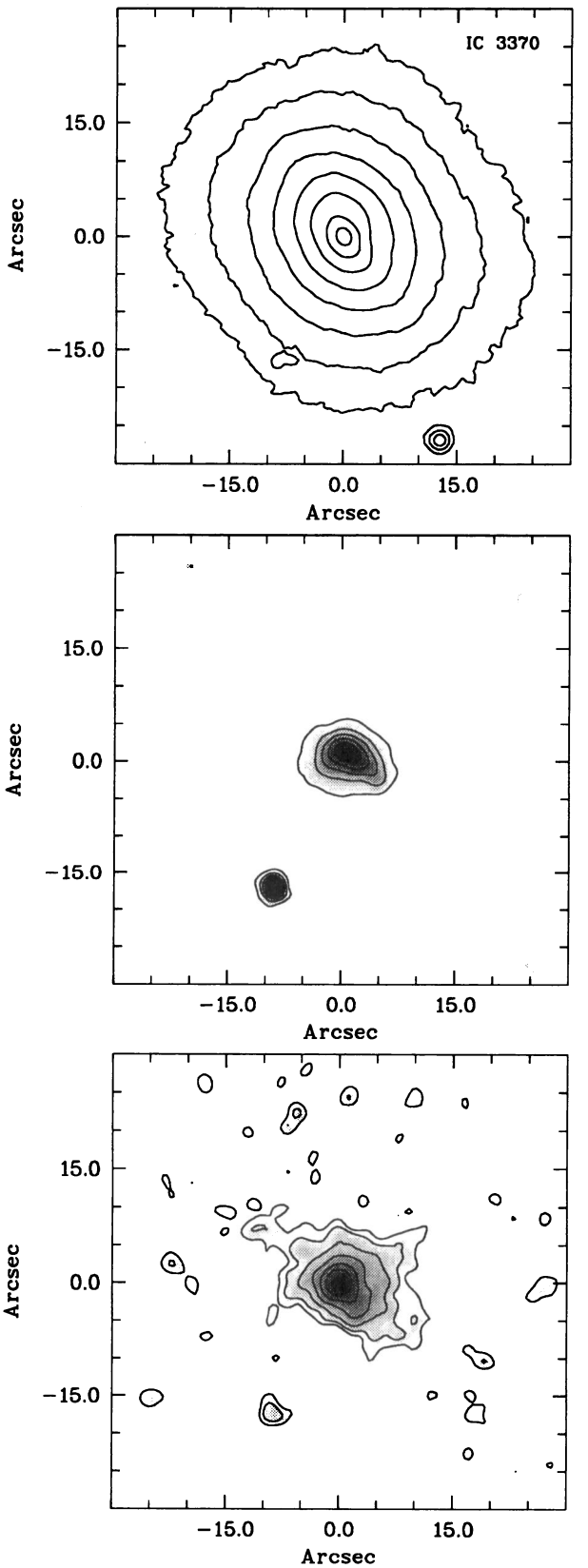

Fig. 18. IC 3370. B (top): 22.5 (0.5) 18.5; $B-I$ (middle): 2.20 (0.09) 2.65; Hα+[NII] (bottom): 1.1, 2.2, 4.4, 8.8, 17.6, 35.2, 70.4

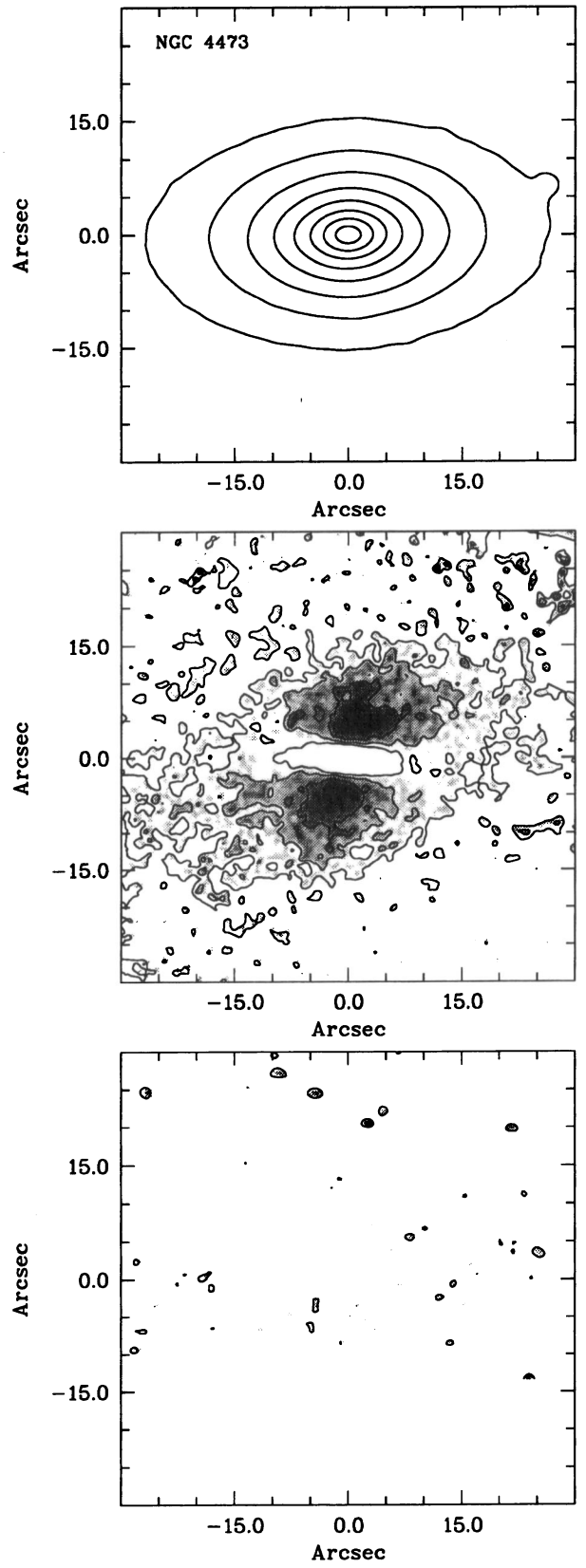

Fig. 19. NGC 4473. V (top): 20.0 (0.5) 16.0; $V-I$ (middle): 1.31 (0.02) 1.37; Hα+[NII] (bottom): 3.3, 6.6

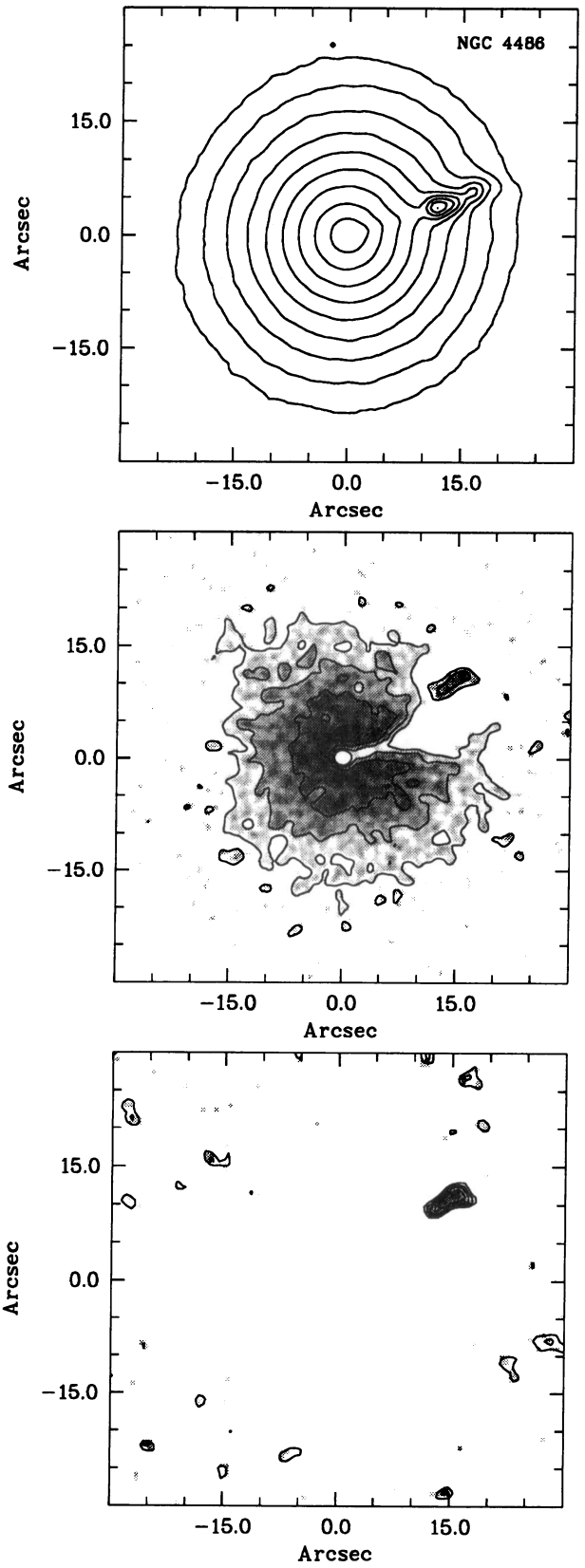

Fig. 20. NGC 4486. B (top): 20.0 (0.25) 18.0; $B-I$ (middle): 2.35 (0.02) 2.43; A_B (bottom): 0.02 (0.005) 0.045

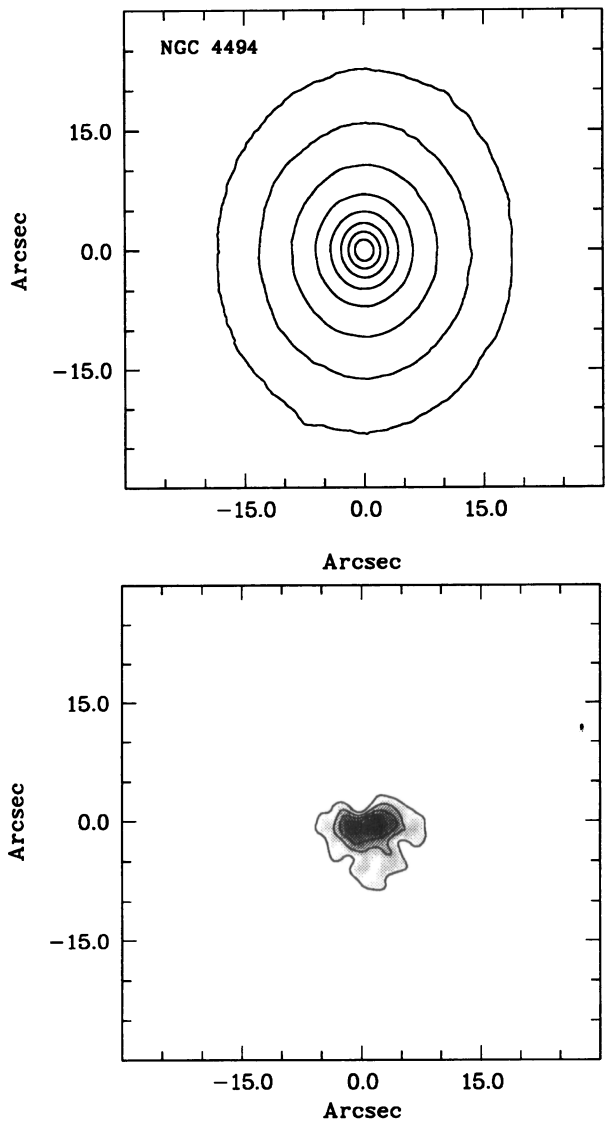

Fig. 21. NGC 4494. B (top): 21.0 (0.5) 17.5; $B-V$ (middle): 0.88 (0.04) 0.96; no Hα+[NII] available

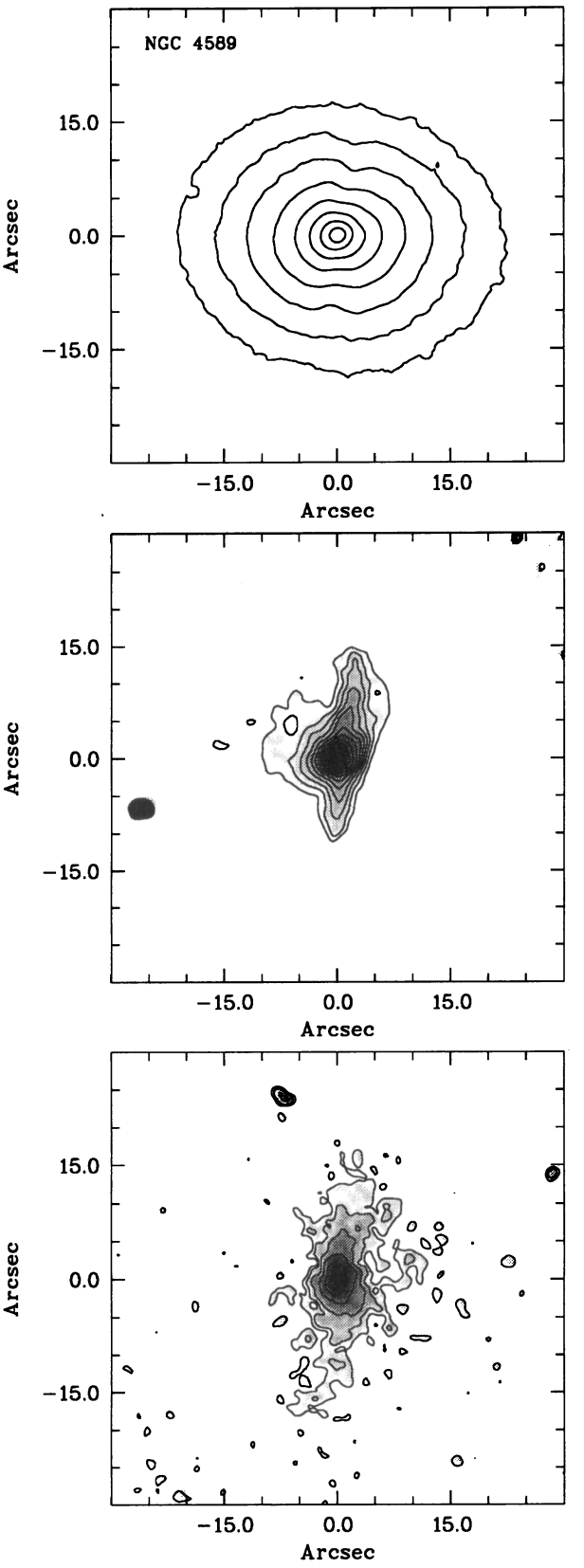

Fig. 22. NGC 4589. B (top): 22.0 (0.5) 18.5; $B-I$ (middle): 2.19 (0.03) 2.52; Hα+[NII] (bottom): 3., 6., 12., 24., 48., 72

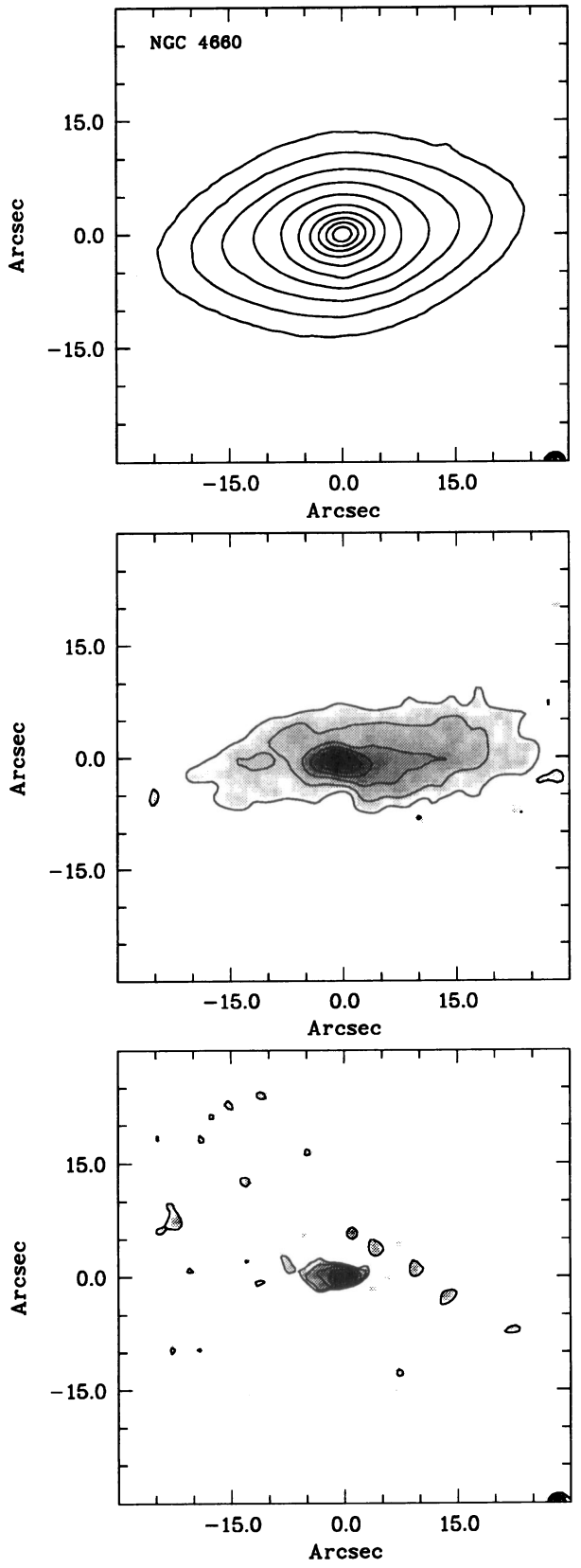

Fig. 23. NGC 4660. B (top): 22.0 (0.5) 17.5; $B-I$ (middle): 2.24 (0.03) 2.42; Hα+[NII] (bottom): 2., 4., 8., 16

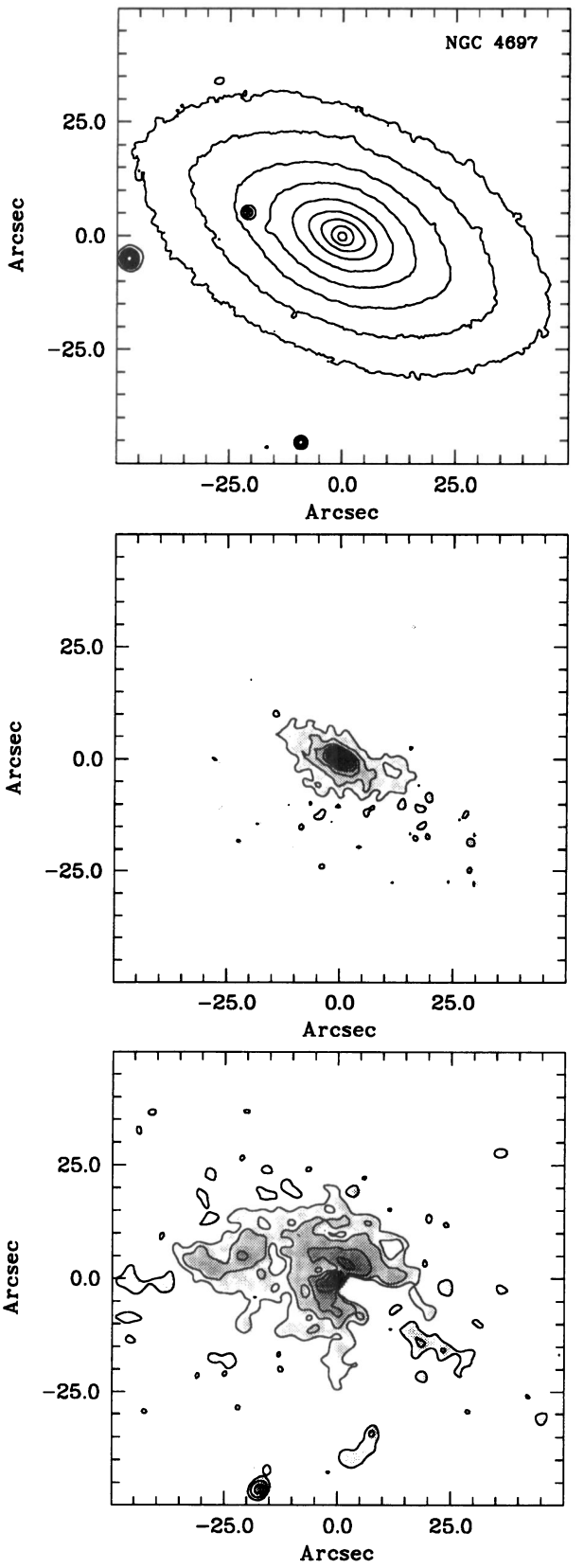

Fig. 24. NGC 4697. B (top): 21.5 (0.5) 17.5; $B-I$ (middle): 2.13 (0.03) 2.38; Hα+[NII] (bottom): .35, 0.7, 1.4, 2.8, 5.6, 11.2

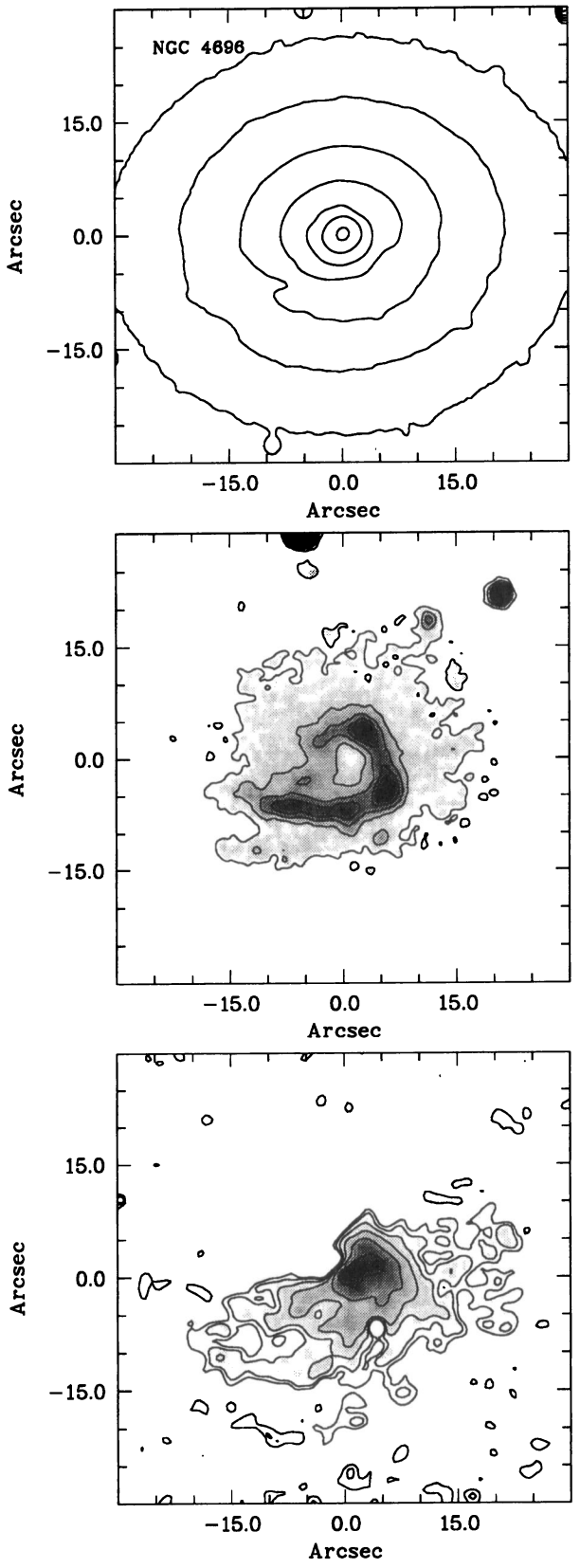

Fig. 25. NGC 4696. B (top): 22.5 (0.5) 19.5; $B-I$ (middle): 2.34 (0.04) 2.54; Hα+[NII] (bottom): .45, 0.9, 1.8, 3.6, 7.2, 14.4

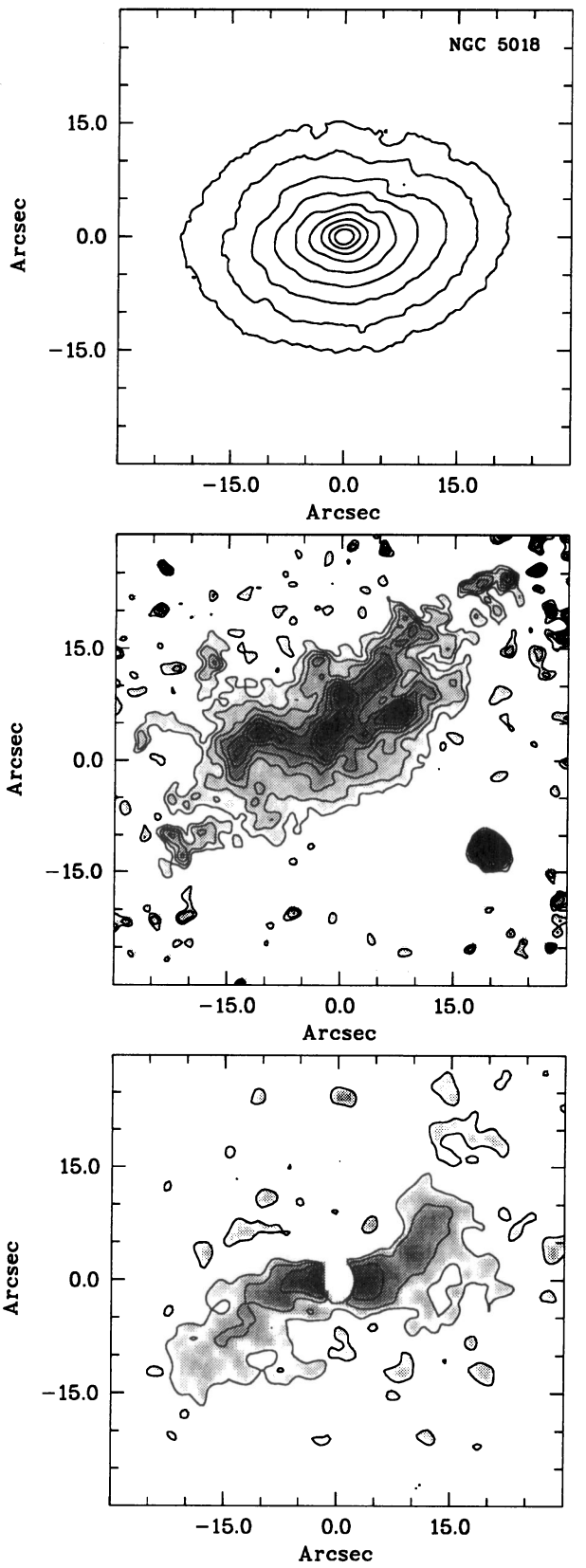

Fig. 26. NGC 5018. B (top): 21.5 (0.5) 17.5; $V-I$ (middle): 1.10 (0.02) 1.24; Hα+[NII] (bottom): 1.2, 2.4, 4.8, 9.6

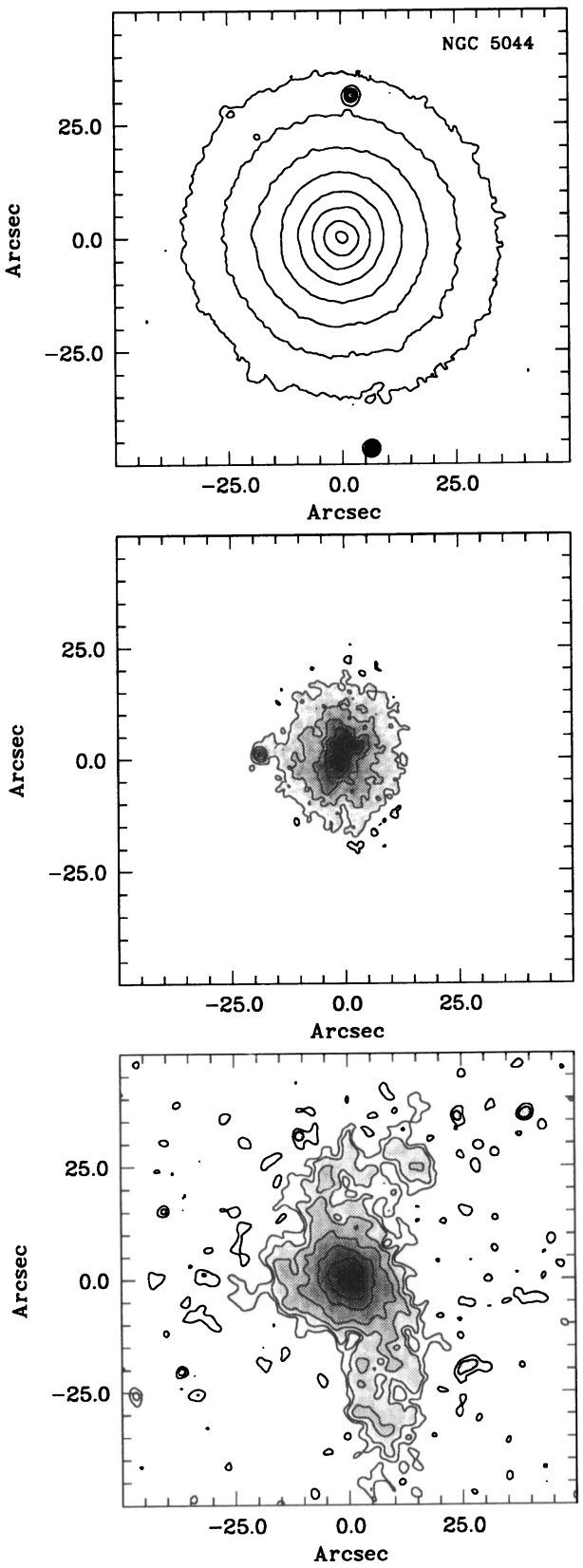

Fig. 27. NGC 5044. B (top): 23.0 (0.5) 19.5; $B-I$ (middle): 2.37 (0.04) 2.57; Hα+[NII] (bottom): 0.5, 1., 2., 4., 8., 16., 32

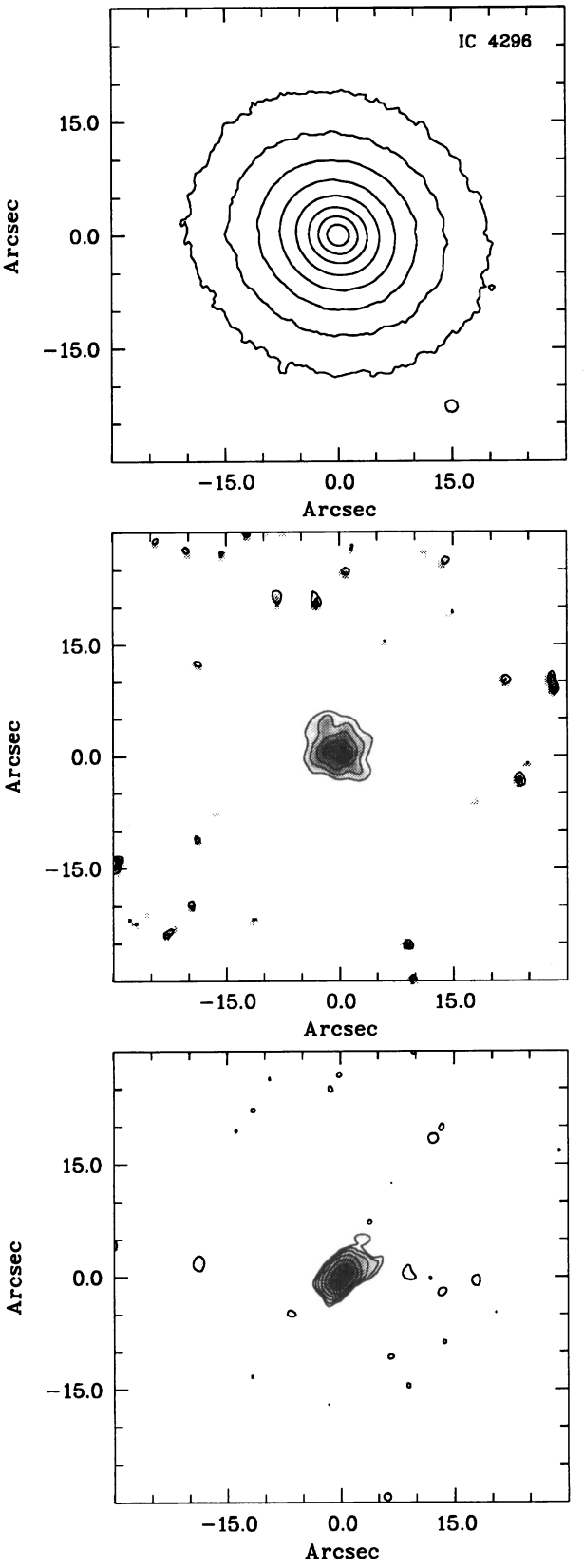

Fig. 28. IC 4296. B (top): 22.0 (0.5) 18.5; $B-V$ (middle): 1.36 (0.01) 1.40; Hα+[NII] (bottom): .75, 1.5, 3., 6., 12., 24., 48

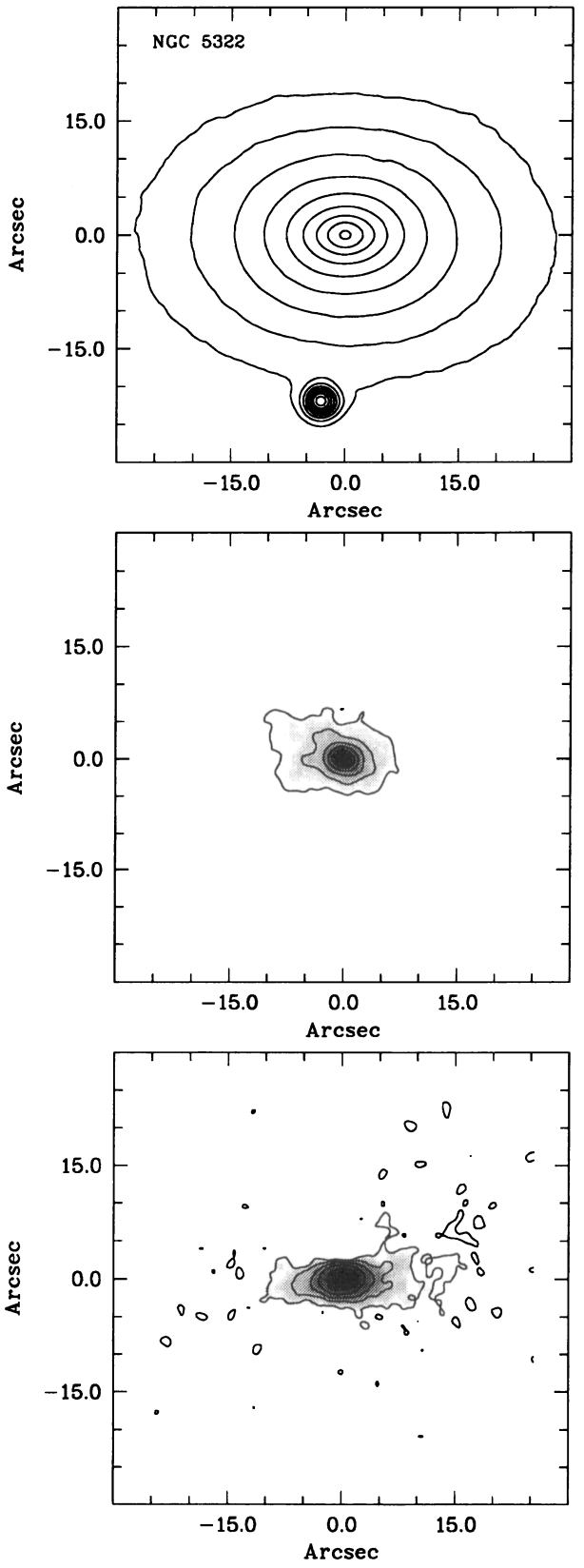

Fig. 29. NGC 5322. B (top): 21.5 (0.5) 17.5; $B-I$ (middle): 2.13 (0.03) 2.30; Hα+[NII] (bottom): 1.3, 2.6, 5.2, 10.4, 20.8, 41.6

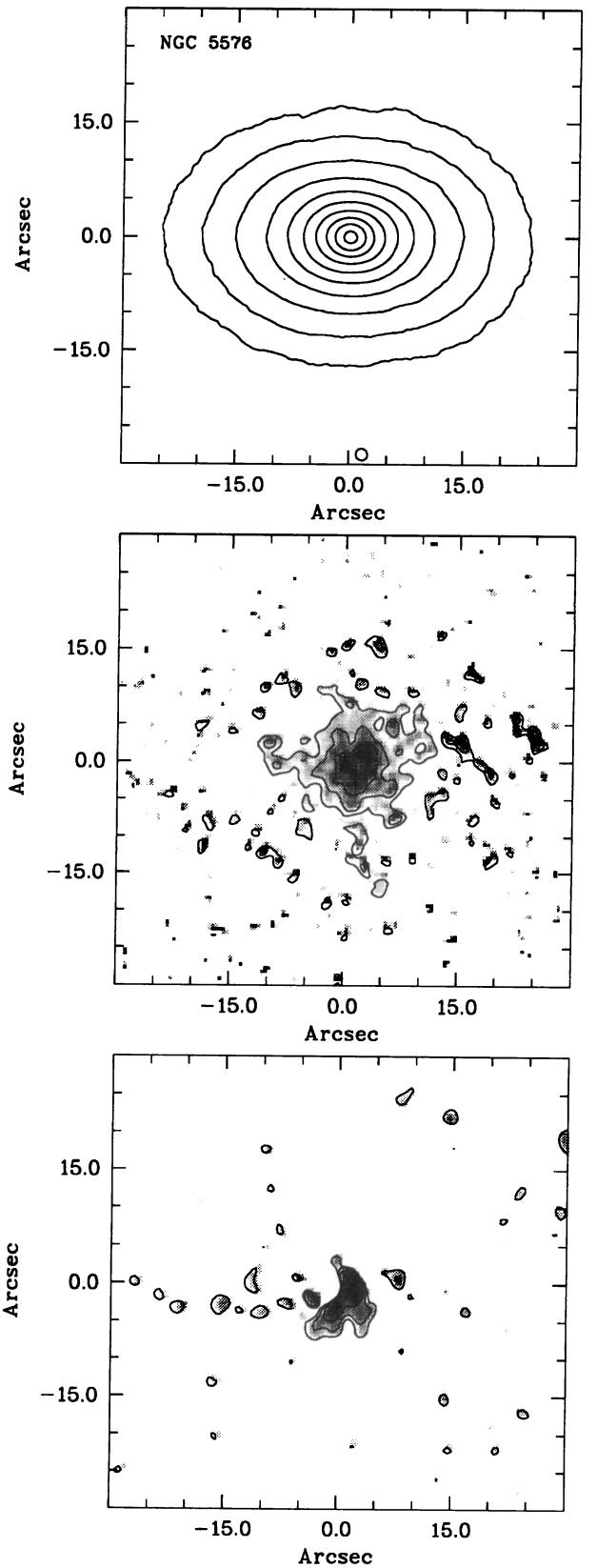

Fig. 30. NGC 5576. B (top): 22.0 (0.5) 17.5; $B-I$ (middle): 2.07 (0.02) 2.13; Hα+[NII] (bottom): 0.9, 1.8, 3.6, 7.2

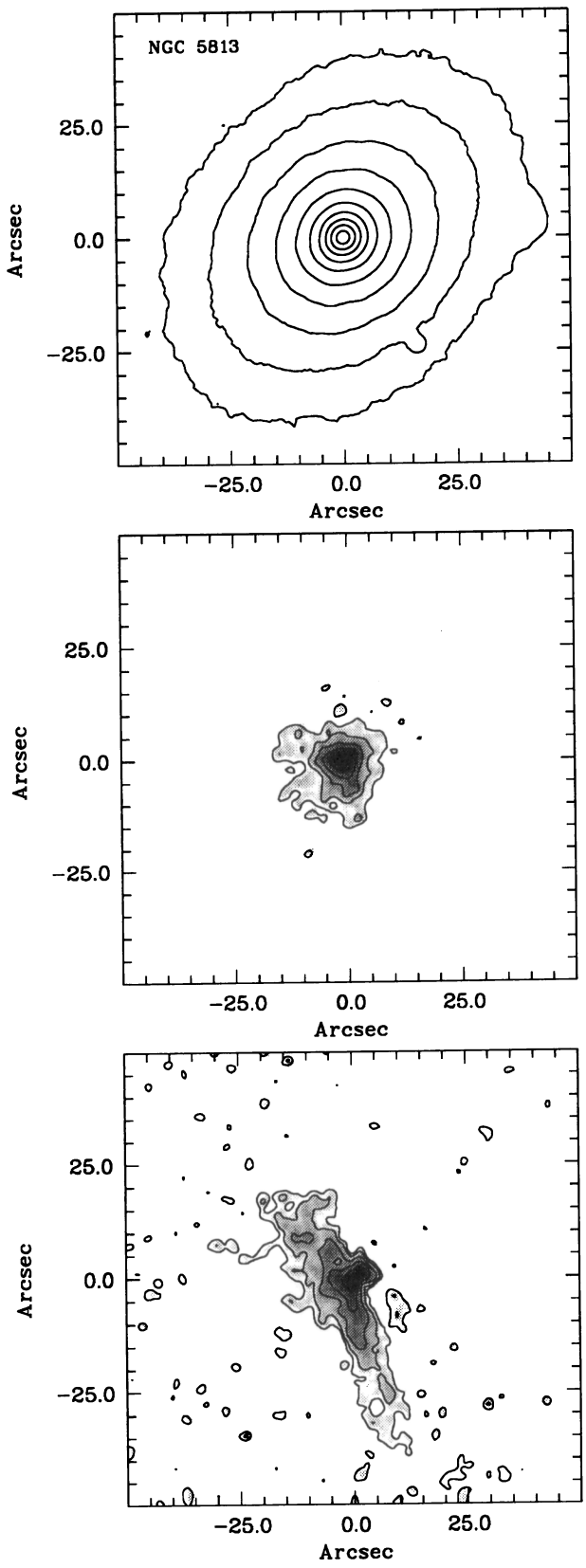

Fig. 31. NGC 5813. V (top): 22.5 (0.5) 18.0; $V-I$ (middle): 1.65 (0.02) 1.73; Hα+[NII] (bottom): 0.9, 1.8, 3.6, 7.2, 14.4

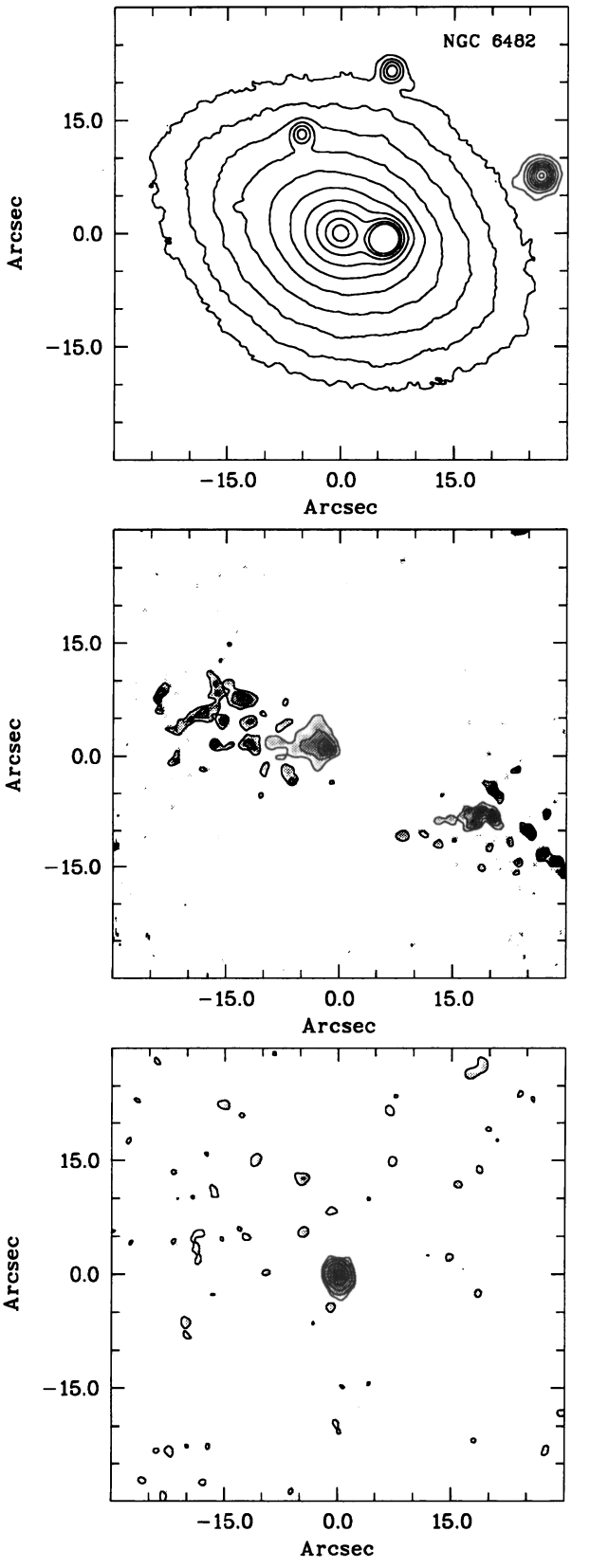

Fig. 32. NGC 6482. V (top): 22.0 (0.5) 17.5; $V-I$ (middle): 1.41 (0.02) 1.47; Hα+[NII] (bottom): 8.5, 17., 34., 68., 136

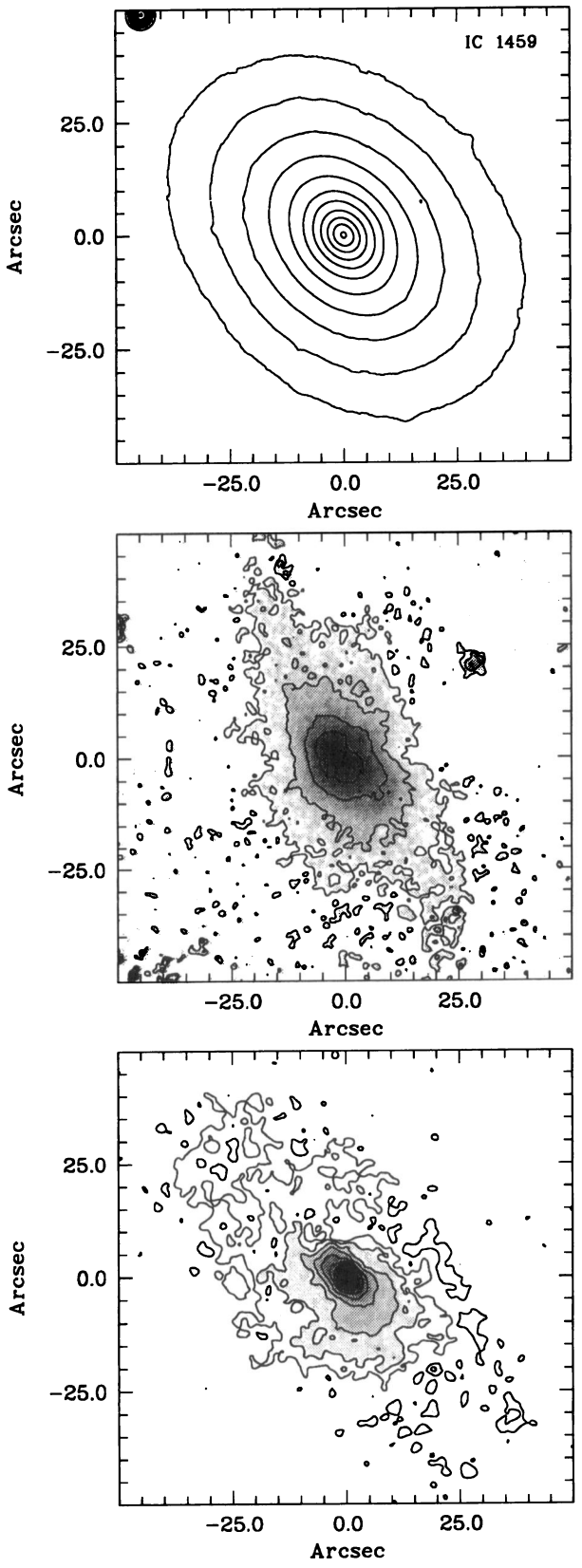

Fig. 33. IC 1459. B (top): 22.5 (0.5) 17.5; $B-V$ (middle): 1.27 (0.02) 1.35; Hα+[NII] (bottom): 0.5, 1., 2., 4., 8., 16., 32., 64., 128

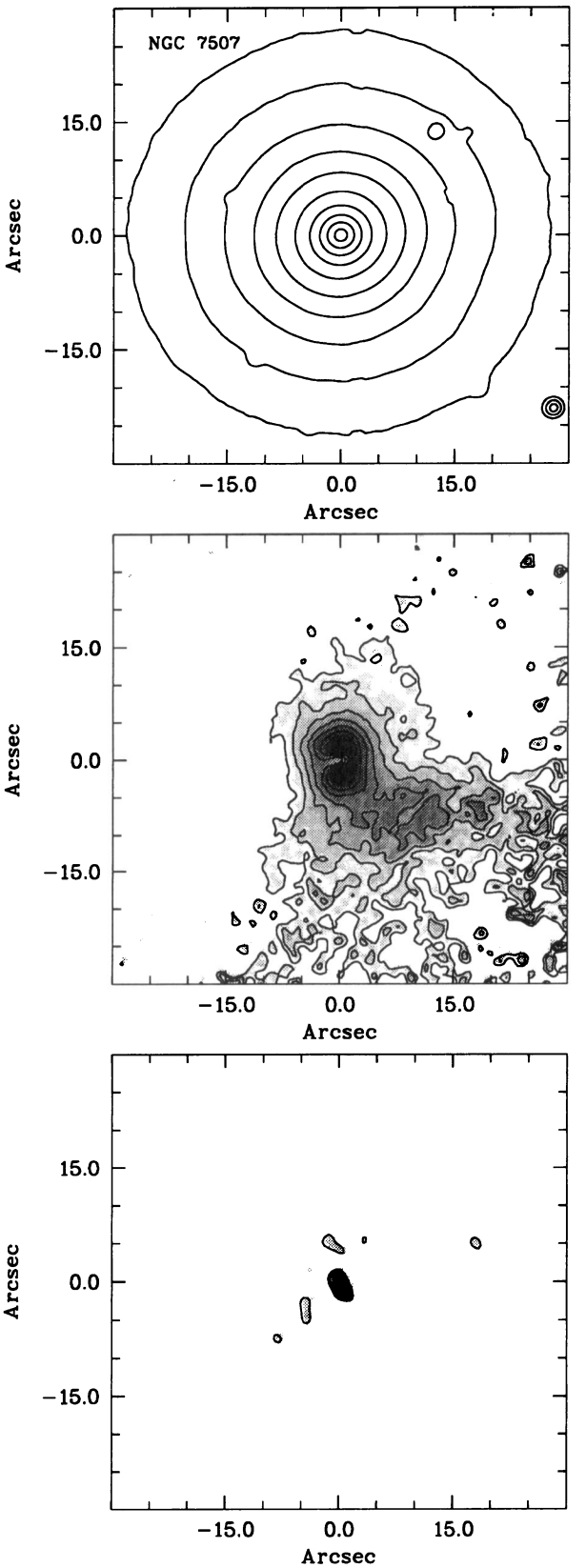

Fig. 34. NGC 7507. B (top): 22.0 (0.5) 17.5; $B-I$ (middle): 2.52 (0.02) 2.66; Hα+[NII] (bottom): 0.8, 1.6, 3.2, 6.4

B. Pure emission-line spectra of elliptical galaxies containing ionized gas

In this Appendix the pure nuclear emission-line spectra of line-emitting sample galaxies are shown, along with an illustration of the template subtraction procedure. In all following spectral plots, the upper spectrum is the observed one (corrected for reddening), the middle spectrum is the scaled template spectrum, and the lower spectrum is the pure emission spectrum, i.e., (observed−template). The emission lines Hα, [NII] $\lambda\lambda$6548, 6583, and [SII] $\lambda\lambda$6716, 6731 are shown. The ordinate units are 10^{-16} erg s^{-1} cm^{-2} Å^{-1} for the observed spectra; a suitable constant was added to the template- and pure emission spectra for ease of visualization. The elliptical galaxy corresponding with each spectrum is indicated in the upper left corner of the plot.

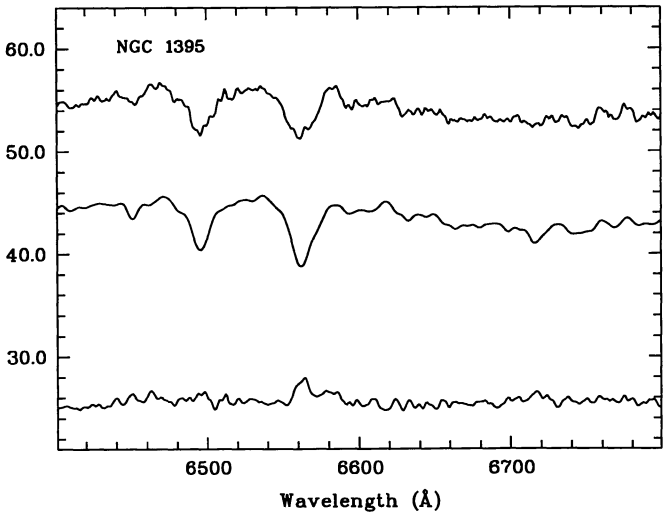

Fig. B.1.

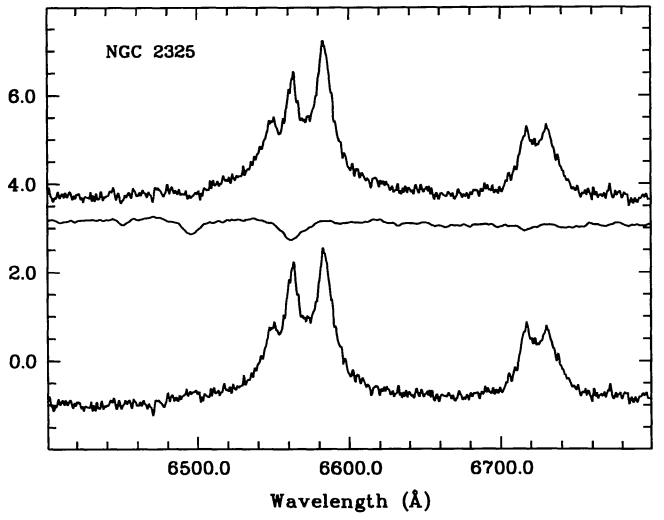

Fig. B.2.

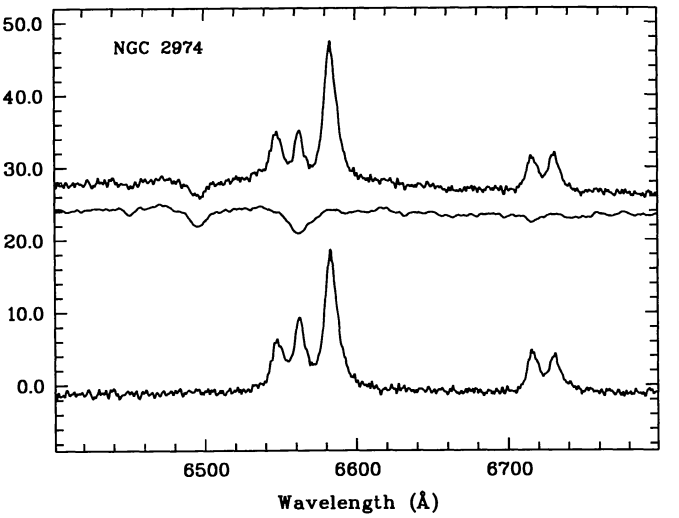

Fig. B.3.

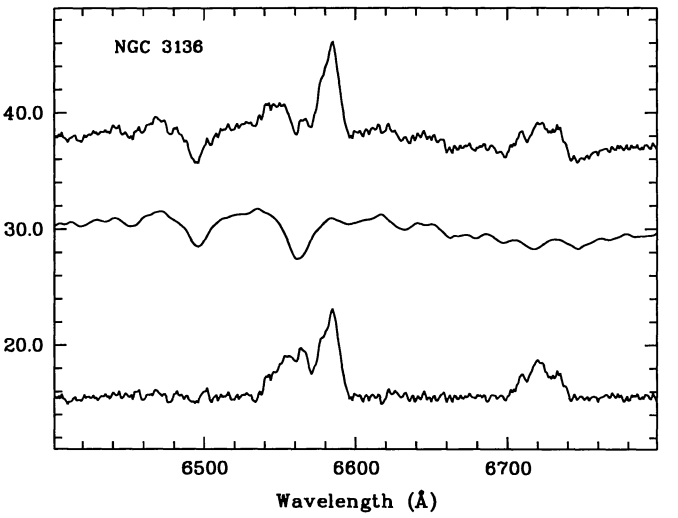

Fig. B.4.

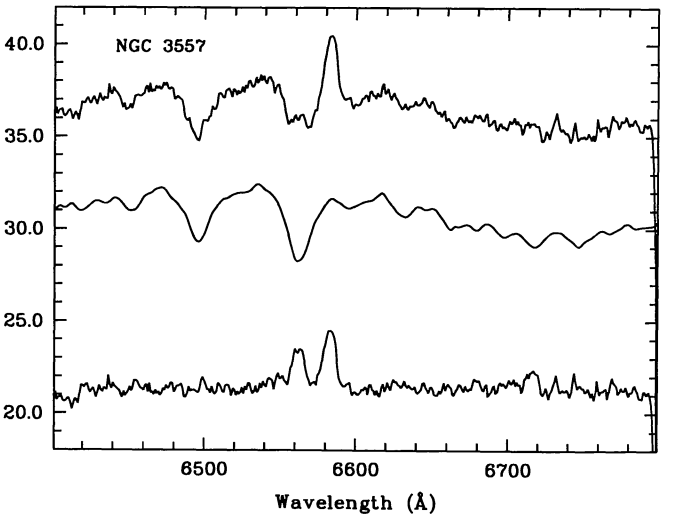

Fig. B.5.

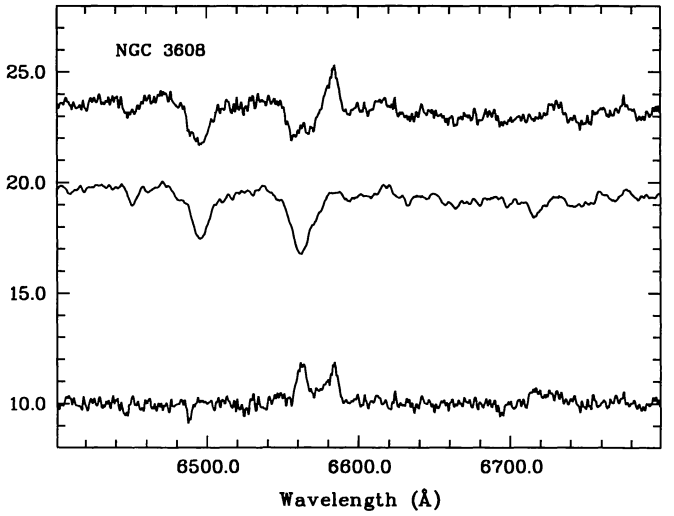

Fig. B.6.

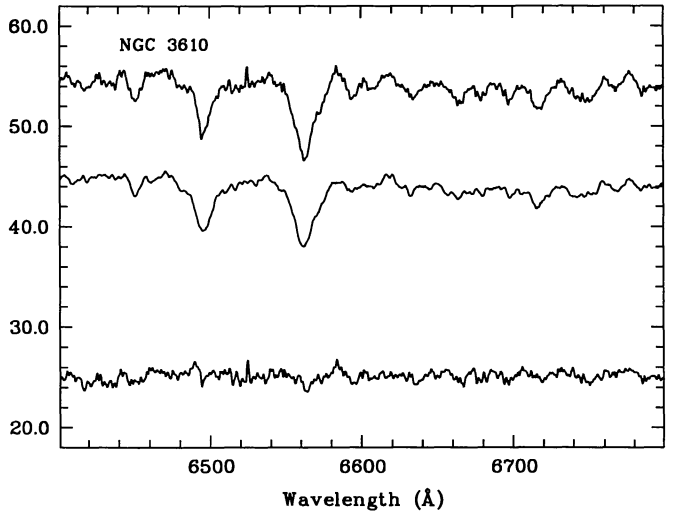

Fig. B.7.

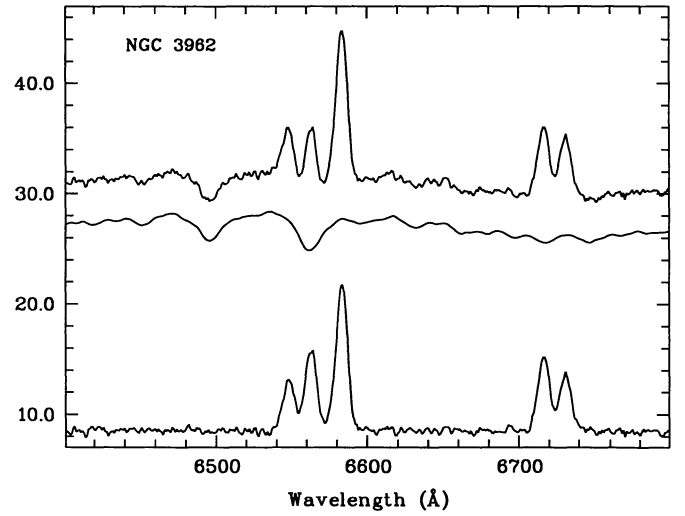

Fig. B.8.

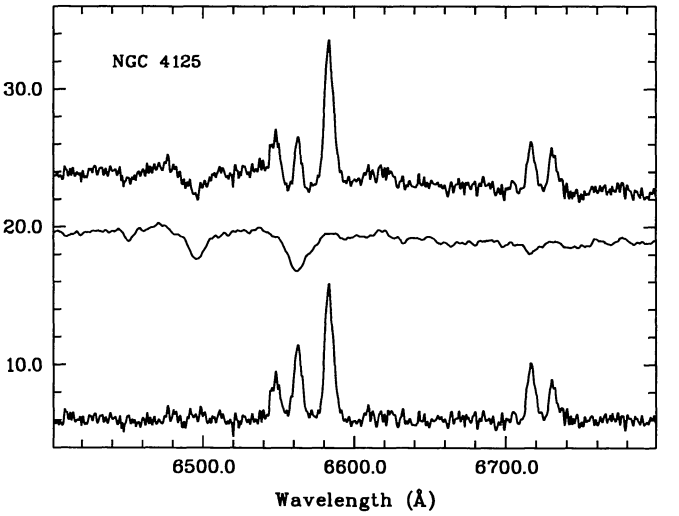

Fig. B.9.

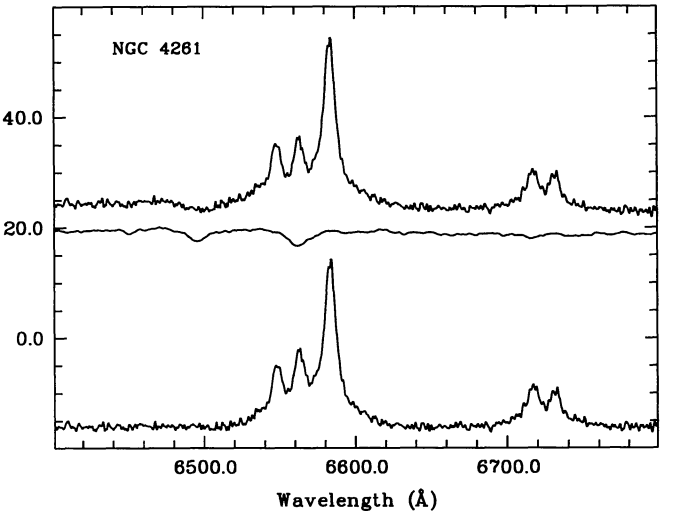

Fig. B.10.

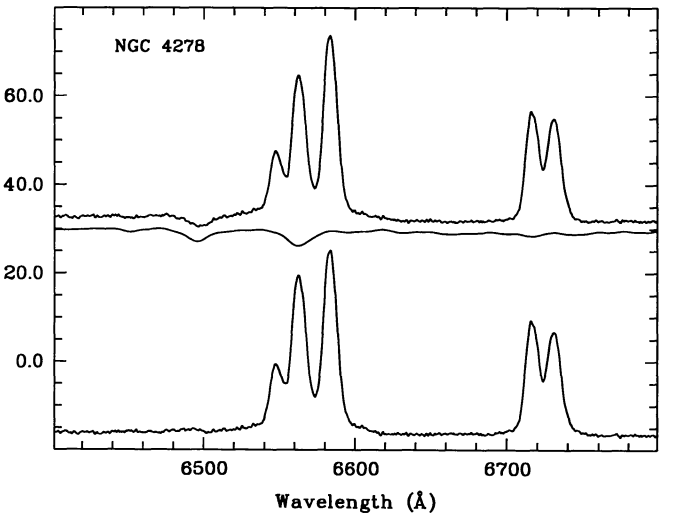

Fig. B.11.

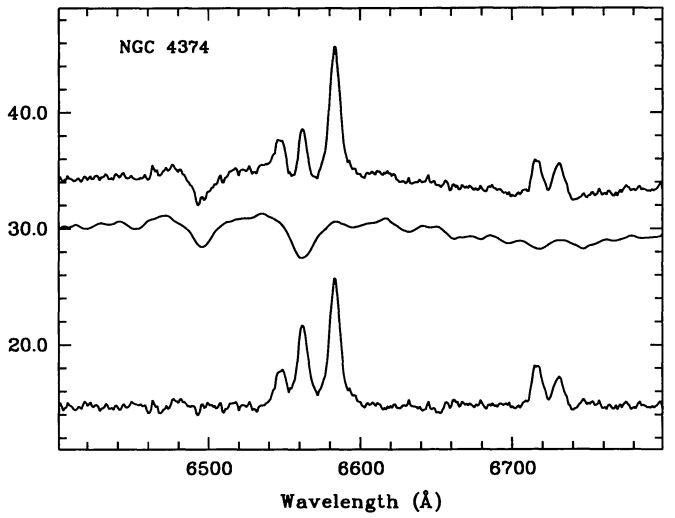

Fig. B.12.

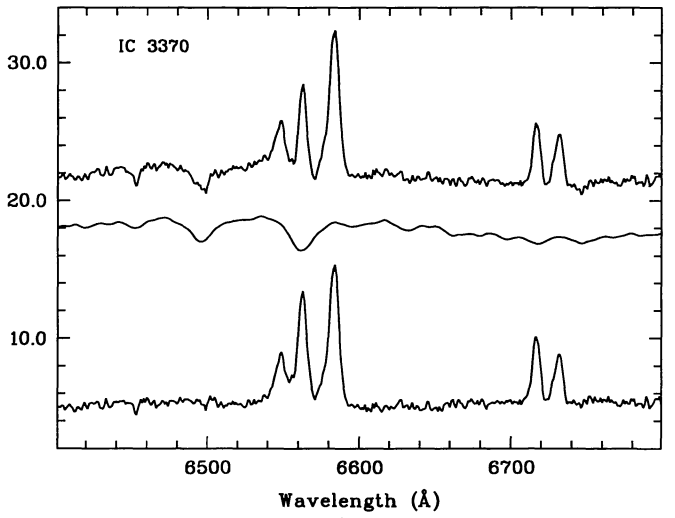

Fig. B.13.

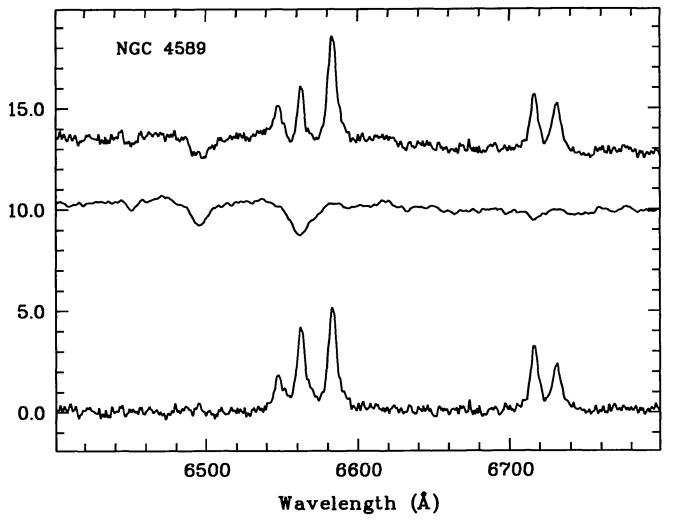

Fig. B.14.

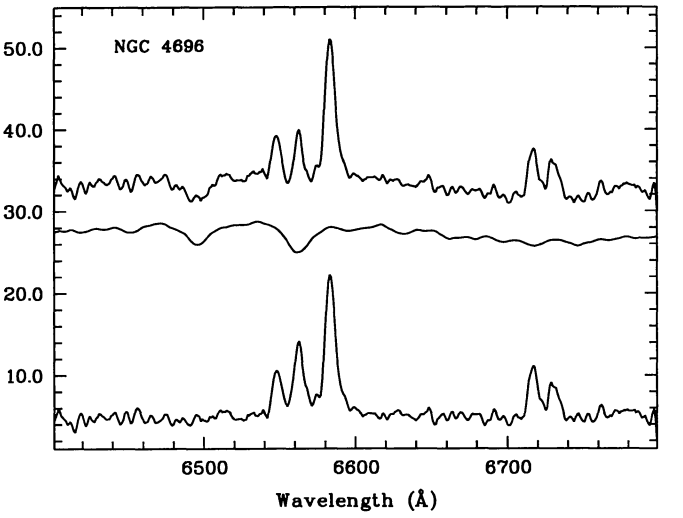

Fig. B.15.

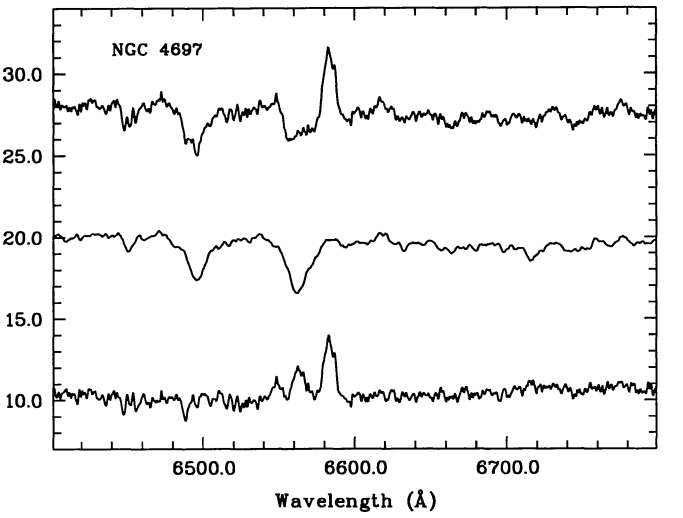

Fig. B.16.

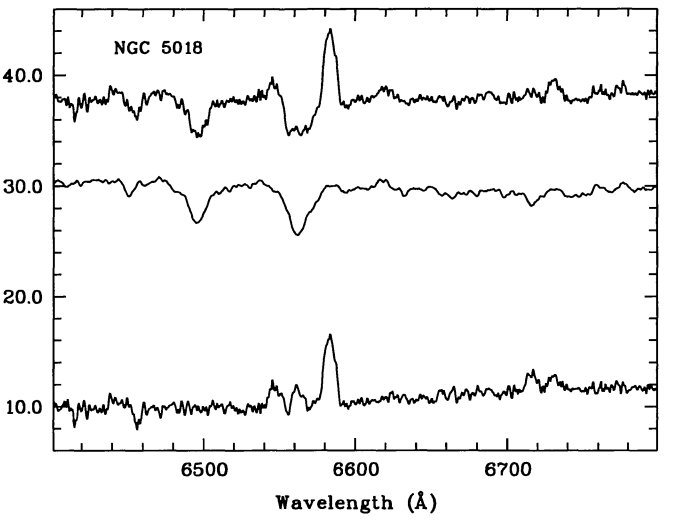

Fig. B.17.

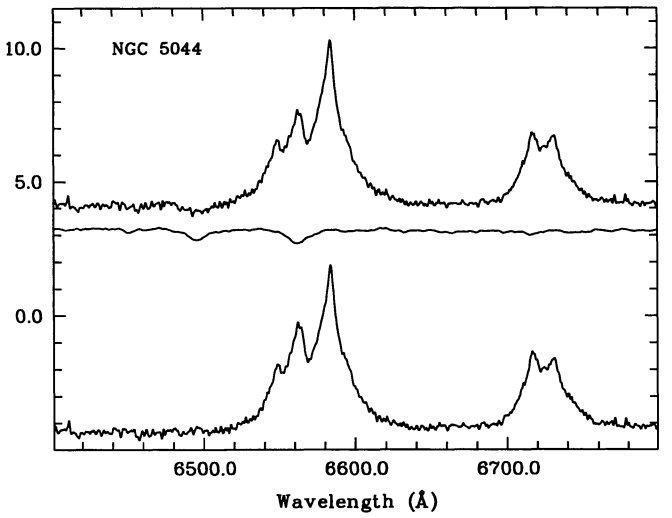

Fig. B.18.

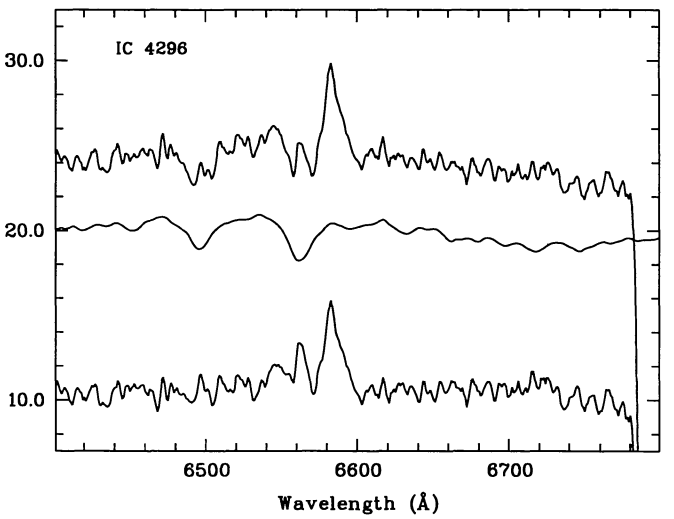

Fig. B.19.

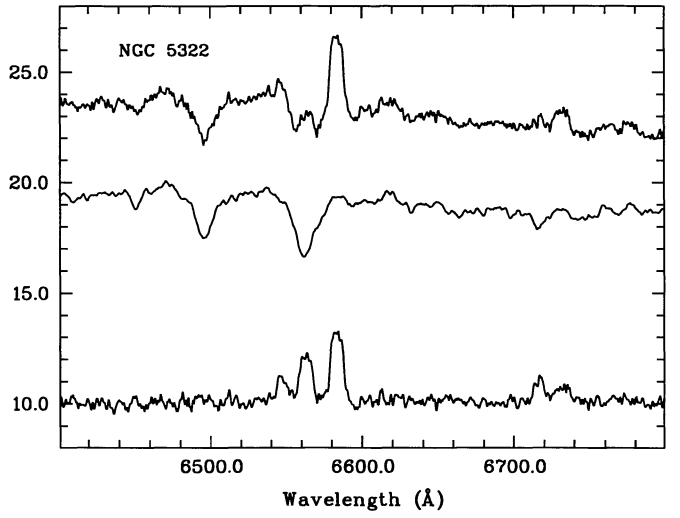

Fig. B.20.

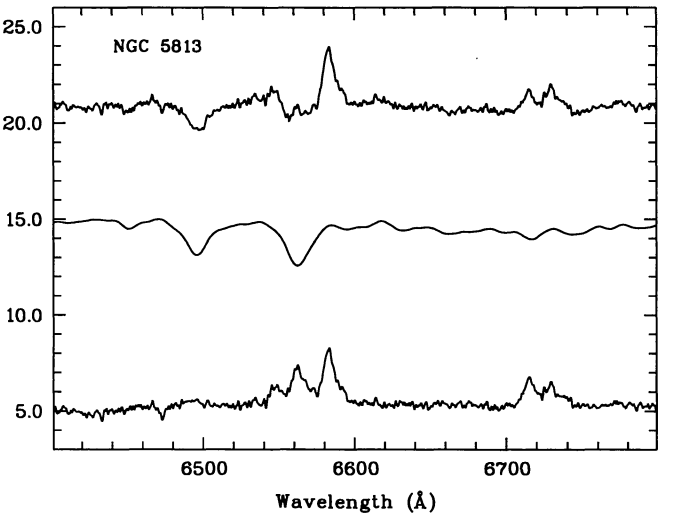

Fig. B.21.

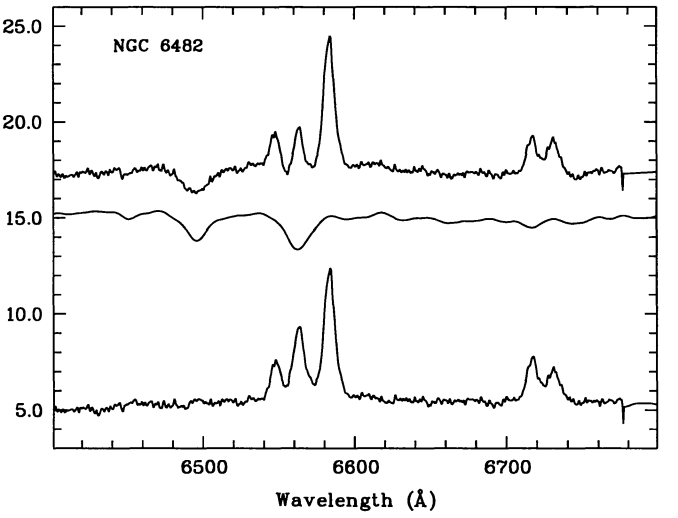

Fig. B.22.

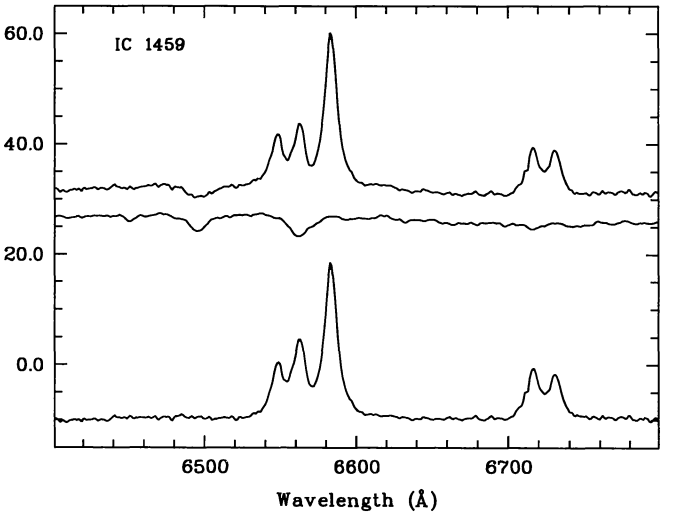

Fig. B.23.